Doctoral School of Geosciences

Characterizing Small-Scale Heterogeneity in Quaternary Freshwater Carbonates of Hungary Using CT Scan Data

Ph.D. Thesis

Author

Nour Nayef Hassan Alzoubi

Supervisor

Sándor Gulyás, Ph.D.

Assistant professor, Vice head of the department

Scientific consultant

János Geiger, Ph.D.

Associate professor

Department of Geology and Palaeontology

University of Szeged

Faculty of Science and Informatics

2023

Szeged

Table of Contents

Table of Figures

List of Tables

List of abbreviations and Acronyms

3D ---------- Three dimensons

a.s.l ---------- Above Sea Level

AIC ----------Akaiki Information Criterion

BVS ---------- Below Voxel Size

DICOM ---------- Digital and Imaging Communications in Medicine

DTI ---------- Danube Tisza Interfluve

EM ---------- Expectation maximum likelihood

FOV---------- Filed of View

GHP ---------- Great Hungarian Plain

HU ---------- Hounsfield Unit

K ----------Kurtosis

kVp ---------- peak KiloVoltage

mAs ---------- milliAmpere Second

MD ---------- Median

mm ---------- millimetre

PWPs ---------- Potential Water Paths

RFCs ---------- Rock-Forming Components

SK ----------Skewness

TDS ---------- Total Dissolved Solid

X-Ray CT ---------- X-Ray Computer Tomograph

XRD ---------- X-ray diffraction analysis

I. INTRODUCTION

I.1. General background:

The Danube-Tisza Interfluve (DTI) is the area between the Danube River and the Tisza River over the Southern Great Hungarian Plain (GHP) which is composed of wind-blown sand and loess deposits that contain up to 10% carbonate minerals, mainly dolomite (Molnár *et al.,* 1995). During the end of the Pleistocene and the beginning of the Holocene period, hypersaline lakes formed through interdunes due to high groundwater levels or surface runoff (Jenei *et al.,* 2007; Lóczy, 2015).

Two types of carbonate strata are presented in the area, with loose carbonate mud restricted to the north-western part, while solid carbonate rock (dolomitic limestone) overlain by unlithified carbonate mud is present in the southeast. The type of carbonate mineral formed is controlled by temperature, evaporation rate, pH, CO2 absorption by aquatic plants, and ions concentration, with the Mg/Ca ratio playing a crucial role (Molnár *et al.,* 1980).

The lakes dry up during summers, and secondary carbonates occur when the salinity fluctuates greatly during the year. Rainfall during autumn supplies freshwater to the DTI alkaline lakes, decreasing Na and K concentrations and increasing the Mg/Ca ratio from 7–12, creating favourable conditions for the precipitation of high-magnesium calcite. The high-magnesium calcite precipitates seasonally based on climatic conditions and groundwater table fluctuations (Müller *et al.,* 1972). Proto-dolomite forms in mud deposited over a lakebed via a transformation of Mg-bearing calcite during periods when pore waters are rich in Mg. (Molnár *et al.,* 1980). Sedimentary rocks provide valuable records of past environmental and climatic changes. By analysing the composition and proportion of rock-forming components (RFCs), we can reconstruct these changes at high resolution.

Computer tomography techniques have found applications beyond medical imaging. Researchers have utilized these techniques in various non-medical fields, such as specialized cross-sectional imaging for non-destructive testing, determining celestial sphere brightness distribution, and three-dimensional imaging with electron microscopy. Tomographic imaging involves recreating a picture from its projections, where a projection represents the integral of the picture in a specific direction. Projections can be derived from transmitted energies or

diffracted sources like ultrasound and microwaves. The advancements in reconstruction algorithms played a crucial role in the rapid improvement of X-ray computed tomography, making it capable of producing high-quality and anatomically accurate images (Kak & Slaney, 1999). X-ray computed tomography (CT) can be used in sedimentology and geology to produce cross-sectional tomographic images of sedimentary rocks and assess the nature of their formation and diagenetic history. Furthermore, CT is used in materials science and engineering to investigate the internal structure and properties of materials, as well as in archaeology, art conservation, and palaeontology.

I.2. Research Objectives and Hypothesis

The main objective of this study is to quantitatively distinguish the rock-forming components of freshwater carbonates based on their density differences and make inferences about heterogeneity. Therefore, the minor goals were researched as follows.

1. Understanding the small-scale heterogeneity in Quaternary freshwater carbonates found in Central Hungary.
2. Defining the rock-forming components (RFCs) by applying univariate statistical and EM mixture analysis on the Holocene freshwater carbonate rocks.
3. Discussing how X-ray CT scans can be used to draw paleoenvironmental and paleoclimatic inferences from alkaline lake deposits in Hungary.
4. Exploring how CT data analysis can help reveal structural heterogeneity and potential flow paths in freshwater carbonates used as decorative and building stones.

I.3. Sampling, methods, and workflow

Three major choices were followed in picking samples in this research: RFCs, mixture analysis algorithm, and watershed algorithm.

I.3.1. Sampling

The samples used in this study are the same ones collected and analysed by Mucsi (1963) from a now protected outcrop near Csólyospálos. The outcrop is approximately one meter deep. The four carbonate samples are currently housed in the sedimentary rock collection of the

Department of Geology and Palaeontology at the University of Szeged. Each sample was initially cut in half and had their surfaces polished.

Four samples, namely Cs-1, Cs-2, Cs-3, and Cs-4, were selected to represent all members of the Csólyospálos carbonate sequence. Cs-1 and Cs-2 are represented by a single sample (referred to as sample I) taken from a depth ranging between 65 to 90 cm in the section. Cs-3 is represented by two adjacent samples (referred to as samples II and III) obtained from a depth of 65-60 cm. Lastly, Cs-4 is represented by a single sample (referred to as sample IV) collected from a depth of 55-25 cm (Molnar *et al.,* 1976).

I.3.2. CT scan parameters

At the University of Pécs in Hungary, the Institute of Diagnostic Imaging and Radiation Oncology conducted high-resolution X-ray CT scans. The scanning process utilized an instrument operating at a peak kilovoltage (kVp) of 140, with a current of 189 milliampere seconds (mAs) and a sampling interval of 1.5 seconds. The lateral resolution of the scan was 0.234 mm x 0.234 mm, and each scan slice had a thickness of 1.5 mm. The image reconstruction matrix comprised 512 x 512 pixels. CT images were saved in a DICOM (Digital and Imaging Communications in Medicine) format.

The metadata of a DICOM file includes important scanning parameters such as Pixel Spacing and Slice Thickness attributes. These metadata hold crucial information for geoscientific applications as they document the dimensions (in millimetres) of each voxel in the x, y, and z directions. DICOM is a widely used image format in medical applications and can be easily interpreted by conventional 3D volume rendering software like VOXLER.

In this study, CT data analysis is shown to provide a more objective and comprehensive understanding of the heterogeneity and textural properties of freshwater carbonates of the GHP compared to traditional thin-section analysis. The thin-section analysis is limited to selected areas of the sample, making estimations subjective. CT data analysis provides quantitative 3D data at different scales, allowing for more accurate characterization of the rock-forming components (RFCs) and their textural heterogeneity. The density information obtained from CT data correlates with the composition of RFCs. Mixture analysis is used to segment RFCs based on CT data, considering the complexity and overlap of distribution curves. The study suggests reevaluating the nomenclature of rocks based on the more accurate estimations provided by CT.

I.3.3. Rock-Forming Components and Mixture analysis algorithms

The identification of the rock-forming components (RFCs) was accomplished through mixture analysis. In this approach, a non-hierarchical clustering technique based on maximum likelihood was employed to estimate the parameters (Mean and Standard Deviation) of multiple univariate normal distributions. These distributions represent groups that overlap and correspond to the RFCs. The algorithm used for this purpose was the EM algorithm introduced by Dempster et al. in 1977. Since our research primarily focuses on the spatial distribution, orientation, and connectivity of voids in brick samples, it was sufficient to determine the void spaces and the main minerals of the rock-forming components. A histogram provides a graphical representation of the distribution of pixel intensity values in an image, where the x-axis denotes the intensity values, and the y-axis denotes the frequency of occurrence.

I.3.4. Watershed algorithms

The term "watershed transformation" refers to a geographical boundary or dividing line between adjacent drainage basins. In simple terms, when a drop of water falls on a terrain, it naturally flows towards the nearest lowest point. This lowest point is identified as the endpoint of the steepest descent path. In the context of topography, this occurs if the point lies within the catchment basin of that lowest point (Beucher & Meyer, 1993).

A watershed map takes data from a grid file and divides the grid into separate basins or catchment areas. The number of basins depends on the sizes of the individual areas and is determined by the number of upstream cells that flow into the grid cells. Increasing the threshold value reduces the number of identified basins. The calculation of flow lines or flow paths is based on the amount of flow into a grid node from surrounding nodes. These lines connect the lowest points on the map. Various algorithms exist for watershed transformation, such as the ones proposed by Beucher & Meyer (1993) and Wang & Liu (2006). In our research, we applied a specific topological algorithm called the accurate eight-direction four-point algorithm, which utilized the Laplace operator. This algorithm was used to identify potential areas of dissipation and confluence. By assigning potential non-real flow paths (PWP) to the grid at each grid node of the CT slices obtained from the SURFER system, we were able to calculate the flow direction at each grid node. (Quick start guide - Surfer Software 2023).

II. Defining Rock-Forming Components of Holocene Freshwater Carbonates Via Univariate Statistical and Mixture Analysis of Computer Tomography Data

Nour Alzoubi*, Janos Geiger, Sandor Gulyas

University of Szeged, Department of Geology, 2-6 Egyetem u., H-6722,

Szeged, Hungary.

e-mails:
Nour Alzoubi*
nouralzoubi@geo.u-szeged.hu
Corresponding author
János Geiger
geostatisztika@gmail.com
Sandor Gulyas
csigonc@gmail.com

Studia Quaternaria,
vol. 39, no. 2 (2022): 113–128
DOI: 10.24425/sq.2022.140887

Defining Rock-Forming Components Of Holocene Freshwater Carbonates Via Univariate Statistical And Mixture Analysis Of Computer Tomography Data

By Nour Alzoubi, Janos Geiger, Sandor Gulyas*

Abstract:

Carbonate rocks are among the sedimentary systems which preserve information on the formation and diagenetic history expressed in its composition (distribution of its major rock-forming components (RFC). For estimating RFC proportions at the micro-scale, a simple counting of visible RFCs in thin sections using overlaid grids is a long-used, well-established technique. However, computer tomography (CT) analysis provides us with quantitative data in 3D at both the scale of the entire sample and a resolution defined by dimensions of the voxels at the micro-scale. The quantitative data expressed in Hounsfield units (HU) correlates with the density of RFCs. In this work statistical properties of CT-based data for selected freshwater carbonate samples from the Danube-Tisza Interfluve have been assessed using histograms and boxplots. Univariate statistical parameters characterize each sample. The maximum-likelihood method of mixture analysis has been adapted to recover and estimate the parameters of these subpopulations. Subpopulations have been defined in the form of overlapping intervals using statistical parameters gained (mean±2STD). Five major components have been defined: empty and partially or entirely filled pores by calcite, limestone micrite, dolomite micrite matrix and limonite saturated matrix.

II.1. INTRODUCTION

The Danube-Tisza Interfluve (DTI) found in the central part of Hungary is covered by wind-blown sand and loess deposits bearing dolomite and other carbonate minerals and having a carbonate content of up to 10%. Prevailing winds during the Late Pleistocene and the Holocene arranged these sands into a series of dunes of NW-SE direction (Mihältz, 1947, 1953; Molnár, 1961, 1970, 1988, 2000). Interdune depressions harbored some 150–200 alkaline freshwater lakes preceding river regulations of the 19th century (Fig. II-1B). These lakes obtain their water from groundwater, rich in dissolved Ca and Mg, and surface runoff from the nearby areas (Molnár and Szónoky, 1976; Molnár and Murvai, 1976; Molnár *et al.,* 1995). Extensive freshwater carbonate strata composed of dolomitic limestone and dolomite developed during the Holocene (Mihältz and Faragó, 1946; Mihältz, 1947, 1953; Mucsi, 1963; Molnár, 1961, 1970, 1980, 1983, 1985; Jenei *et al.,* 2007; Sümegi *et al.,* 2015; Sümegi & Náfrádi, 2015). In general, two basic types of carbonate strata are present in the area with loose carbonate muds, 30–110 cm thick, overlying loess or wind-blown sands being restricted to the north-western part. In the southeast where the lacustrine phase of carbonate formation ended, diagenesis allowed for the formation of solid carbonate rock (dolomitic limestone), overlain by unlithified

carbonate muds in its upper parts (Mihältz 1947, 1953; Mihältz and Faragó, 1946; Molnár, 1961, 1970, 1980, 1983, 1985; Jenei *et al.,* 2007; Mucsi, 1963; Sümegi *et al.,* 2015; Sümegi & Náfrádi, 2015). The precipitation of high magnesium calcite from the lake water, and the formation of dolomite and proto-dolomite attributable to seasonal variations of the climate and concomitant volume, geochemical (pH, dissolved element concentration) changes of the groundwater, pore waters and the water body in these lacustrine environments is a unique feature of the area. The formation of freshwater carbonates in the freshwater lakes of the DTI has been discussed in various studies (Mihältz 1947, 1953; Mihältz and Faragó, 1946; Molnár, 1961, 1970, 1980, 1983, 1985; Mucsi, 1963; Müller, 1970; Müller *et al.,* 1972; Jenei *et al.,* 2007; Sümegi *et al.,* 2015; Sümegi & Náfrádi, 2015) Müller et al. 1972 presented a general model of lacustrine carbonate formation using data from 25 European and Anatolian lakes of varying salinity and hydrochemistry. Temperature, pH and ion concentrations are the main factors that control the type of carbonate minerals that are formed. The precipitation of primary carbonates (calcite, high-Mg calcite, aragonite, hydrous Mg carbonate) and secondary carbonates (proto-dolomite, dolomite, Huntite, magnesite) depend on the Mg/Ca ratio of the lake and pore waters. Secondary carbonates along with high-Mg calcite appear in lakes where the mentioned ratio is >7, a total water salinity is high and changes significantly during a year. Although the definition of the proto-dolomite is not fully settled yet in carbonate sedimentology (Müller, 1970; Gaines, 1977; Fang and Xu, 2019), the proto-dolomite is considered to be a mineral where the composition approaches that of the dolomite mineral, yet only a partial structuring of Ca^{+2} and Mg+2 is notable in its lattice (Müller and Wagner, 1978; Tullner and Cserny, 2003; Chen *et al.,* 2017).Proto-dolomite forms in a mud deposited on a lakebed via a transformation of Mg-bearing calcite during periods when pore waters are especially rich in Mg (Müller *et al.,* 1972; Gaines, 1977; Müller and Wagner, 1978; Fang and Xu, 2019). Such conditions generally emerge during the fall in the ponds of the DTI. The total dissolved solids (TDS) content of the groundwaters of the DTI is relatively high (500–2000 mg/l in general, sometimes >5000 mg/l). Due to high summer temperatures and minimal rainfall, strong evaporation reduces the lake levels. As the lost water is recharged from the groundwater, the TDS of the lake water further increases to values between 8000–70,000 mg/l, turning these ponds highly saline (Molnár and Murvai, 1976; Molnár and Szónoky, 1976; Molnár *et al.,* 1995; Molnár, 1996). From the ions present, sodium is dominant in addition to calcium, magnesium, and hydro-carbonate making the water highly alkaline with pH ranging

between 9–11. Groundwater also drops to 3–8 m depth and many of the lakes dry up by the end of summer (Molnár, 1991).

Precipitation during the fall brings in freshwater reducing salinity, and the concentration of Na and K allowing for an increase in Mg/Ca ratio to values between 7–12, leading to the precipitation of high magnesium calcite (Molnár, 1961, 1970, 1981, 1983, 2015; Bender *et al.,* 1975). As a result, the Mg/Ca ratio further increases in the remaining pore waters bringing about the early diagenetic alteration of the high magnesium calcite into a proto dolomite (Mucsi, 1963; Molnár, 1970, 1980, 1983, 1985, 1991). As the ratio of CO_3/Ca is higher than 1, these conditions also favour the formation of dolomite. Where the lacustrine phase of carbonate precipitation ended, seasonal migration of the pore waters saturates the matrix and fills up the pores with minerals precipitating from the remaining solution (calcite, limonite), turning the carbonate mud into solid rock. Due to the smaller Mg/Ca ratio attributable to the exhaustion of magnesium during the proto-dolomite, dolomite formation and reduced salinity of the pore waters, the pore-filling cement is calcitic in composition (Molnár, 1970, 1980, 1983, 1985, 1991). Thus, in the freshwater carbonates of the DTI, the precipitation of the carbonate matrix reflects the evolution of the lacustrine system itself, while the formation of the carbonate cement infilling the pores is a secondary process carrying information on the diagenesis.

The formation and diagenetic history of sedimentary rocks is expressed in their composition that is distribution of its major rock-forming components (RFC). To understand and assess the nature of these processes and resulting spatial heterogeneity, one needs quantitative information on the distribution of RFCs at the macro and micro-scale. Analysis of texture characters of carbonate sedimentary rocks of the interfluve area has been extensively studied both at the macro (hand specimen) and micro-scale (thin sections) (Molnár, 1961, 1970, 1980, 1983, 1985, 1991, 1996; Mucsi, 1963; Molnár and Murvai 1976; Molnár and Szónoky, 1976; Molnár *et al.,* 1995). For estimating RFC proportions at the micro-scale, a simple counting of visible RFCs in thin sections using overlaid grids is a long-used, well-established technique. The quantitative information gained in this way has certain limitations though. Firstly, it is two-dimensional, spatially heavily restricted representing only a minor fragment of the entire sample, i.e., the scale of the area covered by the thin sections. In addition, estimations are rather subjective. Several different RFCs are present within a single grid cell, so correct filtering of

the individual components and estimation of their proportions in the grid is not without a bias. Computer Tomography (CT) analysis however provides us quantitative data in 3D at both the scale of the entire sample and a resolution defined by dimensions of the voxels in the micro-scale. The quantitative data expressed in Hounsfield units (HU) correlates with the density of RFCs. Thus, its statistical properties also record information on their heterogeneity. This work presents results of a detailed quantitative analysis of data gained via CT analysis.

II.2. GEOLOGY AND STRATIGRAPHY

The DTI forms a wind-blown sand and loess-covered ridge (180 km long and 120 km wide, 100–150 m a.s.l.) between the Danube and Tisza rivers in central of Hungary (Fig.II-1a). To the west, the area is bordered by the tectonic depression of the Danube valley lying at 90–100) m a.s.l. The 10–15 km wide valley of the Tisza River (80 m a.s.l.) forms the eastern boundary of the area. The bedrock of the DTI is given by alternating loess and wind-blown sand sequences representing the reworked fluvial deposits of the Danube.

During the Holocene prevailing winds arranged the sand into a series of dunes with an NW to SE trend. The interdune depressions are occupied by natron lakes characterized by freshwater carbonate formation, supplied with water primarily from groundwater flowing from the Danube valley in the west towards the Tisza valley in the east (Fig. II-1b) (Molnár and Murvai 1976; Molnár and Szónoky, 1976; Molnár *et al.,* 1995). Our study site at Csólyospálos located on the southeastern side of the DTI (Fig. II-1a, b) represents one of such interdune lacustrine systems where carbonate formation starting at the beginning of the Holocene came to an end about 3500 years ago (Jenei *et al.,* 2007; Sümegi *et al.,* 2015; Sümegi & Náfrádi, 2015). The outcrop is situated ca. 2 km northeast of the village of Csólyospálos at 92 m a.s.l. A geological profile created in the centre of the Late Pleistocene interdune depression exposes a ca. 1 m thick carbonate sequence covered by the Late Holocene black earth soils. The former pond is flanked by the Holocene dune in the SE (Fig. II-1c, d). The carbonate sequence overlying the bedrock of the Late Pleistocene wind-blown sand is comprised of a lower lithified and an upper non-lithified part. Based on its observed lithological features the sequence was subdivided into 5 members (Fig. II-1c, e) (Molnár, 1961, 1970, 1980, 1983).

The member Cs-1 (corresponds to the Molnár's member A) is a sandy dolomitic limestone of looser structure with vertical veins stained by red limonite. It is 20–30 cm thick. This unit

transforms into the member Cs-2 (corresponds to the Molnár's member B), with no clear boundary at the top. Cs-2 is a solid light-grey dolomitic limestone, 30–40 cm thick with vertical vugs of several cm corresponding to roots of the former aquatic vegetation, hence its folk name is honeycomb stone. There is a sharp lithological boundary between the member Cs-2 and the overlying member Cs-3 (corresponds to the Molnár's member C). Cs-3 is a solid dark-grey dolomitic limestone, 5–8 cm thick, with the highest carbonate content in the entire sequence (>80%). Here vuggy and moldic type porosity is present in a form of shelter, gas pores and desiccation or sheet cracks in addition to vugs corresponding roots of a former vegetation. In some pores, the intrusion of not fully consolidated carbonate mud is also visible. Most of the pores are partially or completely infilled by calcisparits. Pore filling starts perpendicularly to the pore wall forming pore-lining structures. The member Cs-4 (corresponds to the Molnár's member D) is the last carbonate member with an average thickness of 30–60 cm. In contrast to the previous members, Cs-4 is non-cemented with carbonate mud of bright white colour. The highest vol- ume of unfilled pores, as well as carbonate clastic grains, appear here. The carbonate content is about 50–60%. Based on textural analyses implemented using thin sections, the carbonates are wackestone type with a mud-supported texture. Rock-forming components are dominantly micrite (~69%), quartz and feldspar grains (~13.6%), unfilled pores (to ~12%), carbonate lithics (~3%) and microsparite infilling pores (2.4%). Shells of freshwater gastropods and oogonia of calcareous algae are also present in minimal proportions similarly to additional contaminants of iron oxides, manganese, fine organic and clay particles (Molnár, 1961, 1970, 1980, 1983, 1985, 1991, 1996; Molnár and Murvai 1976; Molnár and Szónoky, 1976). The density of the rock ranges between 2.729 and 2.790 g/cm3, with porosities of 25.77–29.82% (Mucsi, 1963), depending on dolomite and iron-oxides, manganese content as well as the cementation degree.

II.3. MATERIAL AND METHODS

II.3.1. Computer Tomography

X-ray CT imaging is a non-destructive examination technique, based on measuring the penetrating radiation intensities over several paths of a sample to produce cross-sectional tomographic views based on density differences. The first use of CT was for medical purposes (Kenter, 1989), then it has been widely used in various sciences such as archaeology,

palaeontology, and sedimentology (Földes *et al.,* 2004; Markussen *et al.,* 2019). The CT technique was used in the early 1980s for scanning meteorites, detecting soil porosity, and analysing sediment morphology. Moreover, the CT technique was employed in palaeontology to scan the irreplaceable fossils in the mid-1980s (Cnudde *et al.,* 2006). Later on, the same technique was used in detecting rock-faulting by the early 1990s. Recently, the micro-CT method was employed first in a laboratory experiment related to structural geology in 2000.

In general, the CT technique is highly sensitive to density changes or any variation in chemical, physical or biological properties of materials (Maurício *et al.,* 2017). For this reason, post- or syndiagenetic sedimentary structures can be easily detected visually on CT scans (Wilding *et al.,* 2005). Thus, this technique is widely used in the studies of clastic rocks. However, a limited number of works have been conducted on carbonates (Hicks *et al.,* 1994). The most important feature of the CT analysis, besides visual evaluation, is however the data behind, which carries

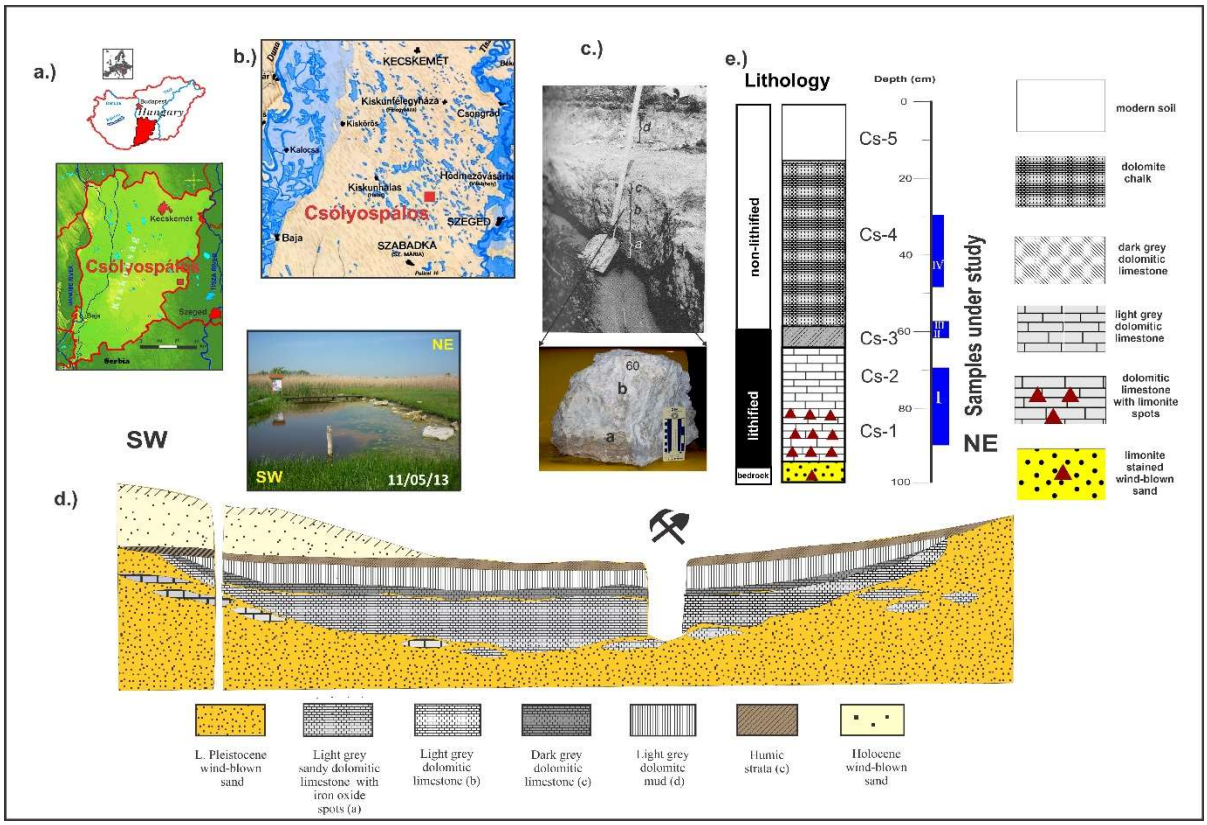

Figure II–1: Location and stratigraphy of the studied carbonate sequence at the site of Csólyospálos. (a. location, b. hydrography of the area before the late 19th century, c. photograph of the 1970 profile by Molnár with his names of the lithological members, d. geological cross-section of the site and view of the outcrop during early spring e. detailed lithology of the outcrop with the position of samples under study marked)

Table II-1: List of samples with Field of view (FOV) for the entire sample and representative voxel size parameter

Samples with stratigraphic position	FOV	Voxel size
	(mm)	(mm^3)
I	669,866	0.08
(Members Cs-1, Cs-2)	(95.5*22.7*309)	
II	305,375	0.08
(Member Cs3)	(79.5 *132 *29.1)	
III	175,882	0.04
(Member Cs-3)	(138*23.3*54.7)	
IV	518,583	0.08
(Member Cs-4)	(76*159.8*42.7)	

quantitative information on density differences observed between rock-forming textural components in a material. These can be thus assessed using various statistical approaches (De Boever *et al.,* 2015). The CT measurements were performed on 4 samples representing all members of the carbonate sequence of Csólyospálos (Cs-1, Cs-2, Cs-3, Cs-4, and Cs-5), using the Siemens Emotion 6 medical scanner at the Department of Radiology, University of Pécs, Hungary. A single sample (sample I) represents the members Cs-1 and Cs-2. Two adjacent samples (sample II and III) were taken from the member Cs-3 and an additional single sample (sample IV) represents the member Cs-4 (Fig. II-1). The CT instrument operates at 140 kVp (peak kilovoltage), with 189 mAs (milliampere-seconds) current and 1.5 s exposure time. The lateral resolution was 0.23 × 0.23 mm^2, with 1.5 mm of scan-layer thickness. The CT images have been exported as DICOM. A 3D volume rendering software used for visualization, filtering, and data extraction. Details on Field of View (FOV) for each sample and the representative voxel sizes are presented (Table II-1).

II.3.2. The workflow applied.

The visual output of CT allows for straightforward interpretation via comparison with the original sample and the available macroscopic lithological descriptions (Fig. II-2). However, certain scanning artifacts like beam hardening can obscure details of interest or cause the CT value of a single material to change in different parts of an image. To overcome this problem the outer part of the image has been removed creating a CT brick (subset) smaller in volume

than the original sample (filtering) (Fig. II– 2). Thus, only the created central sub-volume of the original sample was used for further visual and quantitative analyses.

Data extracted from the brick were used in further statistical analysis using the software packages STATGRAPHIC and PAST4.06 (Hammer *et al.,* 2001). Distribution types were visually assessed using histograms and boxplots to identify potential outliers and extreme values present in samples (Fig. II–2).

Univariate statistical parameters (Mean, standard deviation, skewness, kurtosis) have been used to characterize each sample. As our samples assumed to represent a pool of normally distributed populations corresponding to the rock-forming components, the maximum-likelihood method of mixture analysis has been adopted to recover and estimate the parameters of two or more univariate normal distributions (Mean, STD) in Past 4.06 (Fig. II–2). The method is based on the Estimate Maximumlikelihood (EM) algorithm of Dempster et al. (1977). To see if the number of groups chosen is appropriate and avoid overfitting, the Akaike Information Criterion (AIC; Akaike, 1974; Hammer *et al.,* 2001) is calculated. Each data point has been assigned to one of groups using a maximum likelihood approach. This can be used as a non-hierarchical clustering method for univariate data.

The statistical parameters gained for each subpopulation have been used to set HU value intervals. Using the gained parameters of the Mean ± 2 STD, the recovered subpopulations are visualized, and their lithological Meaning is assessed relying on the descriptive geological reports and thin sections of (Molnár *et al.,* 1976; Molnár, 1980, 1981). HU intervals set for each Meaningful sub-population using the referred statistical parameters can be regarded to quantitatively describe rock-forming components present in samples. Knowing the original volume of the studied and filtered subsamples, the percentage of each identified rock-forming component (e.g., calcitic matrix, filled pores, etc.) can also be estimated. The proportions of each rock-forming component calculated can be compared to those defined by Molnár et al. (1976) and Molnár (1980, 1981, 1991), based on multiple thin sections taken from selected parts of samples. However, the adoption of quantitative CT analysis and 3D visualization has several significant advantages over the traditional approaches of Molnár et al. (1976) and Molnár (1980, 1981, 1991).

Thin section analysis allows for the characterization of a very small volume of sample. Furthermore, even if multiple thin sections are prepared, they capture only a very small part of

the entire block sample. In contrast in the CT analysis, the percentage and spatial distribution of each rock-forming component can be assessed for the entire CT brick allowing to reveal small scale vertical and horizontal heterogeneity present.

II.4. RESULTS

II.4.1. Sample I, members Cs-1 and Cs-2

Sample HU values follow a univariate, slightly negatively skewed leptokurtic distribution (MD: 2560, STD: 255, SK: -1.4, K: 9.3). The single peak with the value of 2382 HU is close to the Mean value of sample, reflecting the general dominance of a single rock-forming component (matrix) (Fig. II-3).

Based on results of the mixture analysis 5, overlapping intervals can be distinguished with densities ranging between zero and 3939 HU (Fig. II–3). Group A has values lower than 626 HU. Group B has values between 277 to 2245 HU. Both groups appear as outliers and extreme values on the boxplot. When we look at the shape, structure, and spatial distribution of the rock-forming components characterized by these intervals, they appear as isolated or interconnected longitudinal tubular or spherical, lenticular structures on the 3D CT brick (Fig. II-4). When compared with the original sample photos, general textural descriptions of Molnár (1981, 1983, 2015) as well as photos of thin sections (Fig. II-4), these must correspond to the pores present in sample. According to Molnár (1981, 1983), most of the pores are vugs, intergranular and moldic pores. Vugs corresponding to roots of the former vegetation appear in various forms and orientation. These connected or isolated tubes are either scattered in the matrix independently of lamination or cross-cut bedding planes. Horizontal desiccation pores also turn up in addition to randomly scattered gas pores. Some pores are empty while others are partially filled by calcite sparite or microsparite. These are also clearly visible on the enlarged photo of the middle part of sample and the thin sections (Fig. II-4). Group A corresponding to the values zero –626 HU thus represents the empty pores, while that of 277–2245 HU (group B) corresponds to the pores partially filled by calcite due to diagenetic processes (Fig. II-4). As seen in the lower left figure (Fig. II-4), a spiral-like structure also turns up (G) corresponding to the shell of an aquatic gastropod. Pore lining calcite crystals are common in empty gastropod shells, in addition to matrix intrusions (Fig. II-4).

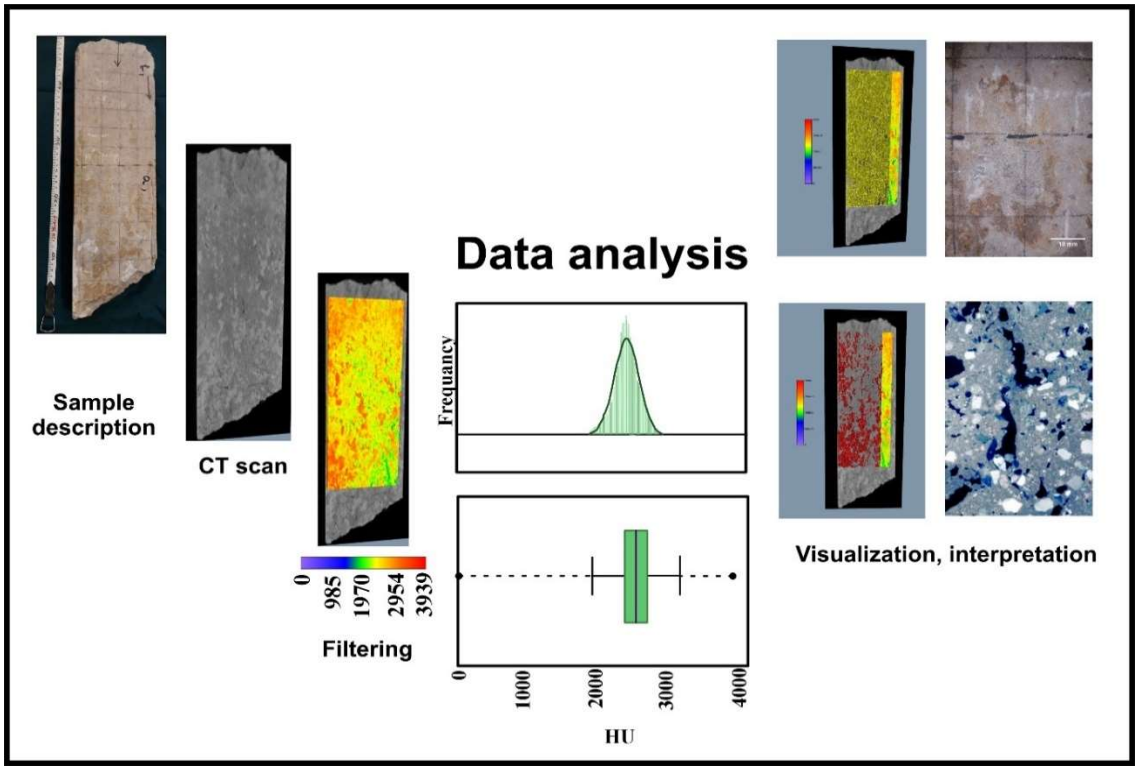

Figure II–2: The general presentation of the workflow.

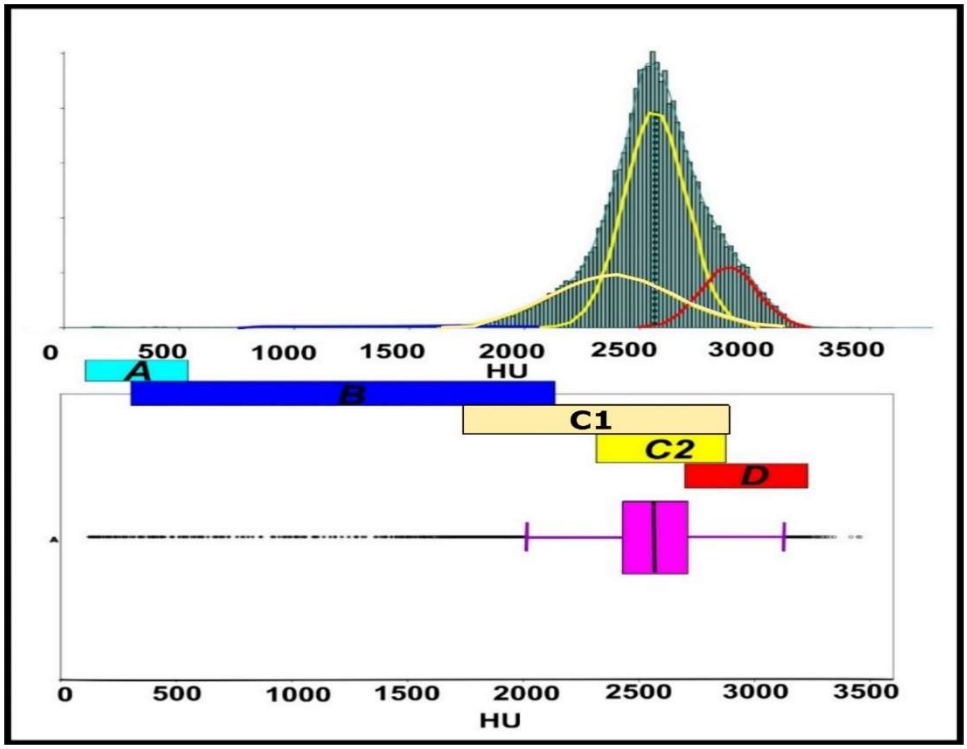

Figure II–3: Statistical characteristics of sample I and revealed subpopulations (A, B, C1, C2, D) represented by overlapping normal distribution curves on the frequency histogram.

Group C with values between 1900–3125 HU gives ca. 75% of sample (IQR + whiskers of the boxplot) and can be divided into two subgroups (Fig. II-3), with a lower (C1: 1869–2896 HU) and higher density (C2: 2299–2832 HU). As the dominant component of sample is the micrite, C1 and C2 must correspond to the matrix with differing densities. Group C1 overlaps with group B, which we interpreted as the calcitic fill of the pores. This way, C1 must correspond to the dominant calcitic matrix. Consequently, C2 must correspond to the matrix composed of dominantly higher density minerals (dolomite micrite). Group D is defined by values between approximately 2500 to 3500 HU, showing the highest density component in sample appearing as the upper outlier on the boxplot (Fig. II-3).

Morphology, orientation, and spatial distribution of the features defined by the mentioned D interval are very much like those defined by the intervals A and B (pores), displaying lenticular and vertical tubular structures running parallel to one another (Fig. II-5/2). This material appears as dark-brown spots on sample photo representing the limonite saturated matrix (Fig. II-5), probably formed as a precipitate in the pores and the matrix during the diagenesis phase.

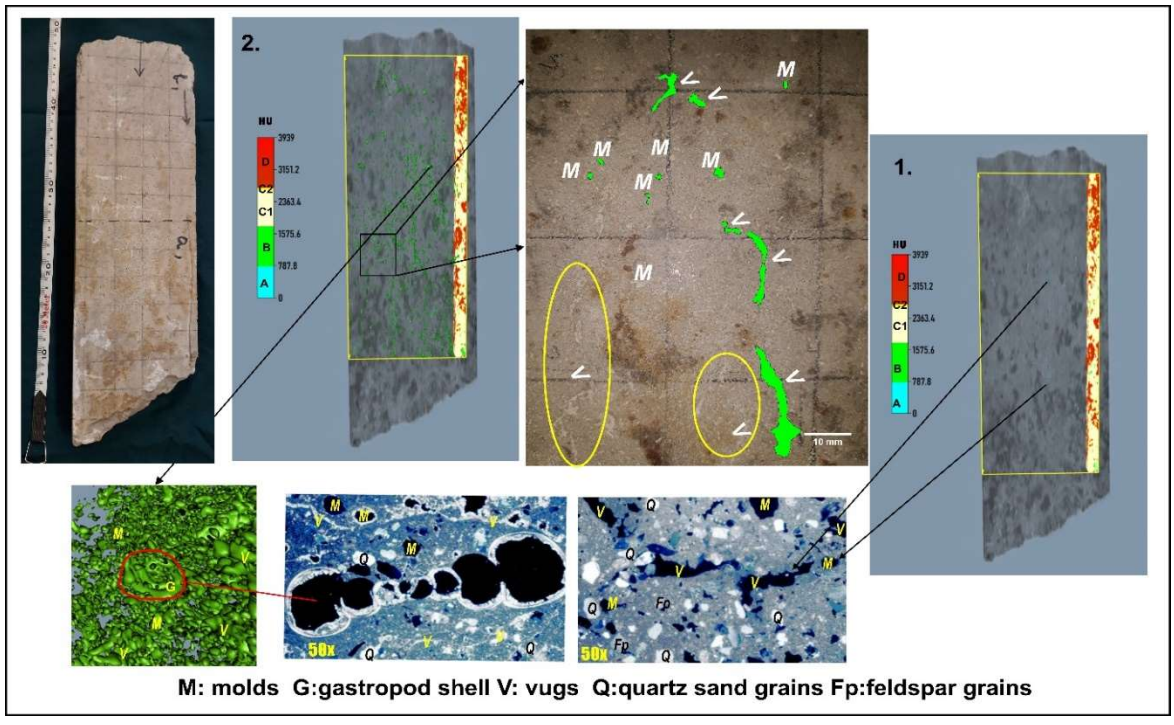

Figure II–4: The visual appearance of group A (1) and B (2) on the CT blocks of sample I and examples of corresponding textural components depicted on sample photos (centre) and selected thin sections.

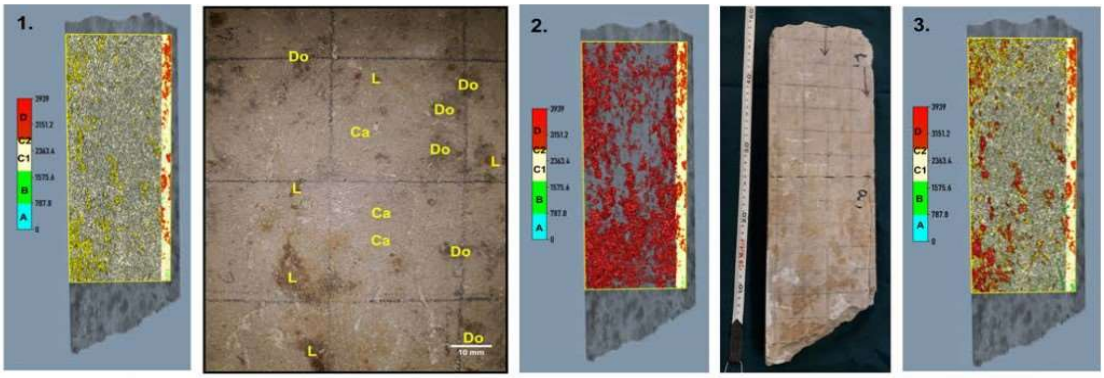

Figure II–5: The visual appearance of HU intervals of group C1, C2 and D on the CT block of sample I (1, 2), combined visualization of matric (C) and the high-density limonite saturated matrix compound (D) (3).

II.4.1. Samples of the member Cs-3

II.4.1.1: *Sample II*

Sample HU values follow a bimodal slightly negatively skewed distribution (MD: 2787.3 HU, STD: 334.23, SK: -1.421, K: 2.365) with a marked peak at 3150 and a shoulder at 2750 HU reflecting the dominance of a high-density and a mid-density component, the latter being close to sample Mean (Fig. II–6).

According to the results of mixture analysis, five overlapping groups could have been differentiated in sample, characterized by a relatively wide range of densities between 0 and 3500 HU (Fig. II–6).

Group A has values lower than 1386 HU. Group B has a wider distribution with values between 1387 and 2749 HU (Fig. II–6). If we visualize the RFCs corresponding to these intervals on the CT brick, they appear to form a network of interconnected and isolated spherical and tubular structures (Fig. II-7/1, 2). Based on their shape, they may represent various types of pores. As seen on the thin section and the surface photo of sample (Figs. II-7, 8), two types of pores are present: molds and vugs. Molds turn up as spherical elongated isolated structures in the brick for the defined interval. In addition, you can see long tubular structures, some of them

being isolated, others being interconnected. These probably correspond to vugs. In addition, both molds and vugs can be further divided into two subgroups: relatively empty ones (Figs. II-7, 8) and the other ones which are fully or partially filled with secondary calcite crystals, and in some cases by the matrix material. Filled pores appear as red-stained crystals on the Na alizarine sulphonate dyed thin sections (Fig. II-8) and as white crystals on the surface photo of sample. It is also visible on thin sections that some crystals form pore-lining structures. When values for the group B are visualized essentially, the same morphologies and orientation appear as in the case of the group A (Fig. II-7/1, 2). Based on the previously mentioned information, both groups A and B correspond to pores in sample, the denser one (B) most likely indicates the presence of additional minerals, besides air-so partially or filled pores.

The figure in the upper left corner (Fig. II-8) depicts a close-up view of the CT brick of sample II. Here the marginal areas of the vugs found in the upper right and right center have values corresponding to group B. These must represent pore-lining calcite crystals.

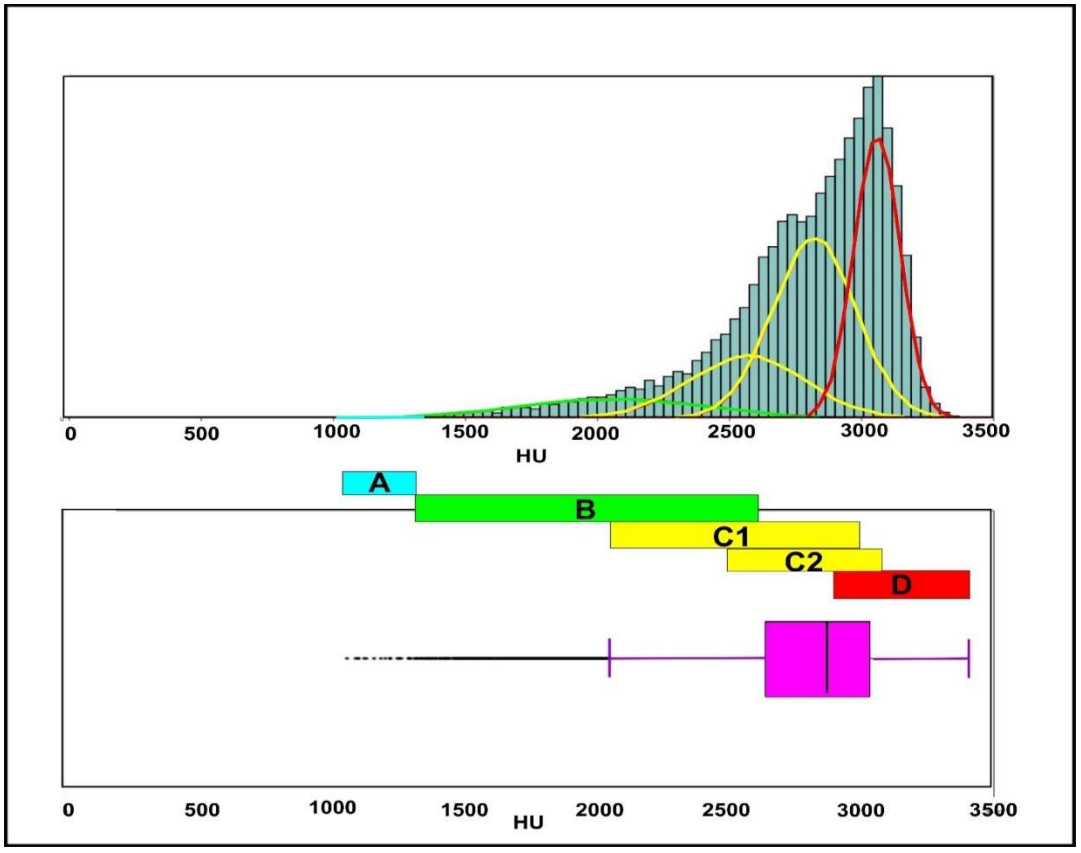

Figure II–6: Statistical characteristics of sample II revealed subpopulations (A, B, C1, C2, D) represented by overlapping normal distribution curves on the frequency histogram.

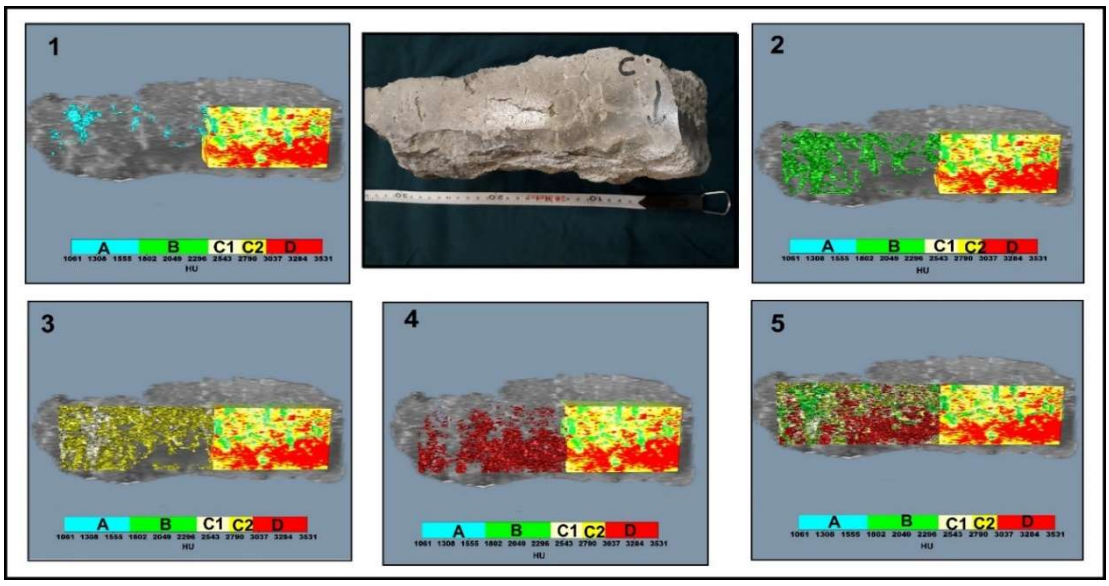

Figure II–7: : The visual appearance of identified subpopulations (A, B, C1, C2, D) on the CT block of sample II (1: empty pores (A), 2: calcite-filled pores (B), 3. C1: matrix of dominantly calcite micrite, C2: matrix of dominantly dolomite micrite, 4: limonite and manganese saturated micrite (D) 5. combined textural components).

The middle part of these vugs, though with values corresponding to group A, represents parts with the least dense component. Similar structures appear along the central line of the surface sample depicted on the upper right photo (Fig. II-8), where the marginal areas of the vugs have white crystals and the central part is empty. There are other tubular or spherical structures as well, with values corresponding to group B. These again can be interpreted as pores filled by higher density calcite crystals. All these observations further corroborate our previous interpretation that these two components (A, B) should represent the empty and partially filled areas of pores. Molds are not evenly spread in the brick but appear in higher densities in the top part (Figs. II-7, 8). Vugs are also scattered, most of them being restricted again to the top part (Fig. II-8) and in some cases, the lower left part of the CT brick (Figs. II-7, 8). The orientation of the vugs is dominated by vertical crosscutting laminae.

The third group (Fig. II-6C) corresponds to the interquartile area on the boxplot, indicating that this group gives a major part of the rock-forming components, i.e., the micritic matrix. Group C is characterized by two overlapping modes (C1, C2) indicating presence of two micritic components with different densities: a lower (group C1: 2117–3001 HU) and a higher (group C2: 2501 HU and 3136) ones. The material covers most of the sample (Fig. II-7/3), indicating

that the major component is a carbonate matrix composed of lower density calcitic micrite and higher density dolomitic micrite, appearing in the figure in light yellow and dark yellow colour.

The last group (D) has the highest density values in sample (2884–3235 HU). We can extend the upper boundary of this interval to the maximum value of sample (3404 HU). Due to the overlap of group D with group C, which we interpreted as the matrix, this group must also represent a part of the matrix, where the presence of an even higher density material must be assumed. When group D is visualized on the CT brick, this part of sample corresponds to the dark gray-brownish lower part (Figs. II-7, 8), representing a geochemical front (GF) where precipitates of dark-brown limonite and dark-grey dolomite stain the rock.

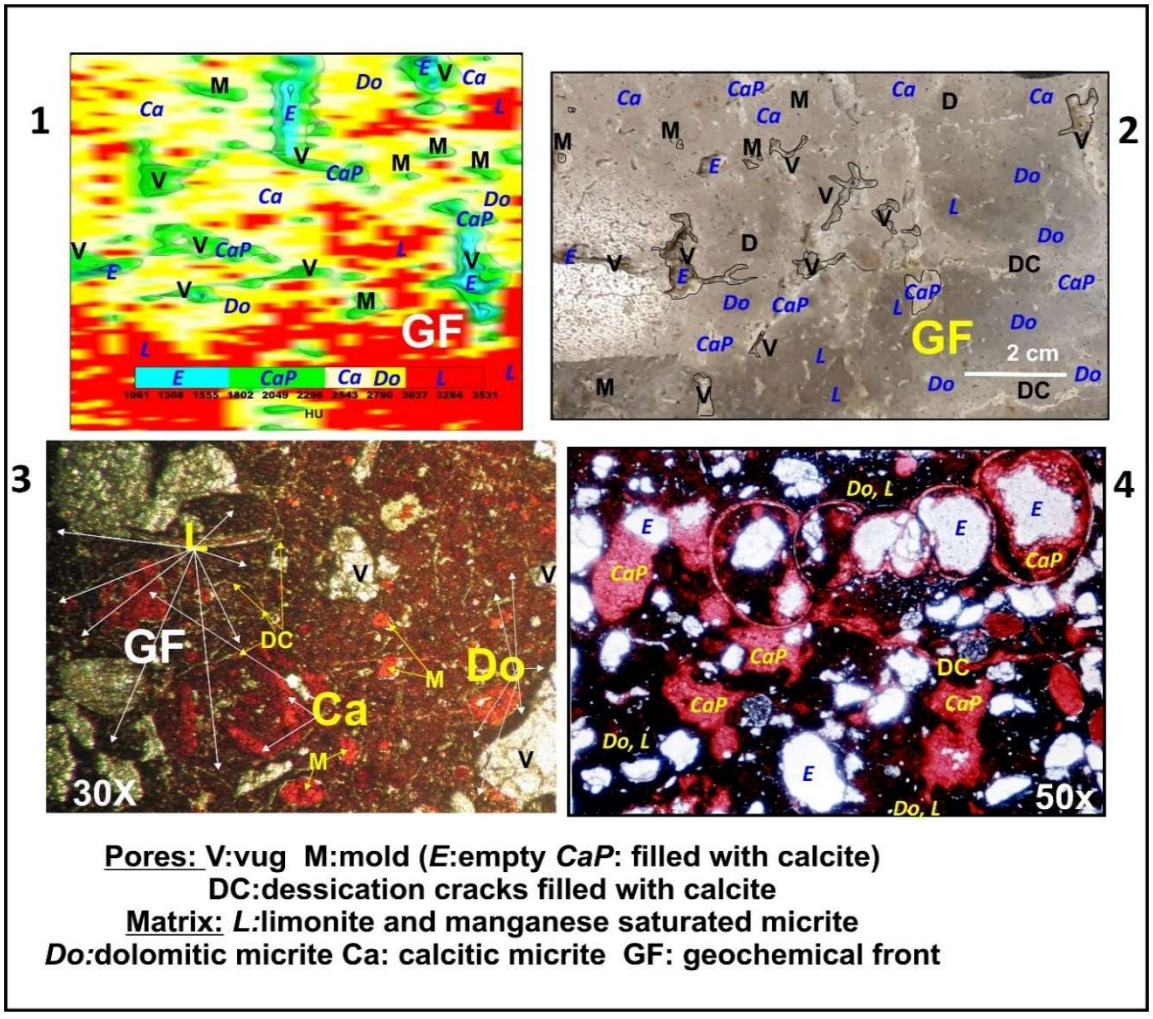

Figure II–8: Close-up view of sample II with different macro and micropores depicted on the CT block (1,3), sample surface (2), and under the microscope (4). (E: empty pores, Cap: calcite filled pores, Ca: matrix of dominantly calcite micrite, Do: matrix of dominantly dolomite micrite, L: limonite and manganese saturated micrite, pore Types-V: vugs (plant roots, plant stems), DC: desiccation cracks, M: molds (gas pores).

It is interesting to note that in some places of the geochemical front, the limonite stained micritic matrix (L-red) is surrounded by the dark-grey dolomitic matrix (Do: dark yellow). The light grey calcitic matrix Ca is concentrated in the top part of sample. In the case of the partially filled pores, most calcite appears as pore-lining crystals (Fig. II-8).

II.4.2.2 *Sample III*

Sample HU values are characterized by a slightly negatively skewed, multimodal leptokurtic distribution (MD: 2510.27, STD:741.46, SK: -1.75, K:2.55), with multipeak at the lower and upper ends (first one at 327 HU, reflecting the lower density component). The largest peak is at 2757 HU, close to sample Mean, with another peak at the right shoulder at 3188 HU reflecting the dominance of the highest density components in sample (Fig. II-9). Multiple peaks on the histogram indicate the presence of multiple rock-forming components with significantly different proportions than in the previous sample.

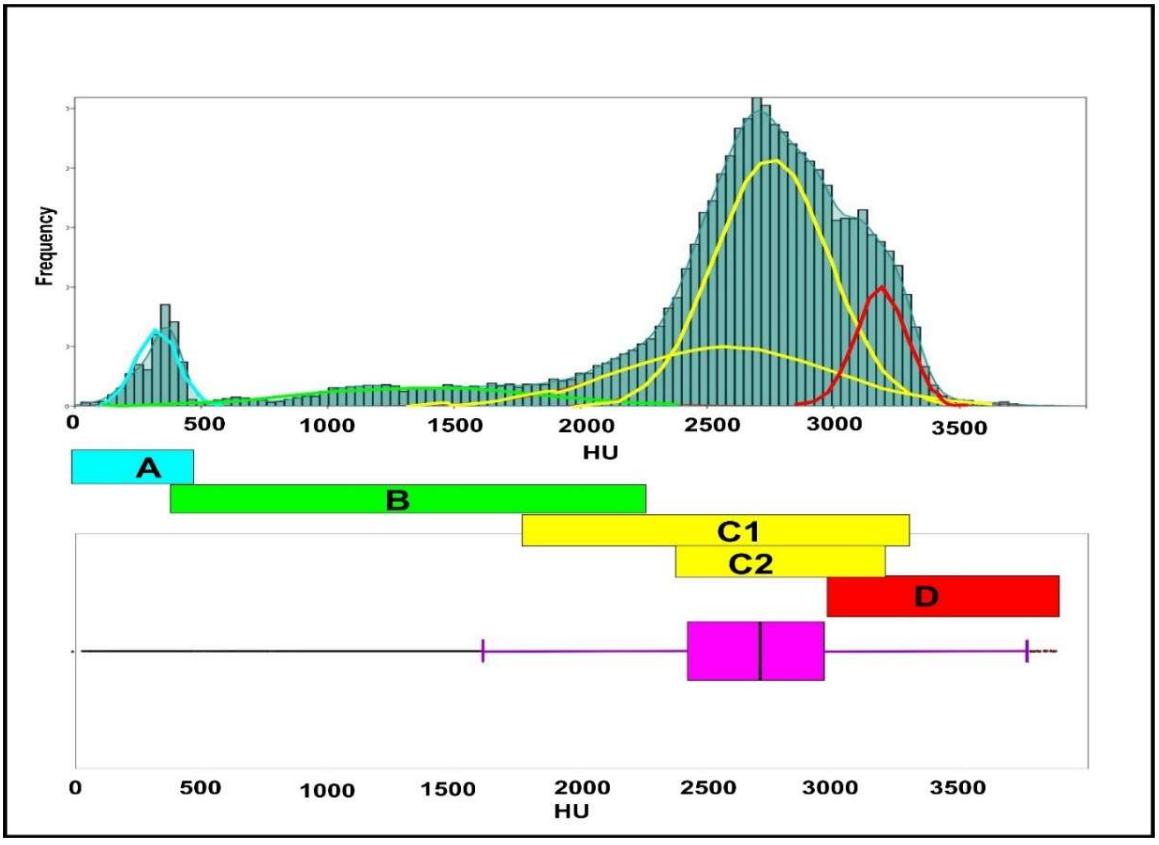

Figure II–9: Statistical characteristics of sample III and revealed subpopulations (A, B, C1, C2, D) represented by overlapping normal distribution curves on the frequency histogram.

There are 5 overlapping groups characterized by slightly different densities with a wide distribution between 0 and 3867 HU in sample. The first group (A) is <490 HU. Group B has a wider range between 122 to 2350 HU. When we check the RFCs related to these intervals on the 3D brick from the CT scan, they appear to form a network of isolated and interconnected spherical and elongated tubular structures (Fig. II-10/1). In our view, they correspond to various types of pores, moldic pores appearing as spherical elongated and vuggy pores appearing as tubular structures.

The third one (group C in Fig. II-10/3) corresponds to the interquartile area on the boxplot of Fig.II-9 indicating that this group gives a major part of the rock-forming components. Group C is characterized by two overlapping modes (C1, C2) referring to the presence of two dominant components with lower (group C1: 2163–3193 HU) and higher densities (group C2: 2757 HU and 3208 HU). The yellow-colour RFC with values of group C on the CT brick corresponds to the upper light-grey area of the original sample (Fig. II-10/3) and represents the carbonate matrix consisting of lower density calcitic micrite and higher density dolomitic micrite.

Sample largest density values are found in the last group (D) (3088–3388 HU). We can expand the top border of this range to sample the greatest value (3938 HU). While group D overlaps with group C, which we regarded as the matrix, this group must also represent a component of

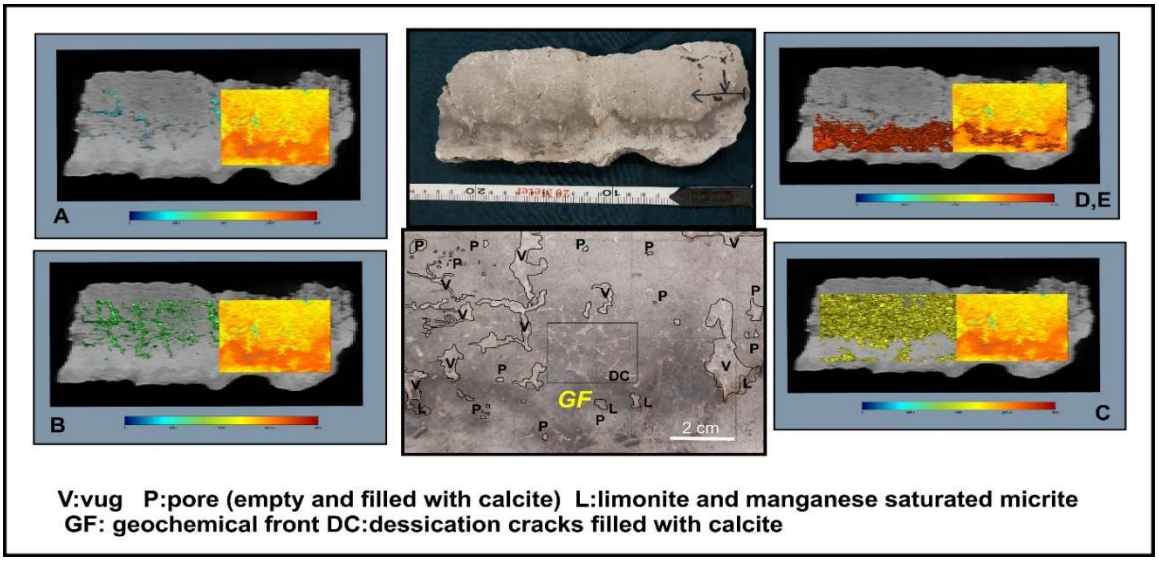

Figure II–10: The visual appearance of identified subpopulations (A, B, C1, C2, D) on the CT block of sample III (1: empty pores (A), 2: calcite filled pores (B), 3. calcitic and dolomitic matrix (C1, C2), 4: limonite and manganese saturated micrite (D).

the matrix, implying the presence of a higher density substance. When group D is visualized on the CT brick (Fig. II-10/4), there is a perfect match with the dark grey-brownish bottom part of the original sample representing a geochemical front (GF) of the limonite, saturated dominantly a dolomitic matrix just like in sample II.

II.4.2. Sample IV, member Cs-4.

The last member of the profile is characterized by a bimodal (MD: 1934, STD:355, SK: -1.16E+04, K:720), negatively skewed and highly peaked distribution, indicating low density (292 HU) and dominance of a high-density component (1985 HU), close to sample Mean (Fig. II-11).

Based on the mixture analysis results (Fig. II-11), 5 overlapping groups with a density between 0 and 3160 HU could also be distinguished. Group A is characterized by values <537 HU. Group B has a broader distribution between 336 and 1907 HU. Visualizing the RFCs, regarding these intervals on the CT brick, they represent a network of interconnected spherical and tubular structures that can be interpreted to be pores, just like in the case of the previous

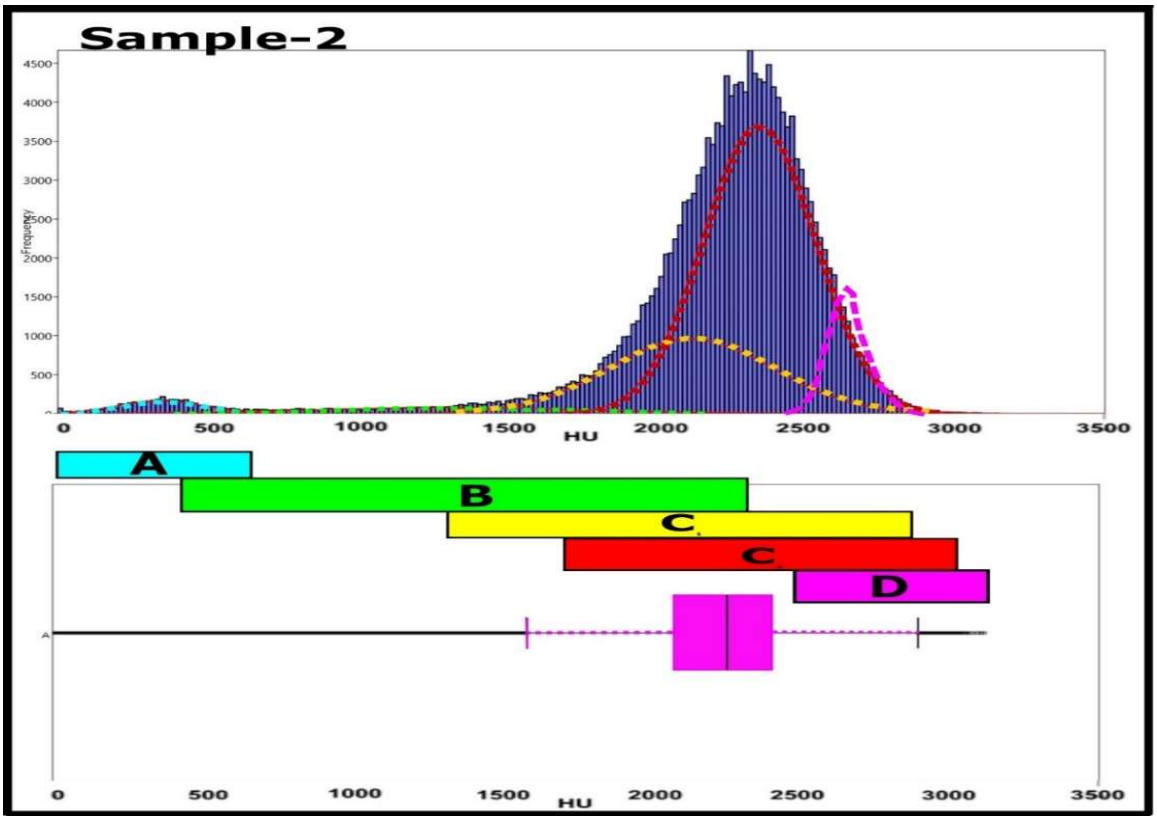

Figure II–11: Statistical characteristics of sample IV and revealed subpopulations (A, B, C1, C2, D) represented by overlapping normal distribution curves on the frequency histogram.

samples (Fig.II-12/1, 2). There are different types of pores regarding their shape, also clearly visible in the thin section: molds and vugs (Figs. II-12, 13).

In a thin section, pores appear in various states: empty pores belong to the first group A, partially filled with crystals lining over the border of the pore during early diagenesis, almost fulfilled with crystals during the early diagenesis, based on the pore water chemistry. Therefore, group B extends widely from low (almost empty pores) to higher density (filled or partially filled with calcite.

The next group C can be divided into two main subgroups (C1, C2), the first one (C1) ranging from 1328 to 2261 HU (Mean: 1794 HU). As this interval partly overlaps group B which we interpreted as pores filled with calcite crystals, group C1 must represent the matrix with a larger proportion of a calcite micrite too. The whole higher density part overlapped with the last interval. Most RFCs were found in groups C1 and C2. Group C2 distributed between 1669 to 3160 HU. On the boxplot, the interquartile area and both whiskers represent groups C1 and C2. Thus, the RFCs of these groups are probably a calcitic micrite mud and a dolomitic micrite mud. As there is a large overlap between these groups; some of the dolomites may be assumed to have precipitated into the pores from a high magnesium content in porewater, in addition to development of a dolomite mud from a calcite mud by entering Mg^{++} to mineral crystals.

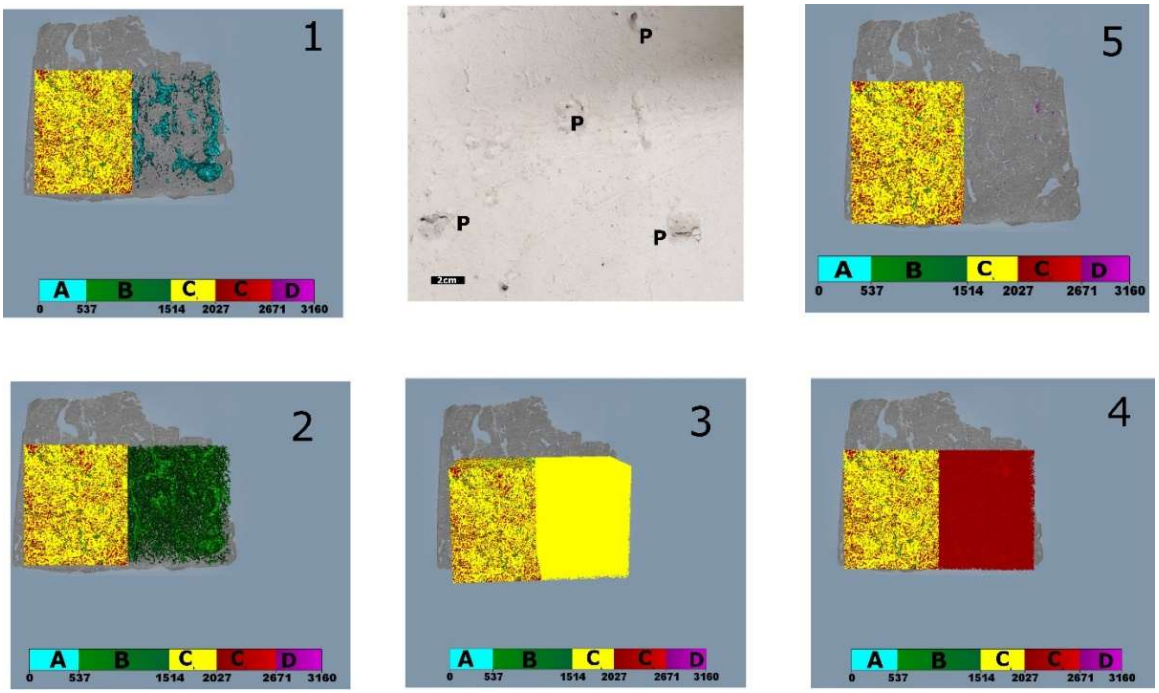

Figure II–12: : The visual appearance of defined HU intervals (A, B, C1, C2, D) on the CT bricks of sample IV (1: empty pores (A), 2: filled pores (B), 3: matrix of dominantly calcitic micrite (C1), 4: matrix of dominantly dolomitic micrite (C2), 5: Limonite and manganese saturated micrite (D)). P is surface pores

The last group of this sample is group D with values ranging between 2560 to 3160 HU, which corresponds to the highest density components such as Fe^{+2}, Fe^{+3}, Mn^{+2} and Mg^{+2}, transported by groundwater fluctuation or dissolved by meteorite water during surface runoff.

II.5. ESTIMATED PROPORTIONS OF RFCs.

Based on our calculations, pores give ca. 0.29% of the total volume in sample I. The proportion of empty pores is negligible around ~0.11%. According to Molnár (1981, 1983), most of the pores are vugs, intergranular and moldic ones. All types are observed in sample (Fig. II-4). As was seen in our CT blocks, vugs corresponding to roots of the former vegetation appear in various forms and orientation. The concentration of these features is generally highest in the member Cs-1 and much lower in the member Cs-2. Their proportion is minimal in the transitional zone of the two members. Looking at the photos depicting the original samples (Fig. II-4), the mentioned features correspond to the dark grey and dark-brown areas, representing dominantly pores infilled with limonite and manganese saturated micrite. These minerals infilling pores precipitated during seasonal fluctuations of the groundwater. In the studied volume, 90% represents a matrix, 27.18% of which is composed dominantly of the lower density calcitic micrite and 56.88% is given by the higher density dolomitic and limonite saturated micrite (Fig. II-14), with a shear dominance of the highest density micrite (15.62% on the average). It must be kept in mind that the densest part of the matrix is composed of high-density minerals (dolomite, limonite), plus a larger proportion of higher density clastics (quartz, feldspars, clays).

Based on the results of detailed XRD investigations (Molnár *et al.,* 1976; Molnár, 1991, 2015), both members Cs-1 and Cs-2 are classified as dolomitic limestone or mud-supported wackestone according to Dunham (1962). Although a general chemical composition of members Cs-1 and Cs-2 is quite similar (74–77% $CaCO_3$ and 19.4–22.3% $CaMg(CO_3)_2$), previously published results of thin-section analyses of both members highlighted significant variations in the proportion as well as the mineralogical composition of the individual matrix components (Molnár *et al.,* 1976; Molnár, 1991, 2015). In the member Cs-1, 58–67% of the matrix is a micrite, composed of anhedral calcite crystals (Molnár *et al.,* 1976; Molnár, 1991, 2015). The proportion of clastic particles (quartz, feldspar, clay) is relatively high (21–24%), while dolomite patches are subordinate, appearing in a size of <1 mm. In the member Cs-2 with a much more uniform texture than the member Cs-1, a proportion of the micritic matrix

is also higher (75–78%), dominantly composed of anhedral calcite crystals and subordinately euhedral dolomite. Clastics are present but in much lower content of 13–15% (Molnár *et al.,* 1976; Molnár, 1991, 2015). This is corroborated by our estimated proportions of RFCs in sample I using the CT data. The calcitic micrite is 27.18% (Fig. II-14) but our data are a sum of values for the entire Cs-1 and Cs-2 complex. Most likely, higher proportions of the matrix in our data must be representative of the (Cs-2) member sample I.

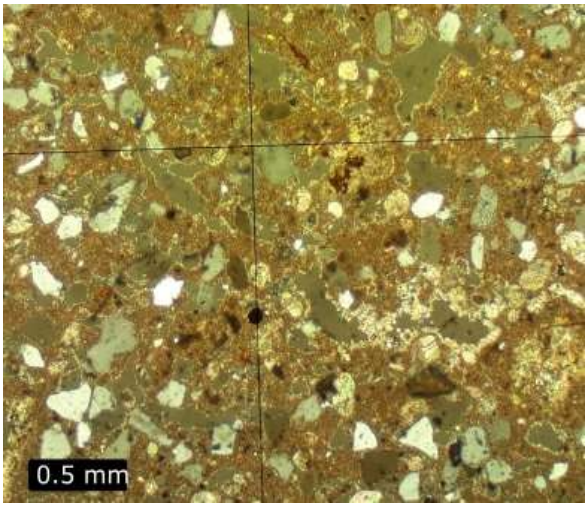

Figure II–13: The thin section from sample IV shows empty pores and filled/ partially filled pores, matrix. (30 x magnification, Xpl). mm: millimetres.

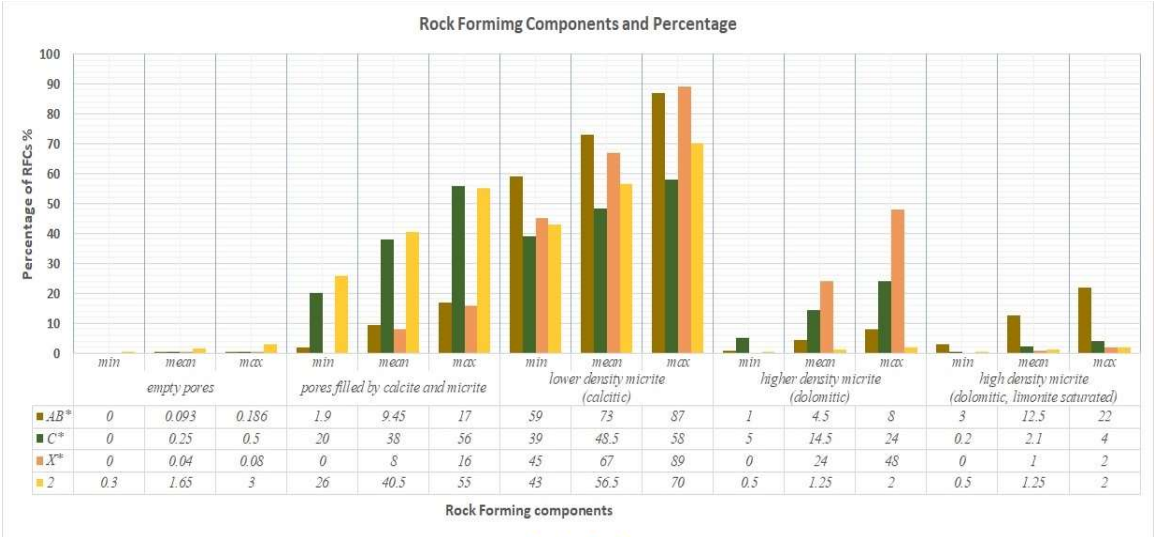

Figure II–14: Proportions of major RFCs determined by CT analysis.

In samples of the member Cs-3 ("pecsmeg" samples II and III) a proportion of the pores is much higher (9.28% in sample II and 13.88% in sample III, respectively) than in members Cs-1 and Cs-2 (Fig. II-14). It is interesting to note that sample II is more compact with a smaller number of pores compared to sample III. So, most of the pores are calcite sparite or micrite filled, which represent around 8.78% and 8.08% in samples II and III, respectively (Fig. II-14). The latter is developed by unconsolidated mud filling only partially the empty shells or pores. Gas pores are usually isometric in the unconsolidated saturated carbonate mud; however, they are distorted during desiccation and lithification (Choquette and Pray, 1970). Macropores are more abundant here than in the members Cs-1 and Cs-2. Macropores are the most diverse in this member as well (Figs. II-7, 8, 10). Desiccation cracks, sheet cracks, open and closed gas pores, root pores appear cutting through the laminae. The ratio of intergranular pores is negligible. So-called sheltered pores also turn up (Molnár *et al.,* 1976; Molnár, 1991, 2015). The limonite saturated matrix is up to 11.26% in sample III compared with 33.8% in sample II, which is higher than in sample I. The member Cs-3 ("pecsmeg" samples II and III) is a mud-supported wackestone with a highly complex texture recorded by thin-section analyses (Molnár *et al.,* 1976; Molnár, 1991, 2015). As reported by Molnár et al. (1976), the dominant component is a micrite (76–82%), the proportion of which is slightly higher than that of the member Cs-2. When compared with the underlying members (Cs-1, Cs-2), the member Cs-3 has ca. 10% lower CaCO3 content of 65.1–66.5% and ca 0.5–7% higher CaMg $(CO3)^2$ content of 26.5–32.1% (Molnár *et al.,* 1976; Molnár, 1991, 2015).

Based on our data, the proportion of the lower density calcitic micrite is 17.97 % in sample II and 22.62% in sample III (Fig. II-14). Higher density dolomitic micrite is present in higher amounts (39.43% in sample II and ~52.23% in sample III). The proportion of quartz and feldspars is the lowest in this part of the profile (9.0–9.5%) based on thin-section data (Molnár *et al.,* 1976; Molnár, 1991, 2015).

Sample IV (member Cs-4), based on the results of detailed XRD investigations (chalk) is dolomite. Based on thin-section data, a proportion of CaCO3 and $CaMg(CO3)_2$ is highly variable with values ranging between 36.1–65.6% of the former and 34.8–59% of the latter (Molnár *et al.,* 1976; Molnár, 1991, 2015). According to our results, the dominant matrix is a dolomitic micrite with ~58% while the calcitic micrite is ~26.1% in sample (Fig. II-14). As the

rock is described as a dolomite mud, our result confirmed a dominance of higher density mineral dolomite in the matrix.

In the member Cs-4, the micrite ratio is reduced to 49–60% compared to the members Cs-1, Cs-2 and Cs-3 (Fig. II-14). There is an increase in the proportion of quartz and feldspars to 16–23%. Lithic components are reduced in size (0.02–0.06 mm). The proportion of carbonate lithics also increases (6.5–8.5%). These clasts are intraclasts rather than exoclasts, having been ripped off the bottom of the lake by winds during a complete desiccation of the lakebed.

Pores filling sparite and microsparites are completely lacking here. The major pore types are desiccation, gas and root ones. Fossil Chara oogonia and gastropod shells also turn up here. which indicates that these samples could have the same precipitation environment, approximately similar in physiochemical or biological conditions. Based on our HU values (Fig. II-14), empty pores are ~2.34%. Pores filled or partially filled with Ca^{+2} are ~3.55%, while the higher density mud saturation limonite is up to ~10% in sample IV.

II.6. CONCLUDING REMARKS

Understanding and documenting the heterogeneity and textural properties of carbonates using the CT data are straightforward and more objective than thin-section analysis-based estimations. The quantitative information provided by thin sections is limited to the areas of the studied sample where subsamples were selectively taken for such investigations. In addition, estimations are rather subjective. Several different RFCs are present within a single grid cell, so correct filtering of the individual components and estimation of their proportions in the grid is not without bias. The CT analysis, however, provides us quantitative data in 3D at both the scale of the entire sample and a resolution defined by dimensions of the voxels at the micro-scale. The quantitative data expressed in the HU correlates with the density of the RFCs. Thus, its statistical properties also record information on their textural heterogeneity.

Previous studies of freshwater carbonates of the DTI in central Hungary have clearly defined the major textural components as calcite and dolomitic micrite, calcite sparite, carbonate clastics, quartz, feldspars, and limonite (Molnár, 1961, 1970, 1980, 1983, 1985, 1991, 1996; Mucsi, 1963; Molnár and Murvai, 1976; Molnár and Szónoky, 1976; Molnár *et al.,* 1995). All mentioned minerals are characterized by different densities (calcite 2.71 g/cm3, limestone 2.711 g/cm^3, dolomite 2.84 g/cm^3 and limonite 2.7–4.3 g/cm^3) which is also expressed in the

CT-based HU values. As the studied rocks represent a pool of the RFCs, in this pioneering work we adopted mixture analysis as a non-hierarchical clustering method for the segmentation of each RFCs using the CT data. We have found only two references that reported the CT-based density data for carbonates: limestone (2765 HU; Bolliger *et al.,* 2009), secondary formed marine dolomite in claystone of the Permian Boda Claystone Formation (3300–3600 HU; Abutaha *et al.,* 2021). These could have been used only as tentative guidelines in our work as the density values are highly dependent on the complexity of the studied rock sample, i.e., types, proportion, and collective presence of the RFCs. This complexity is also recorded in the overlap of distribution curves of each Meaningful sub-population determined by mixture analysis of the CT data in our work. So, setting up discrete boundaries for the RFCs is not easy and that is why the CT-based density data is reported as intervals in our work in addition to Mean and 2 STD.

Knowing the original volume of the studied and filtered subsamples, the percentage of each identified rock-forming component (e.g., calcitic matrix, filled pores, etc.) can also be estimated. The proportions of each rock-forming component calculated using the CT data can be compared to those defined by multiple thin section analyses on subsamples taken from selected parts of the studied sample. In light of our results providing a better estimate on the proportions of the RFCs for the entire volume of sample than thin sections, the nomenclature of the rocks must be reconsidered. XRD analysis provides us only semi-quantitative data on the presence and the proportion of rock-forming minerals. In the 1960s and 1970s, technical limitations in the XRD analysis hampered the estimation of the exact proportions of each identified mineral. In older studies as those of Molnár (1961, 1970, 1980, 1983, 1985, 1991, 1996) applying the XRD for the identification of rock-forming minerals in freshwater carbonate samples of the DTI, intensity of mineral peaks was considered for naming the studied rocks of each member of the Csólyospálos profile. According to our findings in samples where the proportion of the calcitic micrite is greater than that of the denser dolomitic, limonite saturated micrite samples can be determined as a dolomitic limestone. Contrary, where the densest components (dolomitic, limonite saturates micrite) are dominant, the name dolomite is adequate.

III. Palaeoenvironmental and palaeoclimatic inferences based on X-ray computer tomography: a case study of alkaline lake deposits in Hungary.

Nour Alzoubi, Sandor Gulyas, Janos Geiger*

University of Szeged, Department of Geology, 2-6 Egyetem u., H-6722,

Szeged, Hungary.

e-mails:

Nour Alzoubi*.

nouralzoubi@geo.u-szeged.hu,

Corresponding author

János Geiger

geostatisztika@gmail.com,

Sandor Gulyas

csigonc@gmail.com

Geologos

29, 1 (2023): 33–49

https://doi.org/10.14746/logos.2023.29.1.03

Palaeoenvironmental and palaeoclimatic inferences based on X-ray computer tomography: a case study of alkaline lake deposits in Hungary.

Nour N. Alzoubi [*] *, Sandor Gulyas, Janos Geiger*

Abstract

Widely distributed freshwater carbonate sediments, i.e., limestone, dolomitic limestone and dolomite, developed in interdune alkaline ponds of the Danube-Tisza Interfluve in the centre of the Carpathian Basin during the Holocene. The key parameters that determine the formation of any given type of carbonate mineral (calcite, dolomite) are temperature, evaporation rate, pH and ion concentrations, in addition to CO2 absorption by aquatic plants. CT analysis is capable of recording small-scale density variations attributable to compositional differences of sedimentary rocks. As the type and proportion of rock-forming minerals and other components is an artifact of past environmental and climatic conditions, CT values may act as potential palaeoenvironmental proxies. The present study compares variations in rock-forming components obtained for freshwater carbonates utilizing the CT method with already available geochemical and palaeoecological proxy data. Variations in molluscan ecology and isotope geochemistry, sedimentation times and CT- based rock density values all indicate the relevance of millennial-scale, climate-driven changes in carbonate formation. As previously observed, the emergence of colder conditions in the North Atlantic, which resulted in increased cyclonic activity and heavier rainfall in western Europe and the Danube watershed area between 10.3 and 9.3 kyr cal BP, resulted in the emergence of humid conditions favouring a rise in the groundwater table at our site and precipitation of calcite from pore waters as opposed to high-magnesium calcite. This is clearly reflected in a negative shift in CT density values in our dated rock samples.

III.1. Introduction

The area of the Danube-Tisza Interfluve (DTI), located in the heart of Hungary between the rivers Danube and Tisza, is covered by wind-blown sand and loess deposits. These sediments contain around 10 % carbonate; they were shaped into dunes in a NW–SE direction by dominant north-westerly winds during the late Pleistocene and early Holocene (Mihältz, 1947, 1953; Molnár, 1976, 1988; Kercsmár, 2015). The interdune areas are occupied by alkaline lakes over the entire interfluve area complemented by a few lakes that emerged because of antecedent river regulations in the 19th century. The main source of water is groundwater which contains calcium and magnesium as well as surface runoff (Molnár, 1976; Molnár & Szónoky, 1976; Molnár *et al.,* 1995).

High-magnesium calcite precipitates seasonally from the water based on climatic conditions and associated volume, geochemistry (pH, the concentration of dissolved elements) of the lake and pore waters, as well as fluctuations of the groundwater table. The DTI groundwater has a

fairly high total dissolved solid (TDS) content; 500-2000 mg/l on average; occasionally > 5,000 mg/l. Strong evaporation affects the water level of the lakes due to high summer temperatures and little rainfall. The TDS of lake water rises to values between 8,000 and 70,000 mg/l, as the lost water is replenished from the groundwater, making these ponds very saline and highly alkaline, with a pH ranging from 9 to 11, due to calcium, magnesium and hydro-carbonate ions (Molnár & Botz, 1996). Seasonally, towards the end of the summer, groundwater levels drop to 3-8 m below the surface, and many of the lakes dry up (Molnár & Szónoky, 1976; Molnár, 1991; Molnár *et al.,* 1995). The ratio of Mg/Ca in the lake and pore fluids determines the precipitation of primary carbonates (calcite, high-Mg calcite, aragonite, hydrous Mg carbonate) and secondary carbonates (proto-dolomite, dolomite, Huntite, magnesite). Secondary carbonates and high-Mg calcite are found in lakes when the stated ratio exceeds 7, the overall salinity of the water is high, and the salinity fluctuates greatly during the year. During periods when pore waters are exceptionally rich in Mg, proto-dolomite occurs in the mud accumulating on the lakebed through the transformation of Mg-bearing calcite (Müller *et al.,* 1972; Gaines, 1977; Müller & Wagner, 1978; Tullner & Cserny, 2003; Chen *et al.,* 2017; Fang & Xu, 2019).

Rainfall during the autumn supplies freshwater to the DTI alkaline lakes, thereby decreasing Na and K concentrations and increasing the Mg/Ca ratio to 7-12 creating favourable conditions for precipitation of high-magnesium calcite. The Mg/Ca ratio in the residual pore fluids rises even more, causing high-magnesium calcite to undergo early diagenetic transformation into proto-dolomite and dolomite since the CO_3/Ca ratio exceeds 1. Seasonal migration of pore water saturates the matrix and fills the pores with minerals precipitating from the residual solution (calcite, limonite), changing the carbonate mud into solid rock where the lacustrine phase of carbonate precipitation had ended (Bender *et al.,* 1975; Molnár, 1980, 1991).

Thus, two types of carbonate are present in the region: the lower part (60–110 cm) is solid carbonate rock (dolomitic limestone) corresponding to lacustrine deposits which have undergone diagenesis, and in the upper part (30–60 cm) there is unlithified recent carbonate mud (Miháltz & Faragó, 1946; Miháltz, 1947, 1953; Mucsi, 1963; Molnár, 1970; Jenei *et al.,* 2007; Sümegi *et al.,* 2015; Sümegi & Náfrádi, 2015). The composition of sedimentary rocks, i.e., the distribution of principal rock-forming components (RFCs), expresses their formation and diagenetic history. To assess the nature of these processes and the resulting spatial

heterogeneity, quantitative information on RFC distribution at both macro- and micro-scales is required (Alzoubi *et al.,* 2022).

X-ray computed tomography is a non-destructive inspection technology that produces cross-sectional tomographic images by measuring penetrating radiation intensity changes throughout various routes of a material. Such changes are linked to density variations attributable to differing chemical, physical or biological characteristics of the material under study (Maurício *et al.,* 2017). The original application of CT was for medical purposes (Kenter, 1989), but it is now frequently employed in other fields, including archaeology, palaeontology, sedimentology and structural geology (Duliu, 1999; Ketcham & Carlson, 2001; Földes *et al.,* 2004; Cnudde *et al.,* 2006; Markussen *et al.,* 2019). Post- or syndiagenetic sedimentary formations present in clastic rocks are also easily identified visually on CT images (Wilding *et al.,* 2005). However, CT techniques were applied to heterogeneous carbonate to show the potential and limitations of CT (Hicks *et al.,* 1994), and compare the standard mass balance equation and concentration with a CT (Fourar *et al.,* 2005). When compared to three-dimensional methods, two-dimensional digital image analysis (2D DIA) allows the processing of any core cutting and needs little data manipulation and computing (Oliveira *et al.,* 2020).

Apart from visual evaluation, the most essential characteristic of CT analysis are the data behind it, which contain quantitative information on density variations evident between rock-forming textural components in the material. Computer tomography analysis supplies us with quantitative data in 3D at both the scale of the entire sample and a resolution specified by voxel dimensions at micro-scale. The density of RFCs corresponds with quantitative data reported in Hounsfield units (HU) (Bhattacharyya, 2016). As a result, its statistical features capture information on their heterogeneity. In a previous study, Alzoubi et al. (2022) successfully applied such techniques to segment freshwater carbonate samples deriving from the site of Csólyospálos in the DTI into its rock-forming components (RFCs). In that work, the authors managed to estimate the proportions of the major rock-forming components, separating them into three major groups: matrix, pores and cement material. The former two carry information on the depositional history, while the last-named refers to rock diagenesis. The creation of carbonate cement infilling the pores is also a subsequent step of rock formation, thus again yielding information on the diagenetic history. The percentages of the RFCs for samples were presented as a whole and made comparisons possible with percentage distributions estimated

using thin sections. While the former was based on values inferred for the entire sample, the latter used thin sections taken only from selected parts of sample. The data available per CT slice (Alzoubi *et al.,* 2022) allows for the investigation of vertical and horizontal compositional changes at a much smaller scale, i.e., that of voxels. In this way minor scale changes, reflecting shifts in the depositional environment, can be tackled. Information on the textural characteristics, geochemical composition, isotope geochemistry and molluscan-based palaeoecology of carbonates from the Csólyospálos site are readily available, although at a much lower resolution (Mucsi, 1963; Molnár, 1970, 1980, 1991; Molnár & Szónoky, 1976; Molnár *et al.,* 1995). This allows us to make a visual comparison with our high-resolution compositional data deriving from CT analysis of samples. The present paper aims to test the applicability of CT-derived data for palaeoenvironmental reconstruction, as well as to capture and describe the vertical heterogeneity of RFCs in selected carbonate samples from the Csólyospálos site using the logic from the previous study by Alzoubi et al. (2022). This time estimations of RFCs are presented per CT slice allowing to tackle minor changes in environmental conditions. A comparison of small-scale trends (possibly centennial) with major trends (multimillennial-scale) seen in geochemical and palaeoecological records from the site enables us to refine the evolutionary history of the lacustrine sequence. In addition, periods dominated by different types of carbonate mineral precipitation may also be captured.

III.2. Study site

The Danube-Tisza Interfluve (DTI) is a 180-km-long and 120-km-wide, wind-blown sand and loess-covered ridge, 100–150 m a.s.l. between the rivers Danube and Tisza in central Hungary (Fig. III-1A). To the west, the region is bounded by the Danube River valley tectonic depression, which is located at a height of 90–100 m a.s.l. The area's eastern limit is formed by a 10–15 km-wide valley of the Tisza River 80 m a.s.l. The DTI's bedrock created of alternating loess and wind-blown sand strata that reflect reworked Danube River deposits. The sands were organised into a sequence of dunes with a NW to SE direction by prevailing winds throughout the late Pleistocene and Holocene. The interdune depressions are filled by a range of soda lakes, which obtain their water mostly from groundwater moving from the Danube valley to that of the Tisza River in the east. These lakes are characterised by freshwater carbonate formation (Fig.III-1D, F) (Molnár & Szónoky, 1976; Molnár *et al.,* 1976). Our study site at Csólyospálos, located on the south-eastern edge of the Danube-Tisza Interfluve (Fig.

III-1B), is one of these interdune lacustrine systems in which carbonate formation began around 11,500 years ago and ended around 3,500 years ago (Jenei *et al.,* 2007; Sümegi *et al.,* 2015; Sümegi & Náfrádi, 2015). The outcrop is located around 2 kilometres northeast of the settlement of Csólyospálos at an elevation of 92 m a.s.l. A geological section constructed in the centre of an upper Pleistocene interdune depression exposes a c. 1-m-thick carbonate succession covered by upper Holocene black earth soil. A Holocene dune borders the former pond in the southeast (Fig. III-1C). The carbonate series that covers the bedrock of upper Pleistocene wind-blown sand is divided into two parts: a lower lithified and a higher non-lithified. The series was subdivided into five members (Cs-1, Cs-2, Cs-3, Cs-4 and Cs-5) on the basis of its observed lithological properties (Molnár, 1970) (Fig. III-1E). Cs-5 corresponds to the modern soil and as such is beyond the scope of the present analysis.

III.3. Methodology

III.3.1. Sampling

Samples in the present study correspond to the ones collected and analysed by Mucsi (1963) and housed in the sedimentary rock collection of the Department of Geology and Palaeontology, University of Szeged. All samples were originally cut in half with their surfaces polished. CT measurements were done on four samples representing all members of the Csólyospálos carbonate sequence (Cs-1, Cs-2, Cs-3, and Cs-4). Members Cs-1 and Cs-2 are represented by a single sample (sample I) taken a depth of between 65 to 90 cm in the section. Member Cs-3 is represented by two adjacent samples (samples II and III) from a depth of 65-60 cm, while member Cs-4 is represented by a single sample (sample IV) from a depth of 55-25 cm (Fig. III-1E).

III.3.2. Computer tomography

CT scans were run for these four samples using a Siemens Emotion 6 medical scanner at the Department of Radiology, University of Pécs, Hungary. The CT scanner runs at 140 kVp, with a current of 189 mAs and a 1.5-second exposure duration. The slice thickness was 1.5 mm, and the lateral resolution 0.23 mm x 0.23 mm.

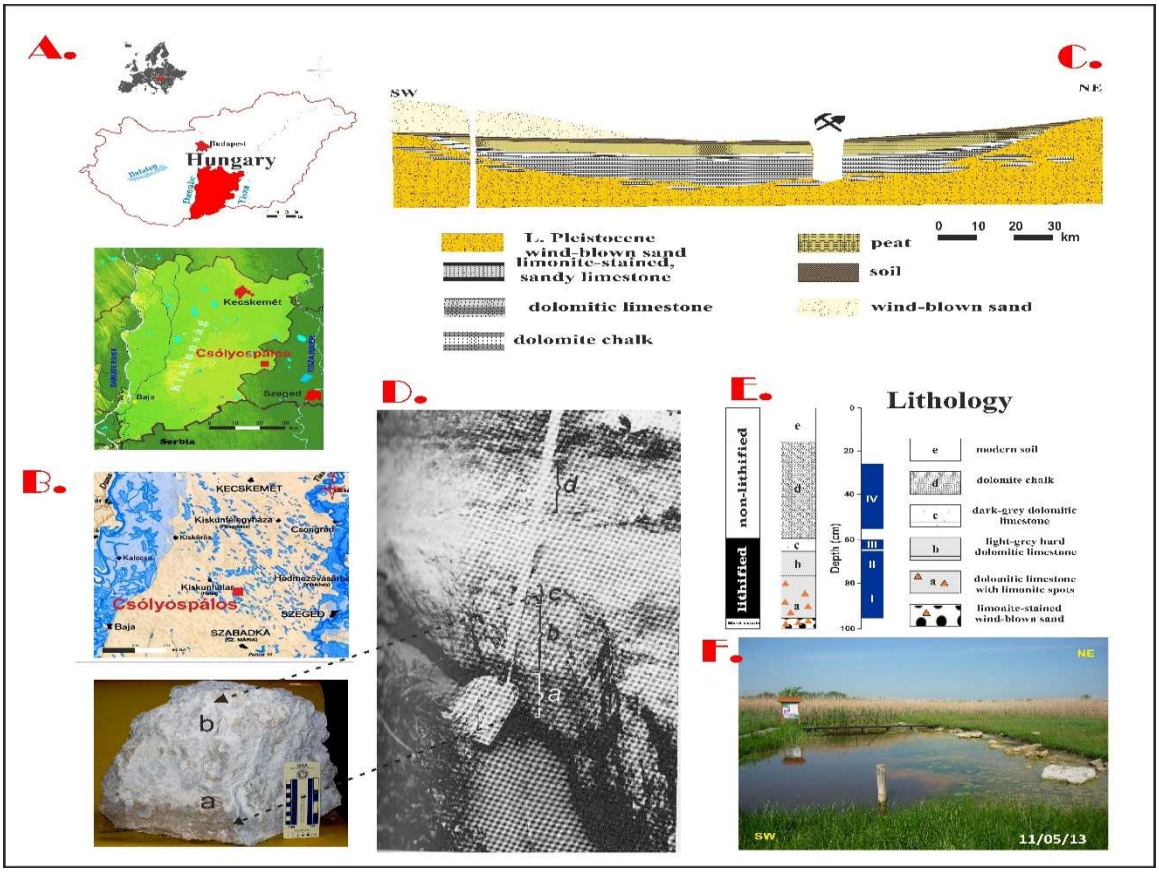

Figure III–1: Location and stratigraphy of the carbonate sequence studied near Csólyospálos. A – Location; B – Hydrography of the area, prior to the late 19th century; C – Geological cross-section of the site; D – Lithology of the site; E – Schematic log of the outcrop with position of samples under study marked; F – View of outcrop (adopted from Alzoubi)

III.3.3. Workflow of analysis

The major aim of our work was to reveal small-scale vertical proportional variations in rock-forming components (RFCs) that record sedimentary environmental changes and to find correspondences with palaeoclimatic and palaeohydrological changes inferred from results of geochemical studies by Molnár & Botz (1996) and palaeoecological investigations done by Mucsi (1963). X-ray computer tomography was done to gain quantitative data based on density differences of RFCs expressed by Hounsfield unit values (HU) (Fig. III-2). The CT images were exported as Digital Imaging and Communications in Medicine DICOM image and a 3D volume rendering software (Voxler 4.0) was used for visualisation, filtering, and data extraction. As scanning artifacts, such as beam hardening, can cause the CT value of a single material to change in different parts of an image, the dataset was filtered by removing the outer part of the image creating a centrally positioned CT brick (subset) smaller in volume than the

original sample. Data extracted from this CT brick were used in further statistical analysis. Distribution types were visually assessed using histograms and boxplots. As our samples are assumed to represent a pool of normally distributed populations corresponding to the rock-forming components, the maximum-likelihood method of mixture analysis was adopted to recover and estimate the parameters of two or more univariate normal distributions (Mean, STD) in PAST 4.06. This method is based on (EM) algorithm of Dempster et al. (1977). To determine if the number of groups chosen is appropriate and to avoid overfitting, the Akaike Information Criterion AIC (Akaike, 1974; Hammer *et al.,* 2001) is calculated. Each data point was assigned to one of groups using a maximum likelihood approach. The statistical parameters gained for each subpopulation were used to set HU value intervals. Using the gained parameters of the Mean ± 1 and 2 STD, the recovered subpopulations were visualised, and their lithological Meaning assessed. HU intervals set for each Meaningful subpopulation using the referred statistical parameters can be regarded to describe rock-forming components present in samples quantitatively.

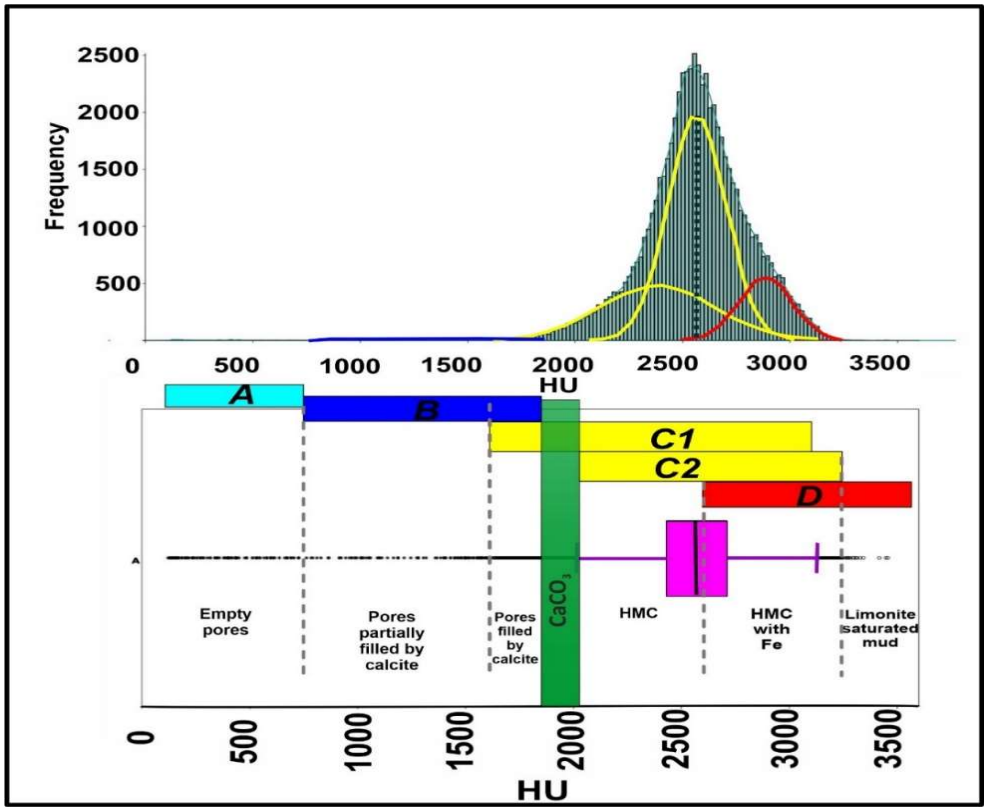

Figure III–2: Results of mixture analysis for sample I with explanation of subcomponents based on HU and RFCs (adopted from Alzoubi et al., 2022). Abbreviations: Ca – calcium, HMC – high magnesium calcite, Fe – iron.

Alzoubi et al. (2022) presented the results of RFCs defined via detailed statistical analysis of CT-scanned samples. Thus, here we just wish to show the main logic of the work by example of sample I. Five main components (A to D), presented in Figure III-2, display the results of the mixture analysis of sample I (Cs-1 and Cs-2). These represent the empty pores (A), partially or almost filled pores (B), the dominantly calcitic limestone (C1), the high magnesium calcite (HMC) bearing matrix (C2) and limonite saturated HMC and dolomitic matrix (D). As there is an overlap between these five major components a total of eight sub-components is notable: 1. empty pores, 2. partially filled pores (pores with less than 20 % infill), 3. semi-filled pores (pores of ~50 % filled), 4. filled pores by around (80-100 % filled), 5. calcitic matrix, 6. high-magnesium calcitic (HMC)-dolomitic matrix, 7. high-magnesium calcitic (HMC)-dolomitic matrix with a minor amount of Fe^{2+} and Mn^{2+} precipitate, and 8. limonite-saturated HMC-dolomitic matrix.

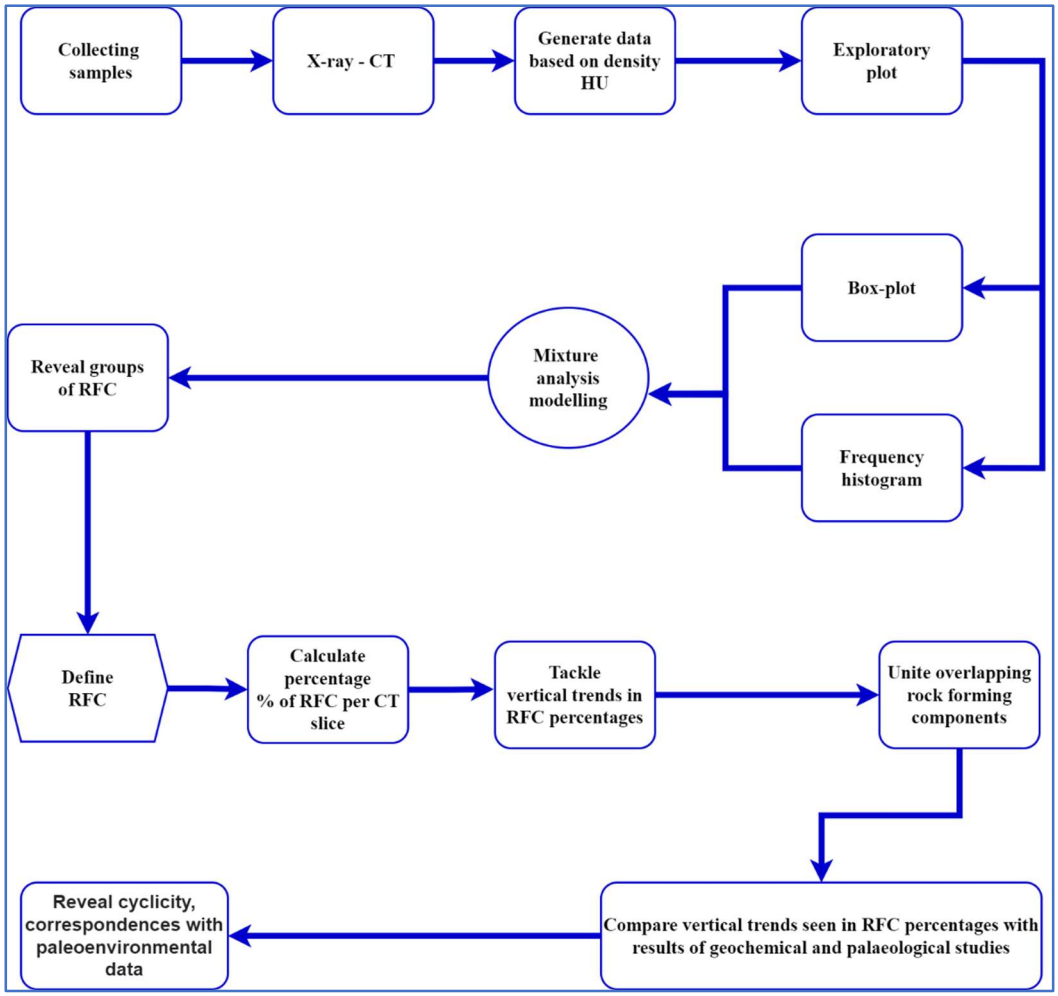

Figure III–3: The workflow applied in the present study.

In the present work, HU intervals of the five major RFCs were used, and percentages of RFCs were calculated for each CT slice sequentially using a script in Golden Software Scripter. Major and small-scale vertical trend changes in RFC percentages of our samples were compared with geochemical data of Molnár & Botz (1996) and palaeoecological data of Mucsi (1963), supplying information on palaeohydrological and palaeoclimatological changes (Fig. III-3).

III.3.4. Age depth modelling and sedimentation time

Radiocarbon data presented by Jenei et al. (2007), Sümegi et al. (2015) and Sümegi & Náfrádi (2015) were used to construct age-depth models. Bayesian modelling was performed using the software package RBacon (Blaauw *et al.,* 2018). All input data were provided as ^{14}C yr BP and the model used the Northern Hemisphere IntCal20 calibration curve (Reimer *et al.,* 2020) to convert conventional radiocarbon ages to calendar ages expressed as cal BP. Age modelling was run to achieve a 5-cm final resolution. All data and figures are presented in calendar ages expressed as cal BP. Sedimentation times (years/cm) were estimated by Markov chain Monte Carlo (MCMC) iterations using the accrate.depth.ghost and accrate.age.ghost functions of RBacon. This function allows us to capture variability in accumulation rates and assigned varying uncertainties with depth in contrast to the traditionally applied equation based on Mean model ages of consecutive depths and depth intervals.

III.4. Result and Interpretation

III.4.1. Members Cs-1 and Cs-2

The graphs in Figure III-4 depict the vertical variation of identified RFCs for sample I (Cs-1 and Cs-2). The vertical proportion of group A corresponding to empty pores is relatively constant with values ranging mostly between 0 and 0.05 % with some minor peaks of 0.15 and 0.2 %. These deviations can be attributed to the presence of large pores in the slices also seen in Fig.III-5. In group B, corresponding to the partially calcite-filled pores, there is a gradual decrease from 1.6 to 0.4 % between *c*. 90 and 82 cm, followed by a pronounced increase to plateau values between 0.8 and 1.2 % in general with some minor peaks of 1.6 %. This plateau corresponds to the middle part of sample after which another significant drop to 0.6-0.4 % is noted in the topmost part.

The percentage of the dominantly calcitic matrix (C1) is low in the bottom and top part of sample with values around 40-45 %. Higher values of 65-75 % form a plateau in the middle part of sample (between *c*. 82 and 68 cm). C1 and C2 show complementary trends along sample. The proportion of C2 in sample is high at the bottom (*c*. 50-55 % between 90-83 cm) and at the top (*c*. 43-55 % between 68-65 cm). The ratio of C2 ranges between 15-20 % in the middle where there is a notable rise in C1. This implies that the dominant form of carbonate mineral was calcite in the middle part and dolomitic matrix in the upper and lower parts. C1 and C2 reveal complementary trends along sample. The percentage of the predominantly calcitic matrix (C1) is low in those parts where the proportion of calcite-filled pores (B) is minimal, i.e., the bottom and top part of sample with values around 40-45%. Likewise, higher values of 65-75 % form a plateau in the middle part of sample (between *c*. 82 and 68 cm). This implies that calcite precipitation was relatively low in the lower and upper parts of sample. Conversely, the dominant form of carbonate mineral was calcite in the middle part. This is further corroborated by the contrasting trends of C2 corresponding to the predominantly dolomitic matrix. The proportion of C2 in sample is high at the bottom (*c*. 50-55 % between 90-83 cm) and at the top of sample (*c*. 43-55 % between 68-65 cm). Conversely, the ratio of C2 ranges between 15-20 % in the middle where there is a notable rise in C1. Conditions thus may have favoured. The formation of high-magnesium calcite and dolomite in periods when the lowermost and uppermost part of sample were laid down. Conversely, the precipitation of calcite must have prevailed in the period represented by the middle part of sample.

The proportion of the densest component (D) corresponding to the limonite-saturated matrix is the highest in the bottom 10 cm or so of sample (5-10 %) showing a steady drop to near zero values in the upper 15 cm. The proportion of Fe and Mn is likewise high in this part (Fig. III-8). This apparently Means that this part was significantly influenced by large-scale fluctuations of the groundwater table in relatively drier periods. Probably bacterial activity in the lake can affect Fe and Mn, but the primary source is dissolution from bedrock loess by oxidisation of groundwater.

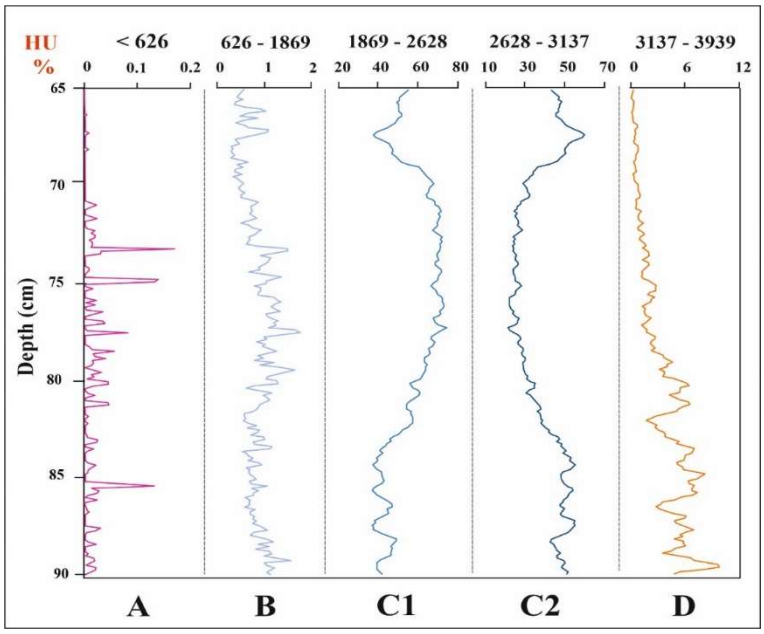

Figure III–5: Vertical changes in the proportion of identified rock-forming components (RFC) for members Cs-1 and Cs-2. A - empty pores, B - partially filled pores, C1 – low-density, predominantly calcitic matrix, C2 – high-density, predominantly dolomitic matrix, D – highest-density, limonite-saturated dolomitic matrix. Note numbers at the top mark the HU intervals of the corresponding RFCs.

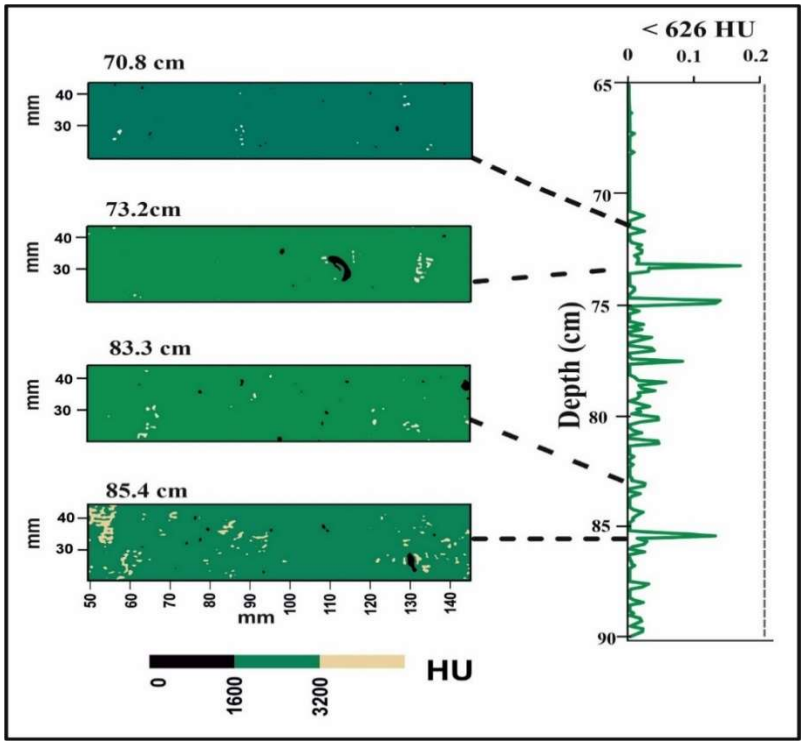

Figure III–4: Selected horizontal slices of sample I display the presence of large empty pores (dark areas) at depths corresponding to peak values of group A (< 626 HU).

III.4.1. Member Cs-3

Two adjacent samples (II, III) were taken from Member Cs-3; sample II is here considered to be representative of this member. The graphs (Fig. III-6) depict the vertical variation of identified RFCs for sample II (Member Cs-3) between depths of 65–60 cm. While empty pores appear to be missing in the lowermost two centimetres or so of sample there is a gradual increase in the topmost 2 centimetres, reaching a maximum value of 8 % at the top.

These values are significantly higher than in the case of sample I, where the proportion of empty pores was below 1.6-2 %. A similar trend is notable in percentage changes of group B corresponding to partially calcite-filled pores. Again, the proportions are significantly higher than in sample I, reaching values between 35-45 % in the topmost two centimetres or so and close to 15-20 % at the bottom. An opposing trend is notable in the proportions of C2 and D, representing high-density, predominantly dolomitic and highest density limonite saturated matrix. Here the largest proportions are confined to the lowermost three centimetres or so of sample with values between 34-56 % for group C2 and 1-4 % for group D. The percentage of lower density calcitic matrix (C1) is significantly lower than that of the higher density matrix components (C2, D), with peak values of 27 and 25 % in the lowermost and highest centimetre or so of sample. It stays relatively constant for most of sample. According to these observations, conditions favoured the formation of higher-density carbonates with a

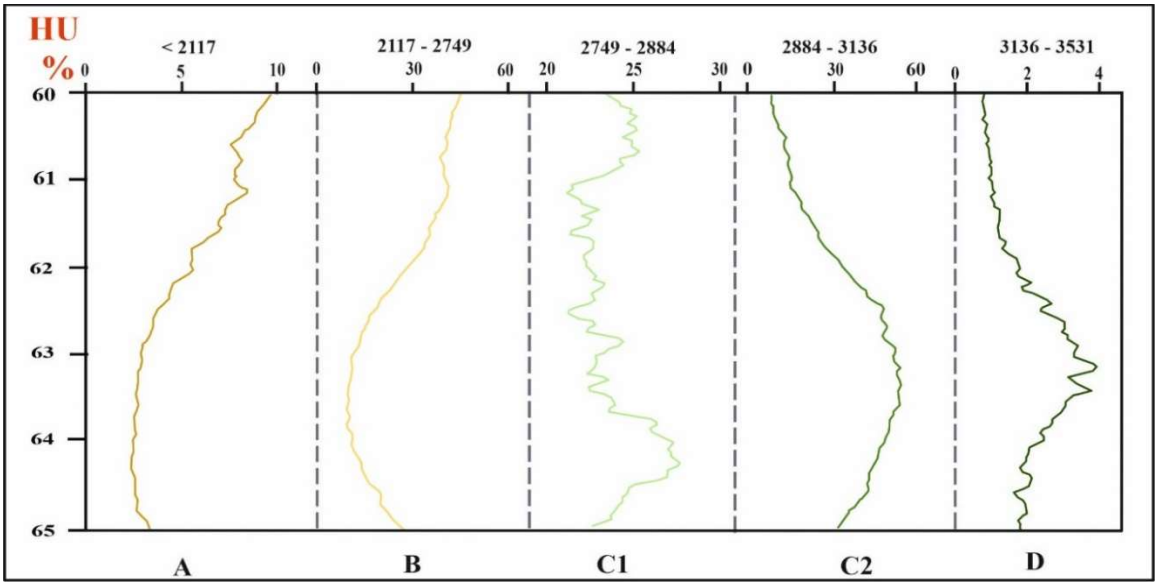

Figure III–6: Vertical changes in the proportion of identified rock-forming components (RFC) for member Cs-3. A - empty pores, B - partially filled pores, C1 – low-density, predominantly calcitic matrix, C2 – high-density, predominantly dolomitic matrix, D – highest-density, limonite-saturated dolomitic matrix. Note numbers at the top mark the HU intervals of the corresponding RFCs.

predominantly dolomitic matrix for the period captured by most of sample (3.5 cm out of 5 cm interval). A notable decrease in these high-density components, with a parallel increase in the lower-density matrix as well as empty pores and calcite-filled pores, is restricted to the uppermost centimetre or so, marking the emergence of highly different conditions.

III.4.2. Member Cs-4

Contrary to the previous sample, the carbonate of sample IV is non-lithified, although it has a similar length of *c*. 30 cm to sample I (Fig. III-7). The proportion of empty pores (A) is minimal (0-1 %) in the lowermost and topmost 5 cm of sample (Fig. III-7). Values are generally low between 50 and 30 cm close to 1% with several random peaks turning up at depths of 48.2, 44.5, 41.2 and 35.6 cm. However, in contrast to sample I where these peaks are sharp, here there is a gradual increase followed by a slow decrease around the mentioned peaks, which hints at the presence of not only a large number of pores but most likely a predominance of larger pores as well. In contrast to the vertical trend characterising group A, proportion of partially filled pores remains much lower and relatively constant (1-1.5 %). The proportion of

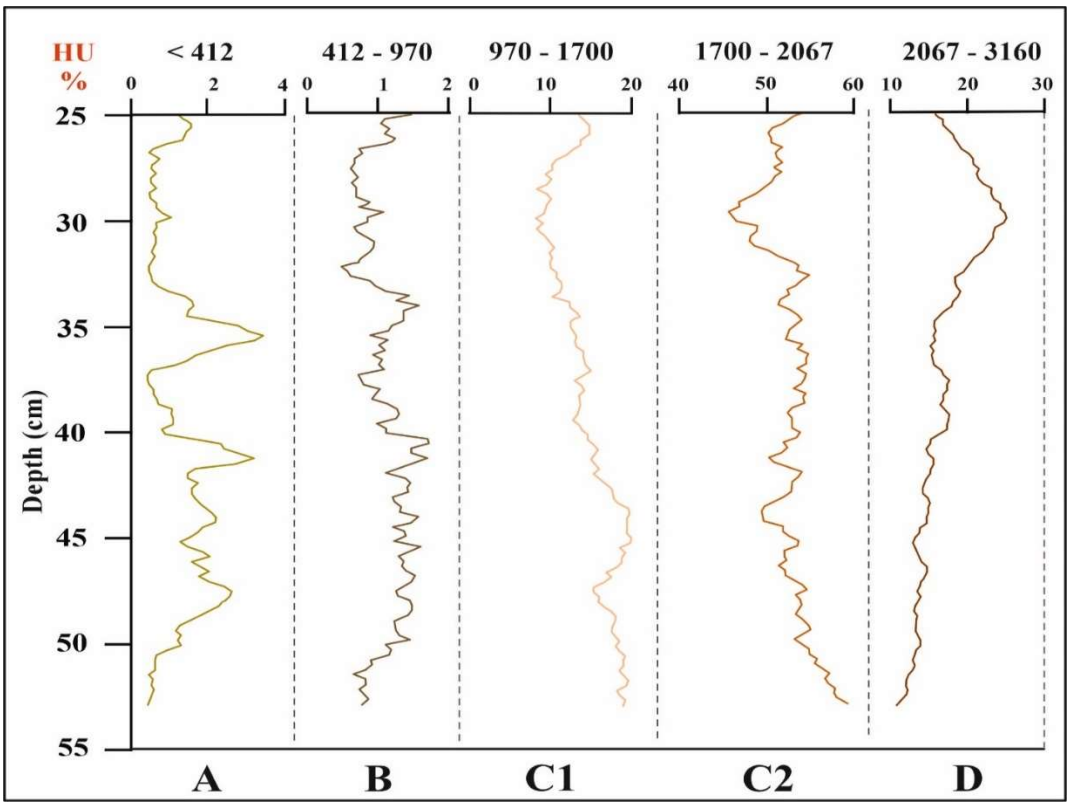

Figure III–7: Vertical changes in the proportion of identified rock-forming components (RFC) for member Cs-4. A - empty pores, B - partially filled pores, C1 – low-density, predominantly calcitic matrix, C2 – high-density, predominantly dolomitic matrix, D – highest-density, limonite-saturated dolomitic matrix. Note numbers at the top mark the HU intervals of the corresponding RFCs.

the lower-density calcite-bearing matrix remains low throughout sample (10-16 %) and has a similar upward-decreasing trend. The highest proportions are notable for the higher density, predominantly dolomitic matrix component (C2) (54-66 %). It is relatively constant for most of sample (around 60 % between depths of 50-33 and 26-28 cm, respectively), implying the prevalence of similar environmental conditions for a major part of sample. Percentages of the highest density RFC (D) remain low (16-20 %) for most of sample with a gradual, slow upward increase reaching peak values of 24-28 % in the topmost ten centimetres or so.

III.5. Comparison with previously generated geochemical and palaeoecological data

As can be seen in Figure III-8, at depths between 90 and 85 cm, the carbonate content is the lowest (< 10 %), while the proportion of dolomite in carbonate minerals is relatively high (*c*. 30-50 %). This is where the highest Mean HU values are recorded, and the proportion of high-density RFCs (C2, D) is also high (Fig. III-4). Ca has its all-time low as well as Sr, along with positive $d^{18}O$ (-4‰) and $d^{13}C$ (1‰) values. This implies the emergence of warmer, drier conditions with higher evaporation rates and restricted plant assimilation of CO_2, favouring the precipitation of high-magnesium calcite and dolomite (McConnaughey, 1991). The proportion of Fe is the highest in this part, indicating that the main controlling factor here is ground water table fluctuation and subsequent fluctuations in pH (compare Molnár & Botz, 1996). The trend in Mn and Fe follows that of HMC (C2, D) in the lowermost part of Sample I (Figs III-4, III-8).

In this interval, as shown in Figure III-11, aquatic gastropods that tolerate a temporary water cover (e.g., *Anisus spirorbis* (Linnaeus, 1758)) are dominant, and the proportion of terrestrial, nearshore taxa (e.g., *Succinea oblonga (*Draparnaud, 1801)) is low, hinting at a relatively restricted shoreline and/or a smaller extension of the former water body. In the next interval, between 85 and 75 cm, there is a marked decrease in the percentage of dolomite minerals to about half of the original value (25-27 %) accompanied by a *c*. 30 % rise in carbonate and *c*. 15 % increase in Ca content (Fig. III-8). The percentage of Fe also

decreases, while the concentration of Mn significantly increases. This interval is also characterised by a negative shift in $d^{18}O$ and $d^{13}C$ values (to -8‰). Mean HU values also undergo a significant decrease to 2,500 from their original value of 2,700, marking the precipitation of lower-density minerals and lower input of higher-density minerals. The proportion of calcite-filled pores also reaches a peak value (Fig. III–4). The negative shift in oxygen isotopes marks the emergence of a slightly cooler and more humid period. The likewise negative shift in carbon isotope values hints at greater extraction of CO_2 by algae responsible for the precipitation of carbonate, while high Mn values indicate higher bioproduction rates in the lake as algae accumulate higher proportions of Mn (Richardson *et al.,* 1988; Vanderputten *et al.,* 2000; Lazareth *et al.,* 2003) in their bodies and this is released into the water after their death. The recurring occurrence of larger empty and calcite-filled pores (Fig. III-4) hints at the expansion of the deep-rooted aquatic vegetation. As seen in Figure III-11 the proportion of near-bank gastropods and those tolerating temporary water cover (*Anisus spirorbis* (Linnaeus, 1758)) decrease, while there is a marked increase in percentages of constant water taxa (e.g., *Pisidium obtusale* (Lamarck, 1818)) marking an expansion of the lake's surface and a deepening of the water under more humid conditions. Higher temperatures result in higher evaporation rates, higher salinity and pH which acts as a limiting factor in algal growth and primary production (Tompa *et al.,* 2014; Molnár *et al.,* 2019). Thus, a reduction in temperatures and increase in humidity favour the increase in algae in the pond by reducing the pH, lowering the concentration of Na, K ions and allowing calcite to precipitate, a process called whitening and yielding murky, milk-like waters (Thompson *et al.,* 1997; Tompa *et al.,* 2014; Molnár *et al.,* 2019; Pósfai, 2020).

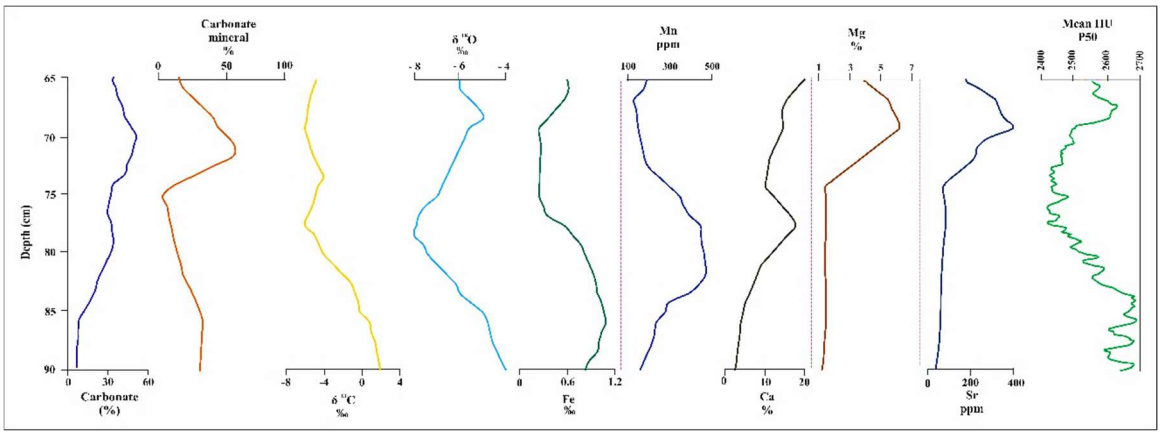

Figure III–8: Geochemical data adapted from Molnár & Botz (1996) for members Cs1 and Cs2 and Mean HU values.

In the last interval, between 75 and 60 cm, there is another increase in the percentage of dolomite minerals (to 65 and 85 %) accompanied by an increase in carbonate content (Fig. III -8). $d^{18}O$ undergoes a positive shift (to -6‰) along with a marked increase in Sr, pointing to the emergence of more arid conditions with higher temperatures in comparison with the previous interval. Mean HU values also increase to 2,650 HU, marking the precipitation of higher-density RFCs. The highest density D component remains low (Fig.III-4) just like concentrations of Fe and Mn. Thus, the appearance of a higher-density matrix is here attributable to the precipitation of high-magnesium calcite and dolomite rather than saturation by metallic components. An all-time high Mg value, as well as the high percentage of dolomite minerals (65-85%), also corroborate this assumption (Fig. III-8).

All in all, we can see the initial development of more arid conditions with a highly limited water coverage and significant water table and groundwater fluctuations favouring the formation of dolomitic limestone. Subsequently, cooler, and more humid conditions emerge, resulting in a deepening of the lake as well as its spatial expansion along with an increase in aquatic and near-shore vegetation. In this interval, the extraction of CO_2 from the water by algae must have been the dominant control of carbonate precipitation, similar to what was seen in the interval between 85 and 75 cm (Tompa *et al.,* 2014; Molnár *et al.,* 2019).

In the final phase, captured by a sample I, drier conditions emerge again favouring the precipitation of high-magnesium calcite and the formation of dolomitic limestone. In sample II (Cs-3) Fig. III–9, which represents the next interval in the lake's evolution, the same trend continues at the top of sample I (Figs III-6, III-8). $d^{18}O$ values remain constant and the same

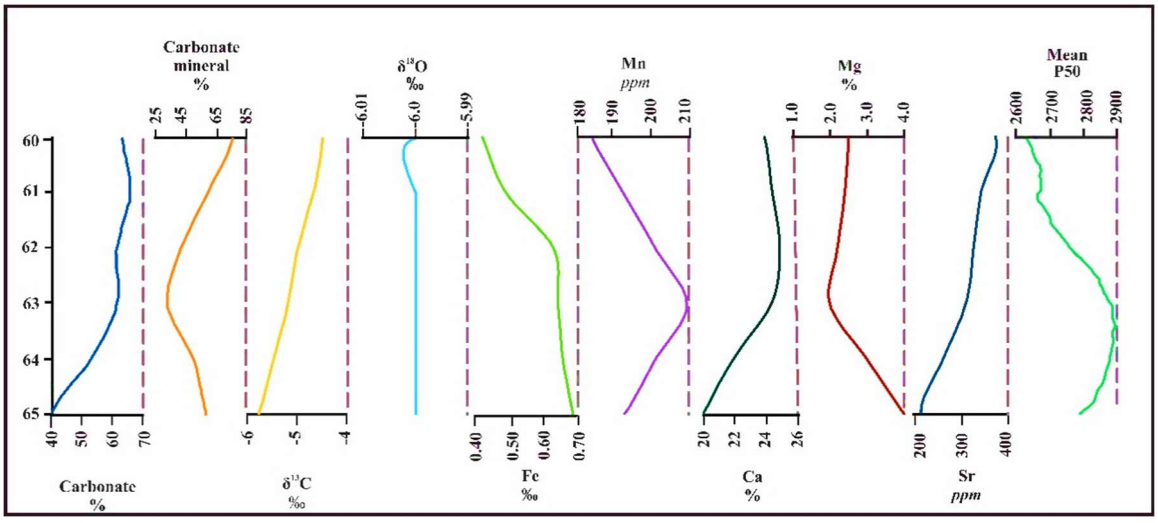

Figure III–9: Geochemical data adapted from Molnár & Botz (1996) for member Cs3 and Mean HU values

as in the top part of sample I (-6‰), Sr values also remain high, showing a gradual upward increase (220 to 380 ppm). All these again point to the prevalence of drier and warmer conditions favouring the precipitation of high-magnesium calcite and the formation of dolomite. The Mean HU values remain above 2,600 similar to the lowermost and topmost part of sample I. In the lowermost 3 cm of sample II, this reaches even 2,900 HU, hallmarking the predominance of higher-density minerals in the carbonate (Fig. III-9). The proportions of dolomite minerals remain close to 50 %, marking relatively stable conditions. The carbonate content also remains stable after an initial rise to 60 %. In this part the percentage of terrestrial gastropod taxa that prefer humid habitats (*Punctum pygmea (*Draparnaud, 1801)) further increases with a continuing decrease of constant water taxa (*Pisidium obtusale* (Lamarck, 1818)), marking a drop in the water level and a reduction in the pond surface (Fig. III-11).

In the topmost sample IV, all geochemical parameters remain relatively constant, with the exception of the interval between 48 and 38 cm (Fig. III-10). d^{18}O values remain around -6‰, the same as in the previous sample, apart from a negative shift to -7‰ in the 10-cm-interval mentioned. Sr also remains high (around and above 300 ppm) with Fe, Mg, and Ca as well as the carbonate and dolomite mineral content. Here the percentage of aquatic taxa (*Pisidium obtusale* (Lamarck, 1818)) significantly decreases, reaching their minimum in the section studied (Fig. III-11). Among aquatic taxa those tolerating temporary water (*Anisus spirorbis* (Linnaeus, 1758)) prevail. Percentages of near-bank and dry habitats preferring taxa (*Chondrula tridens* (Müller, 1774)) increased significantly, marking the expansion of

terrestrial habitats, a significant reduction in the lake surface and a major drop in the water level. After the initial drop Mean HU values remain constant. Comparison of absolute values with those of previous samples is not possible as here the lower values hint at the lack of

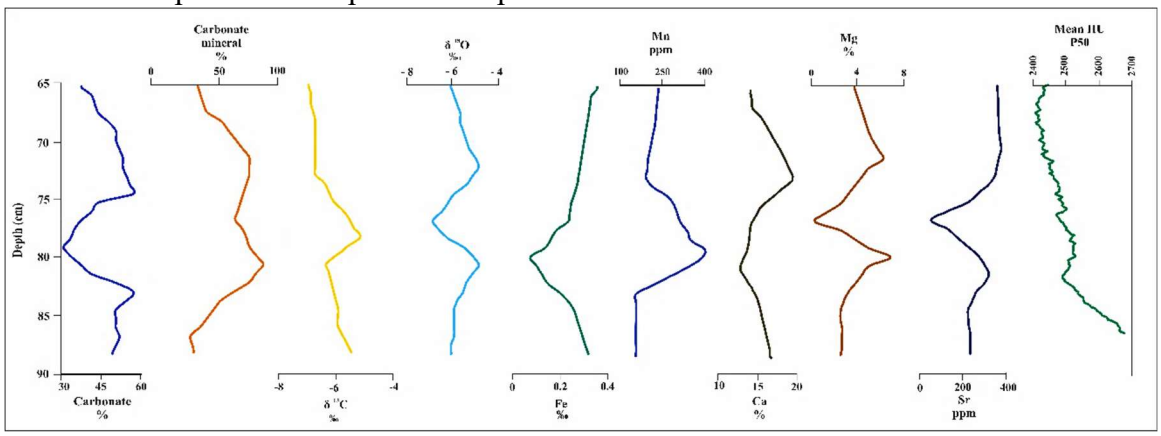

Figure III–10: Geochemical data adapted from Molnár & Botz (1996) for member Cs4 and Mean HU

cementation. So again, dry conditions favoured the precipitation of high-magnesium calcite and dolomite in this part. In the mentioned 10-cm-interval between 48 and 38 cm, where a short period of cooler and more humid conditions can be presumed, a slight increase in the percentages of C1 (low-density, predominantly calcitic matrix) is also notable parallel with a slight decrease in the proportion of the higher-density C2 component (Fig. III-7).

III.6. Comparison with extra-regional palaeohydrological and palaeoclimatological proxies from the North Atlantic and west-central Europe

Based on the developed age depth model, the first two studied samples span the interval between 10.8 and 8.8 kyr Cal BP (Fig. III-12). Sedimentation times varied between 33 and 80 years/cm. At the base of the section, corresponding to the interval between 10.8 and 10.4 kyr, sedimentation times were low (60-65 years/cm). This period is characterised by relatively higher Mean HU values (2,600-2,700 HU). Here both the $\delta^{13}C$ and $\delta^{18}O$ values are positive (-1 to 0 ‰ and -4.8 to -4‰, respectively), and the estimated dolomite mineral content is also high (~ 50 %). The proportion of intermittent water-cover-tolerant gastropods (e.g., *Anisus spirorbis* (Linnaeus, 1758)) is likewise high (40-25 %), while that of constant water-preferring taxa is low at 15-20 % (*Pisidium obtusale* (Lamarck, 1818). The amount of non-arboreal pollen grains (NAP) is also relatively high (Fig. III-12). All this confirms our view of relatively warmer conditions and a greater aridity at the site. In the following period, *c*. 1 kyr to 9.4 kyr

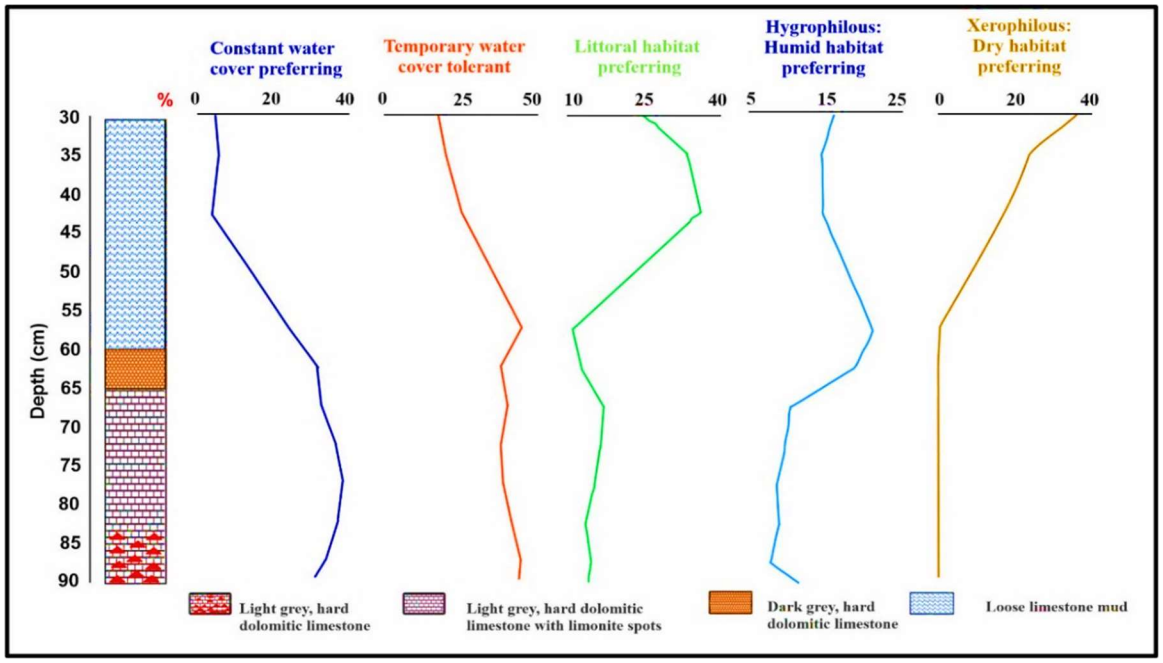

Figure III–11: : Palaeoecological data for the entire section, adapted from Mucsi (1963).

Cal BP sedimentation times decreased to 30-35 years/cm, marking an increase in carbonate formation. This period is characterised by a strong negative shift in the $\delta^{13}C$ and $\delta^{18}O$ values (ca. -7 and -3‰), hallmarking the emergence of cooler and more humid conditions and greater primary production. A similar negative shift is notable in the Mean HU values, indicating the precipitation of dominantly calcite. A marked decrease in the number of non- arboreal pollen NAP grains (Gramineae) also signals a reduction of open steppe areas around the lake. The water level probably rose. This is seen also in the marked decrease in intermittent water-cover-tolerant aquatic gastropods (*Anisus spirorbis* (Linnaeus, 1758)) and a major increase in the constant water-cover-preferring elements (*Pisidium obtusale* (Lamarck, 1818)). Aquatic gastropods that prefer milder conditions also significantly decrease, parallel to an increase in the proportion of cold-loving elements signalling the emergence of cooler conditions. This period is bounded by two major important climate change events: an expansion of colder conditions in the Alps (Magny *et al.,* 2003, 2006) and a southward displacement of ice-rafted debris and cooler ocean water in the North Atlantic, referred to as Bond event 7 at 10.3 kyr cal BP and Bond event 6 at 9.4 kyr cal BP (Bond *et al.,* 1997, 2001). As a probable result, significant cooling and increase in precipitation are notable in western Europe also seen in the high lake water levels of the Swiss Alps (Magny *et al.,* 2003, 2006).

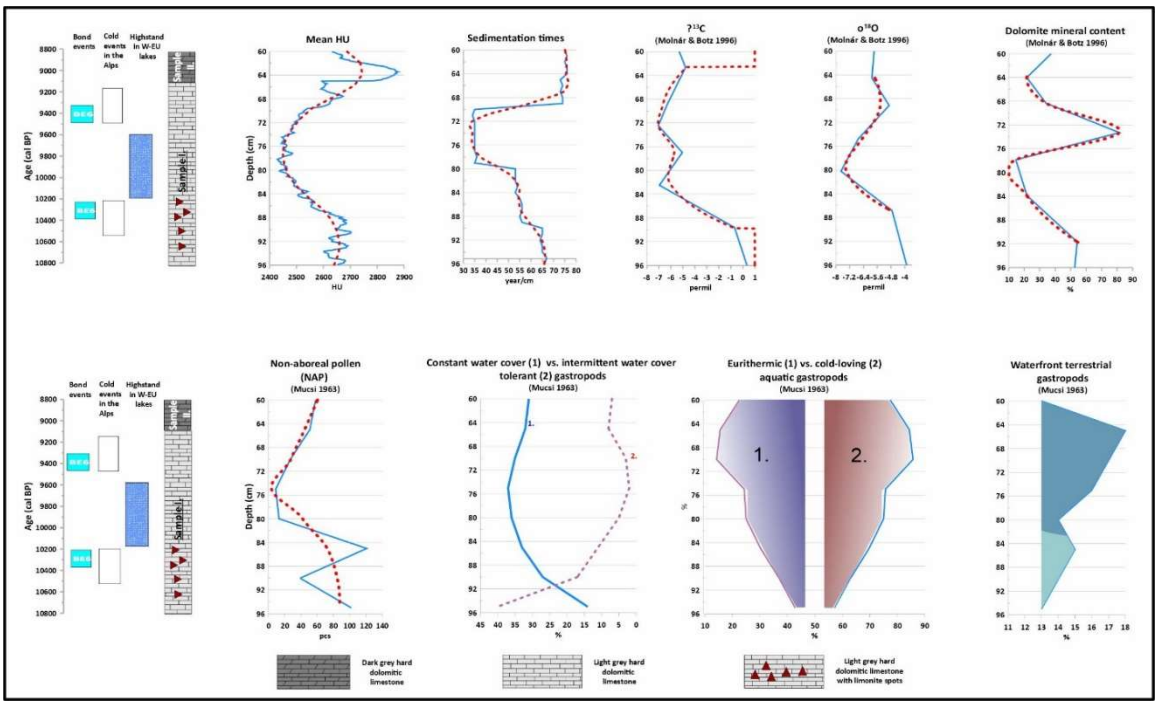

Figure III–12: Temporal changes in Mean HU values, sedimentation times and geochemical (Molnár & Botz, 1996), palaeoecological (Mucsi, 1963) parameters between 10.8 and 8.8 kyr cal BP in light of palaeoclimatic and palaeohydrological data for the North Atlantic, Alps and western Europe (Bond et al., 1997, 2001; Magny et al., 2003, 2006).

This could have resulted in higher flood waters on the catchment of the Danube River, yielding a higher input of freshwater to the ponds of the Danube-Tisza Interfluve through rainfall and higher groundwater tables. A reduction in temperatures also led to reduced aridity and expansion of arboreal vegetation (bushes). In the last 600 years, after *c*. 9400, conditions slowly improved leading to slightly warmer temperatures; a reduction in the water table was also seen in the expansion of waterfront terrestrial gastropod taxa (*Chondrula tridens* (Müller, 1774)) and a positive shift in all isotope and Mean HU values, again hinting at the prevalence of high-magnesium calcite and dolomite precipitation.

III.7. Concluding remarks

Sedimentary rocks are the best archives to record past palaeoenvironmental and palaeoclimatological changes. Comparison of high-resolution biotic and abiotic proxy records enables us to reconstruct these changes at the millennial and even centennial scale, depending on the resolution attainable via sampling. Rock-forming components record information on the environmental conditions in which they are formed. In lacustrine freshwater carbonates the matrix, composed of autochthonous carbonate minerals precipitated from the water, plus additional allochthonous components (quartz, feldspars, clay minerals), yields information on sediment formation which reflects properties and changes in the sedimentary environment. To assess these changes quantitative information on the composition and proportion of rock forming components (RFCs) at high resolution is needed. The CT is sensitive to changes in density; therefore, changes in any biogeochemical parameters in the environment show changes in CT Mean values. X-ray computer tomography has helped us gain quantitative data based on density differences of RFCs expressed by the Hounsfield unit values. In the present study, we have tested the applicability of the method to reveal small-scale (mm) vertical proportional variations in RFCs recording temporal sedimentary environmental changes and find correspondence with palaeoclimatic and palaeohydrological changes inferred from results of geochemical and palaeoecological investigations. Due to their lower resolution of mm-scale compared to that of micro-CT offering resolutions at the nanometre scale, data and images from medical CT are unable to tell apart micrite and sparite in carbonates, whose size is below the voxel size. Based on density differences the relative components of the matrix (autochthonous calcite and dolomite as well as allochthonous quartz, feldspar, clay, pellets) as a whole, the cement and pores can safely be decomposed from medical CT data. Micritic and

sparitic components, as well as single particle grains, are recorded only on micro-CTs that offer higher resolution. This may be a limiting factor in the application of medical CT. However, upscaling of data from the level of micro-CT to that of medical CT is still not solved in earth sciences. Nevertheless, general density changes in the matrix captured via medical CT carries information on sediment formation which reflects properties and changes in the sedimentary environment. Molluscan ecology, isotope geochemistry, sedimentation times and CT-based rock density changes show a strong correspondence implying that millennial-scale climatic oscillations are clearly recorded in carbonate formations of Holocene alkaline ponds of the Danube-Tisza Interfluve in southern Hungary. Seasonal temperature change affects directly the rate of evaporation which increases with a rise in temperature, increasing salt concentration and pH in the lake water. This generally leads to precipitation of high-magnesium calcite which turns into protodolomite, dolomite syngenetically in the alkaline ponds. Rocks composed of such carbonate minerals are characterised by higher densities, as reflected in positive shifts of Mean HU values. In periods of lower evaporation, higher humidity, and rainfall the photosynthetic activity of algae is the predominant controlling factor in carbonate formation, resulting in the precipitation of dominantly calcite rather than high-magnesium calcite characterised by lower densities and as such lower Mean HU values. Thus, application of the CT method and complex statistical analysis of the data gained seem to be suitable for revealing small-scale (millennial, centennial) sedimentary cycles recording past Palaeoenvironmental changes.

IV. The use of CT analysis in revealing structural heterogeneity of freshwater carbonate decoration and construction stones: implications for conservation.

Nour Alzoubi*, Sandor Gulyas, Janos Geiger

University of Szeged, Department of Geology, 2-6 Egyetem u., H-6722,

Szeged, Hungary.

e-mails:

Nour Nayef HassanAlzoubi

nouralzoubi@geo.u-szeged.hu,

corresponding author

János Geiger

geostatisztika@gmail.com,

Sandor Gulyas

csigonc@gmail.com

Archeometriai Műhely

The use of CT analysis in revealing structural heterogeneity of freshwater carbonate decoration and construction stones.

A CT-analízis alkalmazása az építőés díszítőkőként használt édesvízi karbonátos kőzetek szerkezeti elemzésében

Nour Alzoubi-Sándor Gulyás-János Geiger*

Abstract

This article presents the findings of a CT analysis conducted on freshwater carbonate rocks found in the Danube-Tisza Interfluve. These rocks are utilized for both construction and decoration purposes. The aim of the study was to uncover the petrophysical properties of the rocks. The proportions of the main constituents of the rocks carry significant information about the formation and alteration history of sedimentary rocks. To comprehend and assess the nature of these processes, as well as the resulting spatial variations, it is necessary to gather quantitative data on the distribution of these constituents at both macroand microscales. The researchers employed an EM-mixture analysis that considered the density differences among the individual constituents to determine the quantitative characteristics of the main components that form the rocks. By setting a threshold value to distinguish macropores (empty spaces) with lower density values from the solid matrix, the percentage of voids was calculated for each CT slice. The distribution of these voids was examined in three dimensions along all possible axial directions (X, Y, Z). Watershed algorithm, and Laplace operator were applying on selected CT slices that corresponded to areas with similar compositional features. This approach helped identify potential flow directions within the rocks. The spatial distribution and orientation of macropores, which could be visualized using CT at a resolution of over 200 microns without causing damage to the samples, provided valuable insights into the paths through which water could enter the carbonate rocks used for construction or decoration. This information is crucial in understanding structural erosion caused by frost weathering and dissolution via capillary action once a static-state flow is established. Furthermore, these findings complement the results obtained from laboratory geotechnical measurements.

Kivonat

Ez a cikk a Duna-Tisza közén található édesvízi karbonátos kőzeteken végzett CT-elemzés eredményeit mutatja be. Ezeket a kőzeteket építési és díszítési célokra egyaránt felhasználják. A vizsgálat célja a kőzetek mérnökgeológiai és petrofizikai tulajdonságainak feltárása volt. A kőzetek fő alkotóelemeinek arányai jelentős információkat hordoznak az üledékes kőzetek kialakulási és átalakulási történetéről. E folyamatok természetének megértéséhez és értékeléséhez, valamint az ebből eredő térbeli eltérésekhez mennyiségi adatokat kell gyűjteni ezen alkotóelemek eloszlásáról mind makro-, mind mikroszinten. A kutatók a kőzeteket alkotó fő komponensek mennyiségi jellemzőinek meghatározásához egy végtag-alapú elemzést alkalmaztak, amely az egyes alkotóelemek közötti sűrűségkülönbségeket vette figyelembe. Egy küszöbérték beállításával, amely megkülönbözteti az alacsonyabb sűrűségértékkel rendelkező makropórusokat (üres tereket) a szilárd mátrixtól, kiszámították az üregek százalékos arányát minden egyes CT-szeletre. Ezeknek az üregeknek az eloszlását három dimenzióban vizsgáltuk az összes lehetséges tengelyirányban (X, Y, Z). A kutatók a Laplace-operátort alkalmazó vízválasztó módszert is alkalmazták a kiválasztott CT-szeleteken,

amelyek hasonló összetételi jellemzőkkel rendelkező területeknek feleltek meg. Ez a megközelítés segített azonosítani a kőzeteken belüli lehetséges áramlási irányokat. A makropórusok térbeli eloszlása és orientációja, amelyeket a CT segítségével több mint 200 mikron felbontással lehetett láthatóvá tenni anélkül, hogy a minták károsodtak volna, értékes betekintést nyújtott azokba az utakba, amelyeken keresztül a víz bejuthatott az építésre vagy díszítésre használt karbonátos kőzetekbe. Ez az információ döntő fontosságú a fagyos időjárás okozta szerkezeti erózió és a kapilláris hatáson keresztül történő oldódás megértéséhez, amint az áramlás állandósult állapotba kerül. Továbbá ezek az eredmények kiegészítik a laboratóriumi geotechnikai mérésekből származó eredményeket.

IV.1. Introduction.

The impact of natural resources on human life is considerable. Finding suitable dwellings has been crucial during life journey. As civilization progressed, people use various materials like mud and stone to construct their buildings, (Dubravka et al. 2013; Fodor 2013; Kustár & Szarka 2013). Carbonate rocks have potential economic benefits, ranging from their use as a source of high-quality calcium carbonate to their potential use as building materials (Knauer 1994; Balogh 1994). Freshwater carbonate is an important material in the geological record and has been the subject of various creative implementations and developments recently, which distinguished it from other sedimentary systems (Capezzuoli & Swennen 2017).

Freshwater carbonate rocks have been widely used as construction materials; like building and pathway stones, and decorative elements since ancient times as shown in (Fig. IV-1). In Hungary, many ruins from the Arpadian age, such as churches and houses were built using carbonate rocks (Dubravka et al. 2013; Fodor 2013; Kustár & Szarka 2013). Local quarries were used to extract rocks for construction purposes, mainly in churches and windmills as shown in Figure (IV-1). Its shallow depth and easy access encouraged residents to work in quarries and use this hard rock in the foundation and walls of their buildings (Fig. IV-2-G) (Molnár and Botz 1996, Dubravka et al. 2013; Fodor 2013; Kustár & Szarka 2013). The freshwater carbonate rock found in Csólyospálos was formed during the late Pleistocene and Holocene in a hypersaline lake between dunes. The freshwater carbonate sequence consists of multiple lithified strata overlain by non-lithified dolomite mud covered by the topsoil.

Limestone is commonly used as a construction material that is constantly exposed to various physical, chemical, and biological factors causing changes. However, depending on their composition, porosity, and texture, some carbonate rocks (such as porous, soft limestone) are especially prone to weathering, which is physical and chemical weathering that is caused by

Figure IV–1: Medieval church walls and church foundations built of freshwater limestone of the Danube-Tisza Interfluve, Hungary a). Church wall of the monastery of Ecser, b). Church wall of the reconstructed church on Church Hill, Kiskunfélegyháza. c). The Truncated tower of Soltszentimre. d). Ruins at Lajosmizse. e). The foundation of the church of Nyárszentlőrinc. f). The Franciscan church of Kecskemét. g). Wall of the castle in Szeged. h). The foundation of the church at Csengele-Bogárhát. i). The foundation of the church at Lakitelek. photo credit: Zsolt Veres (https://akovekmeselnek.hu)

IV-1. ábra: A Duna-Tisza közi édesvízi mészkőből épült középkori templomfalak és templomalapok, Magyarország a.)Az ecseri kolostor templomfala. b.)A kiskunfélegyházi Templomhegyen lévő felújított templom fala. c.)Soltszentimre Csonka tornya. d.) Romok Lajosmizsén. e.) A nyárszentlőrinci templom alapja. f.)Kecskeméti ferences templom. g.)A szegedi vár fala. h.) A csengele-bogárháti templom alapja. i.) A lakiteleki templom alapja. fotók: Veres Zsolt (https://akovekmeselnek.hu)

water infiltrating the rock's voids (De Muynck et al. 2010). This is because the mineral matrix slowly dissolves through weathering, which leads to increased porosity and ultimately decreased petrophysical properties. Nevertheless, most limestone and dolostone types have proven to be durable materials for construction purposes (Ahmed et al. 2021; Balogh 1994; Knauer 1994). In instances where the mentioned freshwater carbonate rocks are used for construction in Hungary, the major cause of carbonate rock weathering is the absorption of groundwater and infiltration of rainwater, leading to both chemical weathering in freshwater carbonate dissolution and physical weathering due to freeze/thaw processes (Ruedrich et al. 2011, Claes et al. 2016). To ensure the long-term durability of carbonate rocks used for construction and decoration purposes information on their physical properties such as hardness, wettability, water absorption, density, stress-strain, and corrosion resistance are indispensable (Hoek 2004, Lin & Mingzhong 2023). These parameters are generally gained through multiple petrophysical laboratory measurements providing us with petrophysical information representative of the total sample. However, the structure and spatial heterogeneity of the void space being the main mediator of fluid flow leading to structural damages cannot be revealed using these technologies. The analyzed stone varieties can be regarded as weak stone due to their high open porosity and water absorption capacity paired with low mechanical parameters (Uğur and Toklu 2020, Ruedrich et al. 2011).

X-ray computer tomography (CT) allows for scanning rock samples in three dimensions providing us with high-resolution (mm and micrometre-scale) quantitative and qualitative information on the structure (mineral phases, matrix, and voids) (Peng et al. 2012; Sun et al. 2019; Atrash & Felicit 2020). This technique allows researchers to create a digital model that reveals details of the inner structure of the rock, including the rock-forming components (RFC) based on their density differences expressed in Hounsfield units (HU).

The CT technique has been utilized in various sedimentology studies, focusing on both clastic sedimentary rocks (Gooya et al. 2016; Abutaha et al. 2021) and carbonate sedimentary rocks (Alzoubi et al. 2022). Comparing lithified carbonate rock to carbonate mud, it is observed that the former exhibits higher HU values. Additionally, variations in HU can arise from changes in sedimentary texture and bulk density (Geiger et al. 2009). Consequently, area with predominantly low density, mainly consisting of voids. Can be distinguished from regions dominant by high-density matrix. By leveraging CT scans, it is possible to determine the

proportions of RFCs based on differences in mineral and particle density (Warlo et al. 2021) caused by processes such as deposition and diagenesis, which involve voids filled with carbonate cement or leaching. Medical CT scanning can capture voids or empty spaces in materials that are larger than the voxel size (generally greater than 200 microns). Voxel size is figured out by the slice grid resolution (usually 512 * 512 pixels), and the third dimension corresponds to the thickness of the slice (Guan et al. 2019) (Radiology 2013).

These larger voids, known as super capillary pores or macropores, are important because they can allow water to infiltrate significant volumes. How these pores are oriented, connected, and shaped determines how deep water can infiltrate into the material, causing structural changes through processes such as chemical dissolution or freezing/thawing. By mapping the distribution, connectivity, and orientation of mega pores, and the major direction of flow within the material, it may be possible to find surfaces and areas that are less prone to infiltration by rain or groundwater and assess the potential water migration paths within the rock itself. This inflow will have a significant impact on the regions affected by capillary flow within the rock itself. The volume change in the capillary pores during freezing is a major contributor to the weathering of rock. It is important to note. However, that capillarity acting against gravity only occurs when the inflowing water is at static state. So highlighting the distribution of potential water paths can aid to choose the right orientation of slabs, and tiles and the assignment of areas that may require higher insulation to prevent potential structural changes when the material is used in construction (Pini & Madonna 2016). Medical CT scanning can capture voids or empty spaces in 3 dimensions over the scanned materials which reveal the inner details based on the pixel resolution and slice thickness that should be larger than the voxel size (generally greater than 200 microns) to appear in the digital sample.

This study aims to assess the vertical and horizontal spatial variations of void space in selected freshwater limestone samples from the Danube-Tisza Interfluve and assign potential flow paths (PWP) thus identifying zones on differently oriented sample surfaces. This inflow will have a significant impact on the regions affected by capillary flow within the sample itself. The orientation and connectivity of macro-voids also influence PWP patterns. Thus, their spatial analysis is essential for the delineation of vertical and horizontal flow paths.

IV.2. Material and methods

IV.2.1. Study area and samples

The Danube-Tisza Interfluve (DTI) is an area of the southern part of central Hungary bounded by the Danube valley to the west, which is a tectonic depression and has an elevation of 90-100 m above sea level (a.s.l). On the other side, it is bordered by the Tisza Valley to the east, which has an elevation of 80 m a.s.l. DTI morphology is formed by an alteration between loess and wind-blown sand (Fig. IV-2-D) (Lóczy 2015). At the end of the Pleistocene – and the beginning of the Holocene, many hypersaline lakes formed due to high groundwater levels or surface runoff that accumulated precipitation in the lowest points between dunes. The layers of freshwater limestone and dolomite mud were as thin as 10 – 15 cm in some places and as thick as 60 - 110 cm in others (Jenei et al. 2007; Sümegi et al. 2015; Sümegi & Náfrádi 2015). Samples studied in this research derive from one of the oldest quarries found near the village of Csólyospálos in the southeastern part of Bács-Kiskun County (Fig. IV-2 A, B & C). The presence of limestone and dolomite mud in Csólyospálos sets it apart from the surrounding area and gives the village cultural and historical significance as one of UNESCO's geological and natural heritage sites, owning both historical and cultural value, especially since limestone quarrying stopped in the 1970s (Dubravka et al. 2013; Fodor 2013; Kustár & Szarka 2013). The geological profile exposing freshwater carbonate layers of 80-110 cm thickness beneath the 15-30 cm topsoil is easily accessible. The freshwater carbonate sequence overlaying the bedrock of the Late Pleistocene wind-blown sand consists of lower lithified carbonate rocks and an upper loose carbonate which is still unlithified carbonate mud (Fig. IV-2 E, F) (Molnár 1991). Freshwater limestone and dolomite mud were utilized as building materials in the surrounding areas (Fig. IV-1) (Dubravka et al. 2013; Fodor 2013; Kustár & Szarka 2013). Two samples reposited in the sedimentary collection of the Department of Geology and Palaeontology, University of Szeged were subjected to CT scans. Sample I represent members Cs-1 and Cs-2 (between 65 and 90 cm), while sample II represents member Cs-3 (between 60 and 65 cm) (Fig. IV-2–F).

First member Cs-1 is equivalent to Molnár's member A, a 30-40 cm thick dolomitic limestone, stained with iron with a looser structure and vertical veins (Figs. IV-2,3). This member which has no clear upper boundary transitions to member Cs-2.

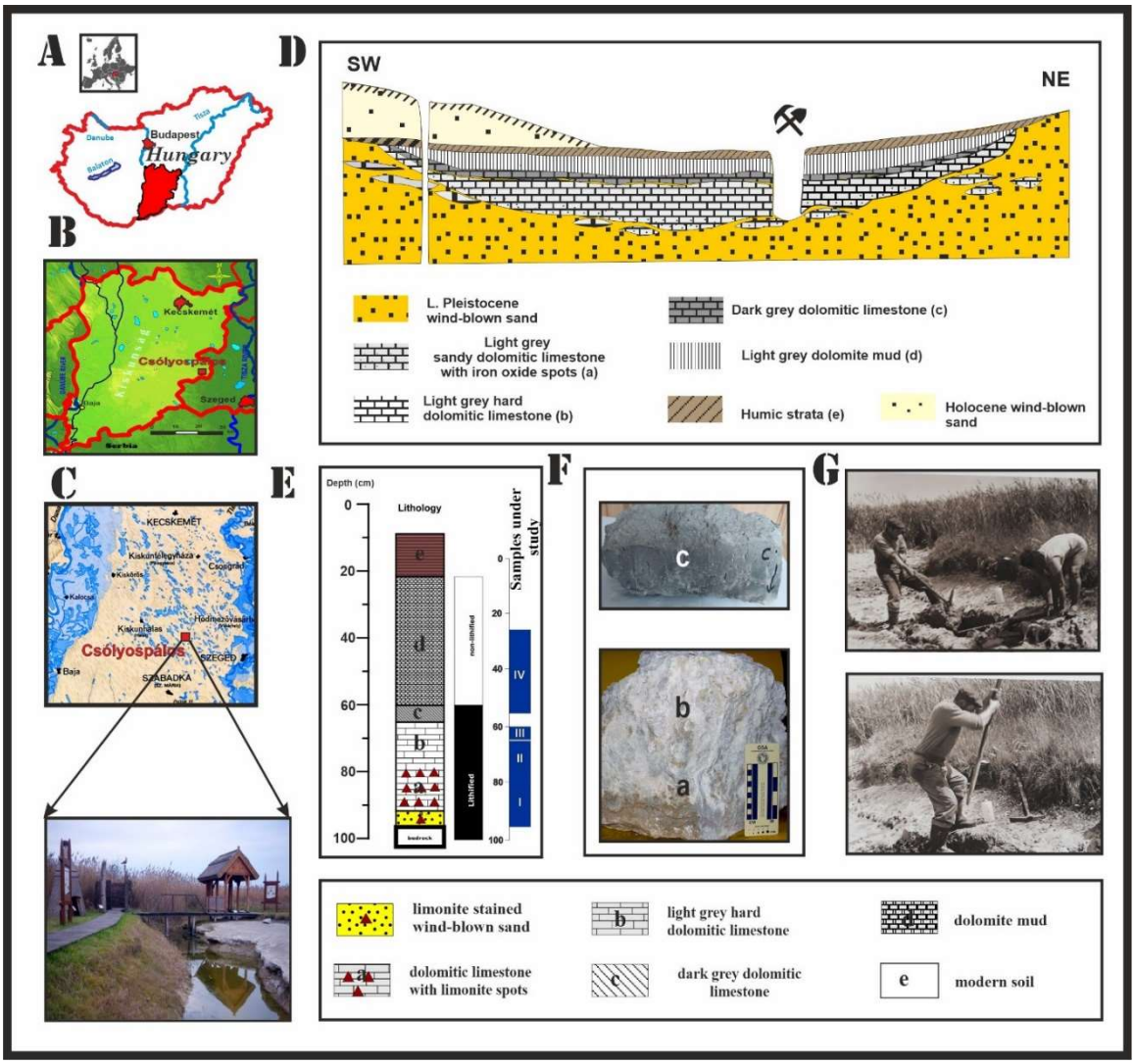

Figure IV–2 Location and stratigraphy of the carbonate sequence studied near Csólyospálos. A – Map of Hungary. B –Location of GHP; C – Hydrography of the area, prior to the late 19th century; D – Geological cross-section of the site. E – Lithology and Schematic log of the outcrop with position of samples under study marked. F – Sample -I (Cs1 – Cs2) ab based on Molnár classified, sample II (Cs3) c based on Molnár classified. G – digging in the quarry before 1970s.

IV-2. ábra: A Csólyospálos közelében vizsgált karbonátos rétegsor elhelyezkedése és rétegsora. A - Magyarország térképe. B - A terület elhelyezkedése; C - A terület vízrajza a 19. század vége előtt; D - A terület geológiai metszete. E - A feltárás litológiái oszlopa a vizsgált minták helyzetével. F - I. minta (Cs1 - Cs2) ab a Molnár B. szerinti besorolás alapján, II. minta (Cs3) c a Molnár B. szerinti besorolás alapján. G – kézi fejtés a kőfejtőben az 1970-es évek előtt.

Cs-2, equivalent to Molnár's member B is a 40-50 cm thick, light grey, dolomitic limestone with vertical vugs measuring several cm, which correspond to roots of former aquatic vegetation. However, this member called by the locals is *honeycomb stone* due to the visible large voids (Fig. IV-1).

There is a distinct lithological boundary between Cs-2 and the overlying member Cs-3. Cs-3 equivalent to Molnár's member C, is a very hard, dark-grey dolomitic limestone that is 5-6 cm thick with the highest carbonate content (>80%) in the entire sequence (Figs. IV-2,3). This member shows vuggy and moldic porosity, including shelter, gas pores, and desiccation or sheet cracks, in addition to vugs corresponding to roots of former vegetation. Not fully consolidated carbonate mud can be seen formed in some pores. Calcisparite partially or completely infills most of the pores, and pore-filling occurs perpendicularly to the pore wall, forming pore-lining structures (Molnár 1991). The carbonates in the sample are classified as wackestone and have a mud-supported texture, as Figured out by the analysis of thin sections. Matrix (carbonate minerals and detrital material) makes up the majority of RFCs around 69%, followed by quartz and feldspar grains at about 13.6%, unfilled pores at up to 12%, carbonate lithics at around 3%, and microsite sparite infilling pores around 2.4%. Tiny amounts of freshwater gastropod shells, calcareous algae oogonia, iron oxides, and manganese minerals are also present (Molnár & Botz 1996; Molnár et al. 1976; Molnár & Szónoky 1974).

IV.2.2. Computer Tomography

Fig. IV-3 presents the workflow adopted in our work. CT was utilized to generate quantitative three-dimensional data, relying on variation in the density of RFCs expressed by the HU (Hounsfield unit, see below) values. X-Ray Computer Tomography (CT) is a modern medical technique, which works by measuring the linear attenuation of X-rays as passing through the object under evaluation. Based on signals through a 180^{o} rotation around the object the detectors receive the transmitted X-rays on the opposite side to produce 3D slices (Hounsfield 1973). During an axial movement, a set of 3D slices creates the volumetric data set. It was developed by Hounsfield and Cormack in 1989 and has undergone various resolution improvements and found applications in non-destructive imaging in fields like geoscience. For instance, CT has been used in palaeontology, clastic rock sedimentology (Földes et al. 2004; Markussen et al. 2019; Abutaha et al. 2021), structural geology to detect faults and fractures (Urbaniec et al. 2018), assess soil porosity (Cnudde et al. 2006), and in engineering (Balázs et al. 2018).

CT images are controlled by various parameters, such as spatial resolution, focal spot size, detector size, crosstalk between detectors, the afterglow of the detectors, and the gantry's rotational velocity. A slice image is reconstructed usually by either a filtered back-projection

or an iterative reconstruction method, which basically applies Beer Lambert's law (equation 1).

$$I = I_o e^{-(\mu d)} \qquad (1)$$

where *I* is the intensity of the transmitted X-ray, I_o is the initial X-ray intensity, μ is the linear X-ray attenuation coefficient of the material and d is the length of the X-ray path inside the material along the beam path in the object. By combining slices, a 3D volume is created (Heismann et al. 2003; Duchesne et al. 2009). A reconstructed slice itself is the map of the linear attenuation coefficient values in that part of the object, which can then be transformed into Hounsfield Units. The Hounsfield unit (HU) is used to express density differences in the CT image data compared to water's density. HU values are determined using equation 2.

$$HU = 10^3 * \frac{\mu - \mu_w}{\mu_w} \qquad (2)$$

where μ is the attenuation coefficient of the material being measured and μ_w is the attenuation coefficient of water. Each HU stands for a 0.1% change in density concerning the calibration density scale. If the measurement is calibrated to distilled water, the resulting HU is 0 for distilled water and -1000 for air.

IV.2.3. Visualization and data analysis

The Siemens SOMATOM Emotion 6 medical scanner at the Department of Radiology, University of Pécs, Hungary was used to conduct CT measurements on two samples that represented lithified members of the freshwater carbonate sequence of Csólyospálos (Cs-1, Cs-2, and Cs-3). The sample I correspond to members Cs-1 and Cs-2 (480 mm * 130 mm * 45 mm), while sample II matches member Cs-3 (240 mm * 180 mm * 100 mm) (as shown in Figs. IV-10 & IV-11). The CT instrument utilized a 140 kVp (peak kilovoltage) setting, with 189 mAs (milliampere-seconds) of current and an exposure time of 1.5 s. The lateral resolution was 0.23 mm × 0.23 mm, with a scan-layer thickness of 1.5 mm. A 3D volume rendering program (Voxler 4.0) was utilized for viewing, filtering, and data extraction from the CT scan files (DICOM (Digital and Imaging Communications in Medicine)). The dataset was filtered by removing the outer portion of the image, resulting in a centrally located CT brick (subset) that is smaller in volume than the original sample (brick of sample I: 306 mm * 101 mm *31.6mm; brick of sample II: 181 mm * 42.3 mm * 42.2 mm). This was done because scanning artifacts like beam hardening can cause the CT value of a single material to change in various

parts of an image. There is no cupping shape in the slice profile so there is no considerable bias in the HU values in this volume, As seen on (SFig. IV-3). Data for the generated CT bricks were used in further statistical analysis.

The RFCs were defined via EM-mixture analysis. This maximum-likelihood non-hierarchical clustering approach is used to find and approximate the parameters (mean and standard deviation) of two or more univariate normal distributions representing overlapping groups corresponding to RFCs relying on the EM-algorithm of Dempster et al. (1977).

As this study focuses on spatial distribution and orientation of voids in our brick samples, determining only two major rock-forming components was necessary. Histogram thresholding is a technique used in image processing to segment an image into different regions based on the intensity values of its pixels. Histogram thresholding involves selecting a threshold value that separates the image into two or more regions based on the intensity values of the pixels. Pixels with intensity values above the threshold are assigned to one region, while pixels with intensity values below the threshold are assigned to another region. The threshold value can be selected manually or automatically using various algorithms. Histogram thresholding is a simple and effective technique for image segmentation and is widely used in various

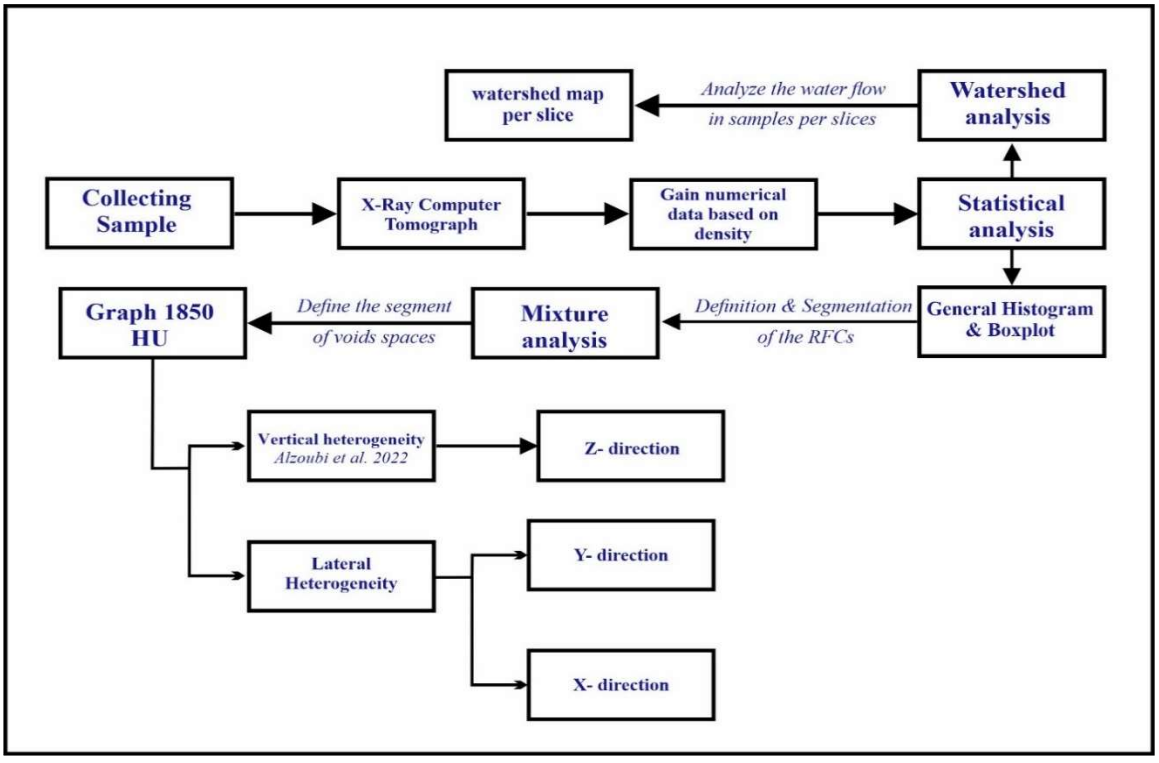

Figure IV–3: : The workflow adopted in our work.
IV-3. ábra Az elemzés lépései

applications, such as object detection, image analysis, and pattern recognition. However, its performance can be affected by factors such as noise, illumination, and image quality, and may require further processing techniques to improve its accuracy. After applying EM-mixture analysis of RFCs on the density frequency histogram a most likely threshold value could be defined. The group having the lowest mean HU value, i.e., being the least dense part, was considered as voids, while the remaining groups of higher mean HU values were taken to represent the higher-density components of the matrix. The threshold boundary between the two was found using the logic presented by (Dawson 2011; Coudray et al. 2013). By drawing linear tangents of the histogram frequency curve at the change in the slope many lines will cross each other which represents the HU value over each crossing point. So, the last cross point with the minimal HU value was chosen as a threshold in this work which ca. 1850 HU. of the univariate frequency distribution representing the density matrix components with higher HU values and the void space at lower HU values. The percentage of RFCs with values less than the mentioned threshold (1850 HU) representing the proportion of the least dense component, i.e., macro voids larger than the resolution of our data (voxel size: 234 µm * 234 µm*1.5 mm) was determined for each slice and plotted. In addition to gaining, a representative value of the overall RFC composition, the mean HU value per slice was also calculated. Calculations (mean HU value, the cumulative percentage of voids) were performed for individual slices in 3 directions depicted in Fig. IV-4: horizontal slices moving from top to bottom along the z-axis, vertical slices moving from left to right along the x-axis, and vertical slices moving from the front to back along the y-axis of the sample brick. This way, we could gain information on the vertical and horizontal heterogeneity of the matrix fabric and the spatial distribution, orientation, and proportion of voids in different samples. The latter also determines the position, length, and orientation of potential water paths (PWP), which serve routes for water entering the sample. To highlight these for selected slices we adopted the method of watershed analysis.

Watershed transformation refers to a geomorphological watershed, or drainage divide, which separates adjacent drainage basins. Intuitively, a drop of water falling on a topographic relief flow towards the nearest minimum. The nearest minimum is that one at the end of the steepest descent path. In terms of topography, this occurs if the point lies in the catchment basin of that minimum (Beucher & Meyer, 1993). A watershed map reads the data from a grid file and splits the grid up into basin, or catchment areas. The number of basins depends on the areas of the

individual basins and is determined by the number of upstream cells that are flowing into the grid cells. The larger the threshold value the smaller the number of identified basins is. The calculation of flow lines (flow paths) is based on the amount of flow into the grid node from all surrounding grid nodes. These lines connect the low points on the map. There are several algorithms for watershed transformation (e.g., Beucher & Meyer 1993, Wang & Liu 2006). In this paper, we applied a topological (accurate eight-direction four-point) algorithm using the so-called Laplace operator to assign potential areas of dissipation and confluence, so that potential non-real flow paths (PWP) are assigned to the grid at each grid node of the CT slices (Quick start guide Surfer Software 2023).

IV.3. Results

IV.3.1. Sample I (CS-1 and CS-2 members)

IV.3.1.1: *Horizontal heterogeneity*

Fig. IV-4 presents the results of the analysis done on horizontal slices of the first sample (Cs-1 and Cs-2 members) moving in a vertical direction (along the z-axis from bottom to top). The first slice (1) represents the top horizontal part and the last slice (205) the base horizontal part of the brick. This orientation allows us to decipher the horizontal variation in RFCs captured by the mean HU values and those of the voids. The percentage of macro voids (> 200 microns) ranges between 0.05 and 1.24 % with an average of approximately 0.56%.

Each zone is defined by the bottom and top slice number and represented by an average slice to describe the potential water paths through the zone. From the bottom, the first zone (Slices 205 to 184) is characterized by high mean HU values (2620 – 2611) and a relatively smaller proportion of macro voids (0.67 - 0.33%). In the second zone, there is a gradual increase in macro voids (1.24%) with a peak value in slice 109 parallel with decreasing mean HU values down to 2459 HU. In the third zone between slices 109 and 34, there is a gradual increase in the density up to 2592 HU alongside decreasing proportions of macro voids to values of 0.07%. Between slices 34 – 17, we can define zone four which shows another sharp increase in macro voids percentage up to 1.01 % at slice 17 with decreasing HU values to 2564. The last zone between the slices 17 – 1 shows a gradual decrease in macro voids percentage to 0.32 % with the mean HU density value remaining relatively constant (2538 HU).

Fig. IV-4 also depicts the spatial distribution of macro voids and the density and orientation of water path flow on representative horizontal slices (x, y). The largest percentage of voids is concentrated in the centre of the sample (Zone 2) and the topmost (Zone 5). In Zone 4 below

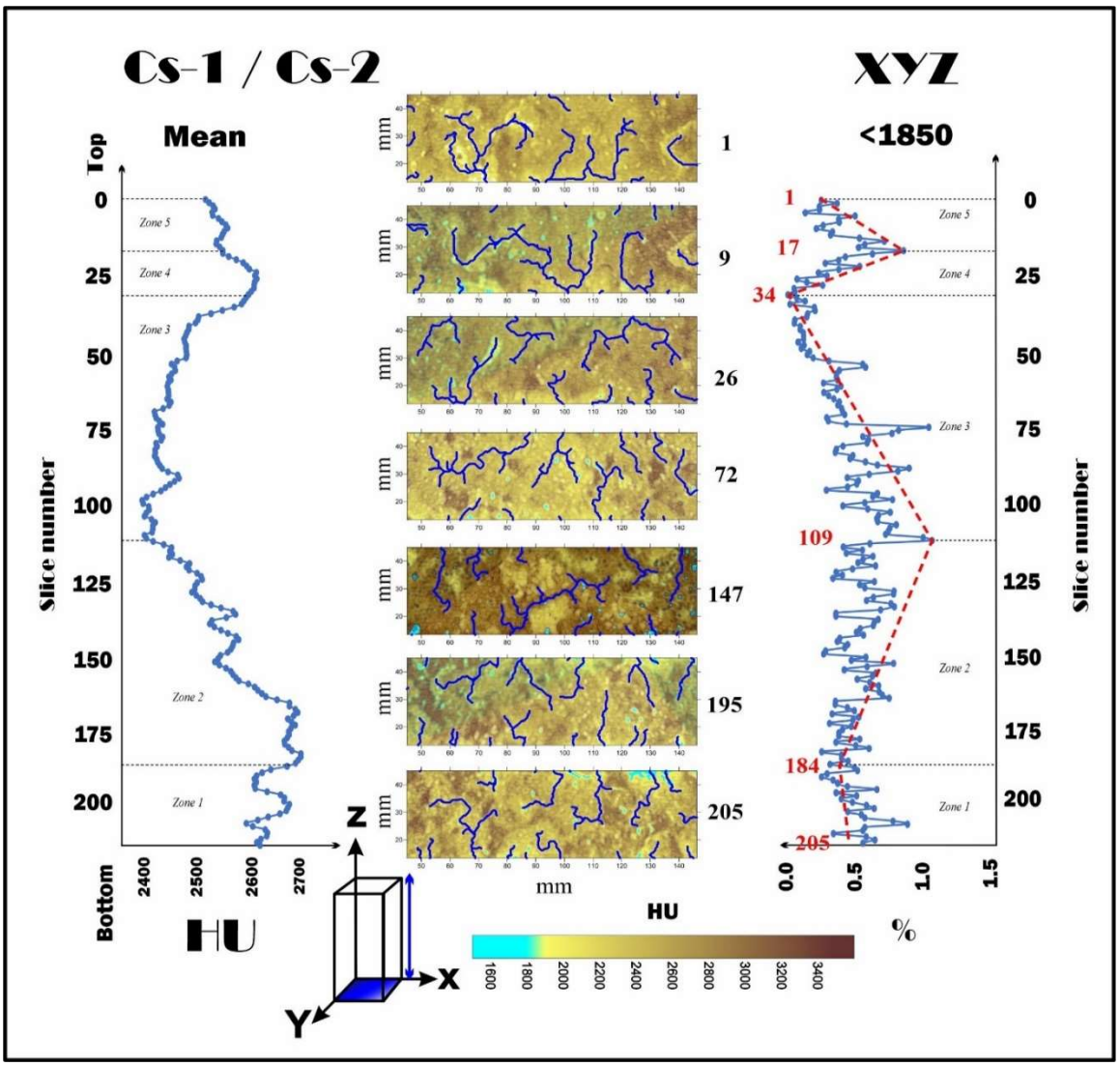

Figure IV–4: Results of analysis done on horizontal slices (x, y) from top (slice 1) to bottom (slice 205) along the vertical axis (z) of the Sample I brick. (Left graph: variation in mean HU values representing density changes in the sample, right graph: percentages of voids, Centre: horizontal slices characteristic of zones defined based on void percentages, light blue colors show areas of macro voids with HU values below the defined 1850 threshold value, darker shades correspond to the matrix numbers on the slices represent distance in mm) .

IV-4. ábra: Az I. minta függőleges tengelye (z) mentén a vízszintes szeleteken (x, y) felülről (1. szelet) lefelé (205. szelet) végzett elemzés eredményei. (Bal oldali grafikon: a minta sűrűségváltozását jelző átlagos HU-értékek változása, jobb oldali grafikon: az üregek százalékos aránya, középen: az üregek százalékos aránya alapján meghatározott zónákra jellemző vízszintes szeletek, a világoskék színek a makroüregek olyan területeit jelzik, amelyek HU-értékei a meghatározott 1850-es küszöbérték alatt vannak, a sötétebb árnyalatok a szeleteken lévő mátrixszámoknak felelnek meg, a szeleteken lévő számok a távolságot jelzik mm-benben.)

Zone 5 the percentage of large voids is close to zero (0.07%) marking the presence of a good aquitard horizon which could protect the vertical inflow of water to deeper layers if these voids are communicating. In Zone 1 the percentage of macro voids is also minimal (0.33%) but not as low as in Zone 4, so here the larger volume of voids may mediate water flow into the sample.

The longest water path flow (PWP) is mainly parallel to the y-axis on both sides in all zones. However, The PWP parallel to the x-axis is minimal, as shown in (Fig. IV-4). They are generally confined to the left top (slices 184,109,1) and left central (slice 34) part of the slices where macropores appear to be oval-shaped and generally isolated (slice 109 blue areas). So, horizontal inflow is generally possible from back to front of the brick in all slices and water can infiltrate as deep as the centre of the sample. It is important to note that flow paths running parallel with the y-axis are less bifurcating, but due to their considerable length and density. These potential voids are more likely to keep water in them, and because of changes in the weather temperature, the periodicity of freezing and melting may reduce the efficiency and durability of the stone.

IV.3.1.2: *Vertical lateral heterogeneity*

The analysis of vertical lateral heterogeneity has been done for both x and y directions. Results of analysis done on vertical slices (z, y) from left (slice 1) to right (slice 434) along the horizontal axis (x) of the Sample I brick are presented in Fig.IV-5. The percentage of macro voids ranged from 0.09 to 1.28%, with an average of approximately 0.44%. Starting from the left side, the first zone, which accounted for almost half of the sample (Slices 1 to 224), displayed low mean Hounsfield unit (HU) values (2653-2469) and a relatively higher proportion of macro voids (0.16-1.26%). Moving further into the sample, the second zone shows a lower percentage of macro voids (0.55%), with an increase in the HU value up to 2655 HU from slice 434. Likewise, to the results of horizontal heterogeneity analysis PWPs (Potential Water Paths) are mainly horizontal running parallel with the Y axis of the brick and are concentrated mainly between 100 and 300 mm. However, vertical paths also appear in the central part of the slices where larger pores showing good connectivity and vertical orientation are present (e.g., slice 224). Most horizontal PWPs start from the back of the brick. So similarly, to the findings of horizontal heterogeneity analysis if water can enter the brick horizontally from the back or front part of the sample, when reaching the centre where larger

vertically oriented pores are present it may continue to a vertical path. After freezing, it again results in the complete uniform horizontal disintegration of the sample between 100 and 300 mm on the vertical axis (z).

Results of analysis done on vertical slices (z, x) from the front (slice 1) to back (slice 150) along the horizontal axis (y) of the Sample I brick are presented in Fig.IV-6. Here the percentage of macro voids ranged from 0.20 to 1.73%, with an average of approximately 0.44%. Slices could have been divided into three main zones along the y-direction. From slice 1 to slice 25 there is a marked increase in the density from 2332 up to 2563 HU parallelly with a sharp decrease in the total percentage of void spaces from 1.74 – 0.29 %. The next zone between slices 25 – 112 shows a slight increase in density up to 2576 HU and a tiny increase in the percentage of void spaces to values less than 0.003%. The last zone between slices 112 – 136 stands for a sharp decrease in the density down to 2509 HU and a parallel sharp increase

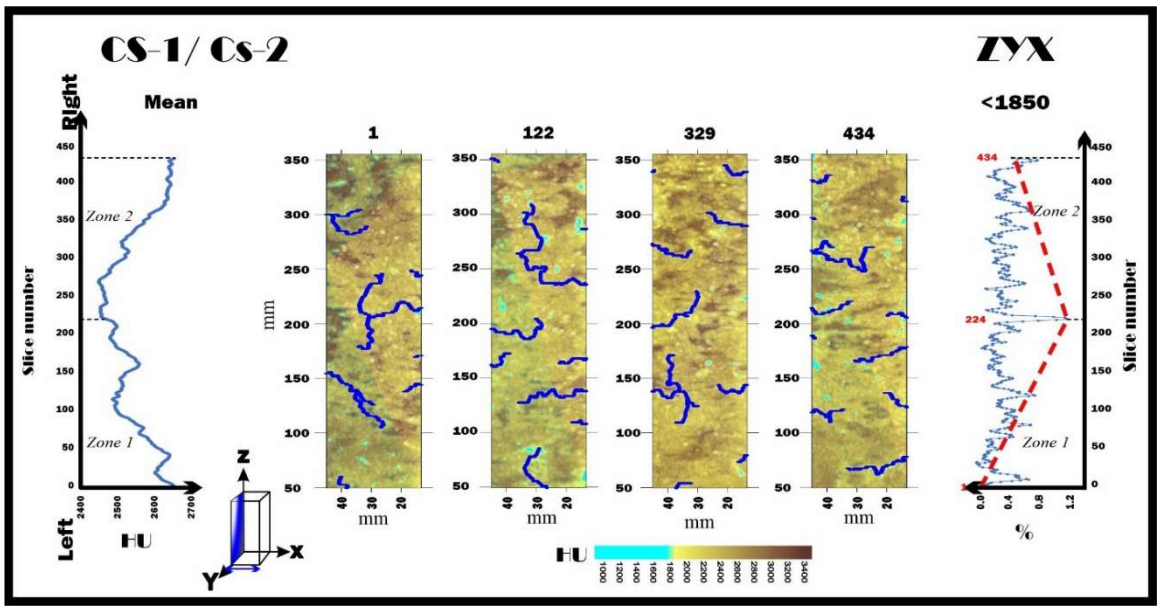

Figure IV–5: Results of analysis done on vertical slices (z, y) from left (slice 0) to right (slice 450) along the horizontal axis (x) of the Sample I brick. (Left graph: variation in mean HU values representing density changes in the sample, right graph: percentages of voids, Centre: vertical slices characteristic of zones defined based on void percentages, light blue colors show areas of macro voids with HU values below the defined 1850 threshold value, darker shades correspond to the matrix, numbers on the slices represent distance in mm).

IV- 5. ábra: Az I. minta vízszintes tengelye (x) mentén balról (0. szelet) jobbra (450. szelet) a függőleges szeleteken (z, y) végzett elemzés eredményei. (Bal oldali grafikon: a minta sűrűségváltozását jelző átlagos HU-értékek változása, jobb oldali grafikon: az üregek százalékos aránya, középen: az üregek százalékos aránya alapján meghatározott zónákat jellemző függőleges szeletek, a világoskék színek a makroüregek területeit jelzik, amelyek HU-értékei a meghatározott 1850-es küszöbérték alatt vannak, a sötétebb árnyalatok a mátrixnak felelnek meg, a szeleteken lévő számok a távolságot jelzik mm-ben).

in the void's percentage up to 1.02 %. So, the largest percentage of voids is confined to the front and back part of the brick (zones 1 and 3), while the proportion of macro voids is relatively small in the central parts. This is also seen in the density values where zones 1 and three have lower densities and generally higher densities characterize the central part of the brick (zone 2).

So, the proportion of the matrix which gives better physical stability against weathering is higher in the centre. It is also clear that most voids are vertically oriented and show good connections, especially in the central part of the slices between 100 and 300 mm (Fig. IV-6) like the results of the previous vertical heterogeneity analysis (Fig. IV-5). This holds for all zones.

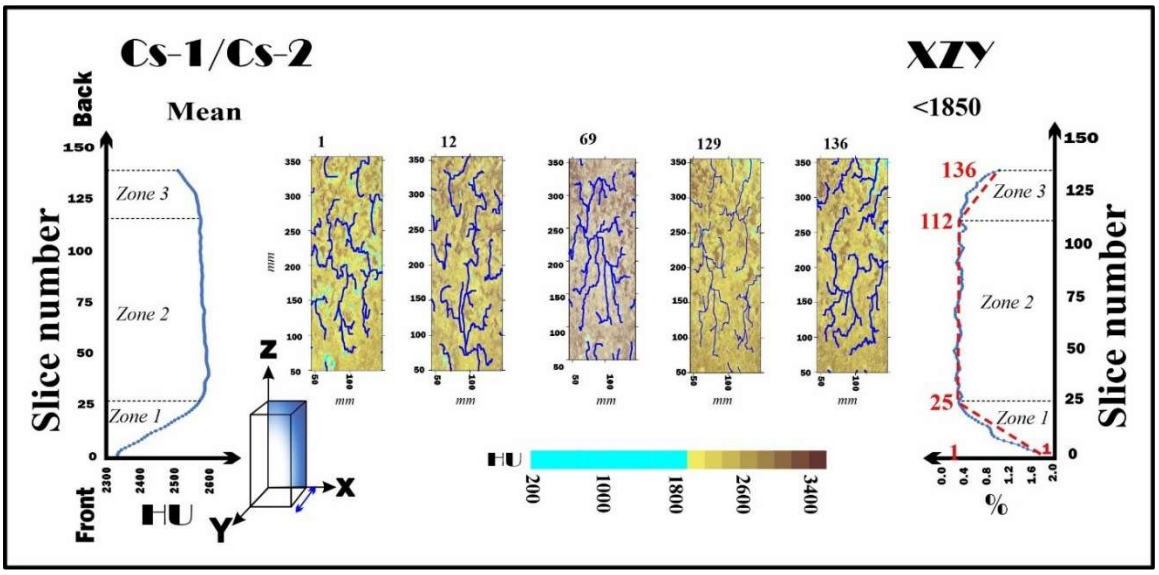

Figure IV–6: Results of analysis done on vertical slices (z, x) from front (slice 0) to back (slice 150) along the horizontal axis (y) of the Sample I brick. (Left graph: variation in mean HU values representing density changes in the sample, right graph: percentages of voids, Centre: vertical slices characteristic of zones defined based on void percentages, light blue colors show areas of macro voids with HU values below the defined 1850 threshold value, darker shades correspond to the matrix, numbers on the slices represent distance in mm).

IV-6. ábra: Az I. minta vízszintes tengelye (y) mentén az elülső (0. szelet) és a hátsó (150. szelet) függőleges szeleteken (z, x) végzett elemzés eredményei. (Bal oldali grafikon: a minta sűrűségváltozását jelző átlagos HU-értékek változása, jobb oldali grafikon: az üregek százalékos aránya, középen: az üregek százalékos aránya alapján meghatározott zónákra jellemző függőleges szeletek, a világoskék színek a meghatározott 1850-es küszöbérték alatti HU-értékkel rendelkező makroüregek területeit mutatják, a sötétebb árnyalatok a mátrixnak felelnek meg, a szeleteken lévő számok a távolságot jelentik mm-ben).

IV.3.2. Sample II (CS-3)

IV.3.2.1: *Horizontal heterogeneity*

In (Fig. IV-7), the analysis of the second sample (Cs-3 member) was done on horizontal slices which move in a vertical direction along the z-axis from bottom to top. Also here, the first slice (1) represents the base, and the last slice (182) is the top horizontal part of the brick. With this approach, both the voids' and the mean HU values' representations of the horizontal variance in RFCs can be understood. The percentage of macro voids has a range from 0.04 BVS (Below Voxel Size) to 6.60%, with an average of about 2.16%. From the bottom, the first zone is between Slices 1 and 69, indicated by close to zero macro voids percentage (approximately 0.04% at Slice 1 displaying a slight increase to the end of the zone to ca. 0.20%). This zone has the highest densities recorded with values between 2845 and 2816. The second zone is between slices 69 to 106, characterized by a significant decrease in density down to 2620 HU, alongside the increase in the proportion of macro voids to values as high as 2.58 %. The next zone starts following a break in the trend line right after slice 106 showed a sharp increase in macro voids percentage up to 5.41% with a parallel decrease in the density down to 2542 HU. In zone four starting from slice 147, the percentage of voids keeps increasing up to 6.60% parallel with decreasing density values down to 2474 HU in slice 182.

The sample has a gradual increase in the percentage of voids from the centre to the top (zone 2, 3, and 4). The fraction of voids in Zone 1 is near zero BVS (0.04%), indicating the presence of a relatively good aquitard horizon that may safeguard the vertical influx of water to the layers above (Zones 2-4). PWPs are relatively short in Slice 1, run parallel with the y-axis, and are confined in general to the front and back sides of the brick. There is a single path appearing on the left side of Slice 1. They have the same orientation and distribution in Slice 69, but here PWPs turn longer and new branches running parallel with the x-axis also develop. In addition, the longest PWPs are confined to the front and the proportion of PWPs remains low in the back part of the slice. As seen in slices 1 and 69, despite the low proportion of voids, the horizontal connectivity of the macro voids is good allowing for the infiltration of water from dominantly the front followed by lateral expansion in the upper part of Zone 1. From Zone 2 to Zone 4 despite a steady increase in the proportion and the visible size of macro voids (slice 147: bottom right and top left, slice 182 bottom left and right) the orientation and length as well as the position of PWPs remain relatively the same as at the boundary of Zone 1. This may be

attributed to the relatively considerable number of isolated macropores present in these zones (e. g., slice 106: top right, slice 182: top left).

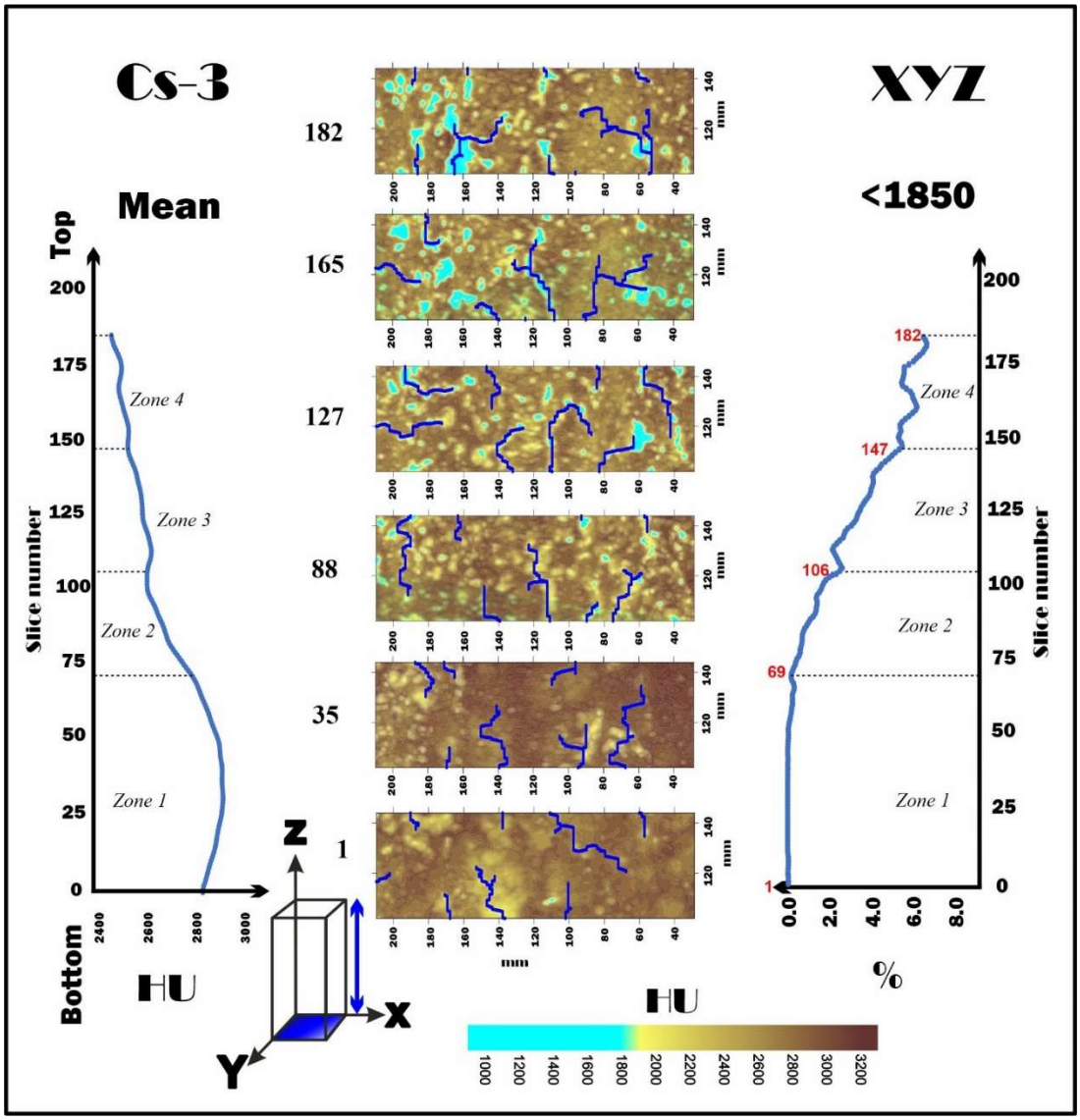

Figure IV–7: Results of analysis done on horizontal slices (x, y) from bottom (slice 0) to top (slice 182) along the vertical axis (z) of the Sample II brick. (Left graph: variation in mean HU values representing density changes in the sample, right graph: percentages of voids, center: horizontal slices characteristic of zones defined based on void percentages, light blue colors show areas of macro voids with HU values below the defined 1850 threshold value, darker shades correspond to the matrix, numbers on the slices represent distance in mm)

IV-7. ábra: A II. minta függőleges tengelye (z) mentén alulról (0. szelet) a tetejéig (182. szelet) vízszintes szeleteken (x,y) végzett elemzés eredményei. (Bal oldali grafikon: a minta sűrűségváltozását jelző átlagos HU-értékek változása, jobb oldali grafikon: az üregek százalékos aránya, középen: az üregek százalékos aránya alapján meghatározott zónákra jellemző vízszintes szeletek, a világoskék színek a makroüregek olyan területeit jelzik, amelyek HU-értékei a meghatározott 1850-es küszöbérték alatt vannak, a sötétebb árnyalatok a mátrixnak felelnek meg, a szeleteken lévő számok a távolságot jelzik mm-ben).

IV.3.2.2: *Vertical lateral heterogeneity*

The analysis of vertical lateral heterogeneity has been done for both x and y directions. Results of analysis done on vertical slices (z, y) from left (slice 1) to right (slice 122) along the horizontal axis (x) of the Sample II brick are presented in Fig. IV-8. Void percentage is between 1% and 4 %. The outlier value of 10% is attributable to the appearance of those two exceptionally large pores which are characterized by large pores by a high diameter~20 mm in Fig. IV-8 slices 21 and 87. Moving from the left side, the first zone of the sample (Slice 1 to 21) displays low mean HU values (2892-2609) and a relatively higher proportion of macro voids (1.67-10.26%). The second zone shows a sharp decrease in percentage macro voids to 0.34% at Slice 28 with a slight in the density up to 2708 HU. The third zone, found between Slices 28 and 87, indicates a clear increase in the proportion of macro voids up to 7.02% with 2713 HU. Finally, the last zone, found between Slices 87 and 122, points to a decrease in the proportion of macro voids down to 2.96% with densities decreasing to 2679 HU. Here both the density and the void percentage values remain relatively constant as appeared in Fig.IV-8.

The other minor peaks that were considered correspond to zone boundaries and are interpreted as a sharp increase to 7.02% at slice 87 is probably an artifact of the appearance of large pores. So, it seems that void percentage and density remain uniform vertically in the sample, and large increases are attributable to the irregular appearance of exceptionally large macropores. Looking at Fig. 8 displaying changes from the front to the back of the brick, it can be seen that vertical PWPs appear systematically and at the same intervals where your peak void % values are noted in this part. What is visible is that PWPs are longer, more bifurcated, and mainly vertically oriented. They are connected to the exceptionally large macropores in general and their number is relatively small (2 -3) which may be attributed to the fact that these large macropores are the mediators of water flow and the remaining pores are mostly isolated as reflected in the low (2-4%) void percentage values in general. It is also worth noting that the largest pores and the most developed PWP are restricted to the left part of the brick (slices 1, 21, and 87) and the right (slices 1, 28, and 122).

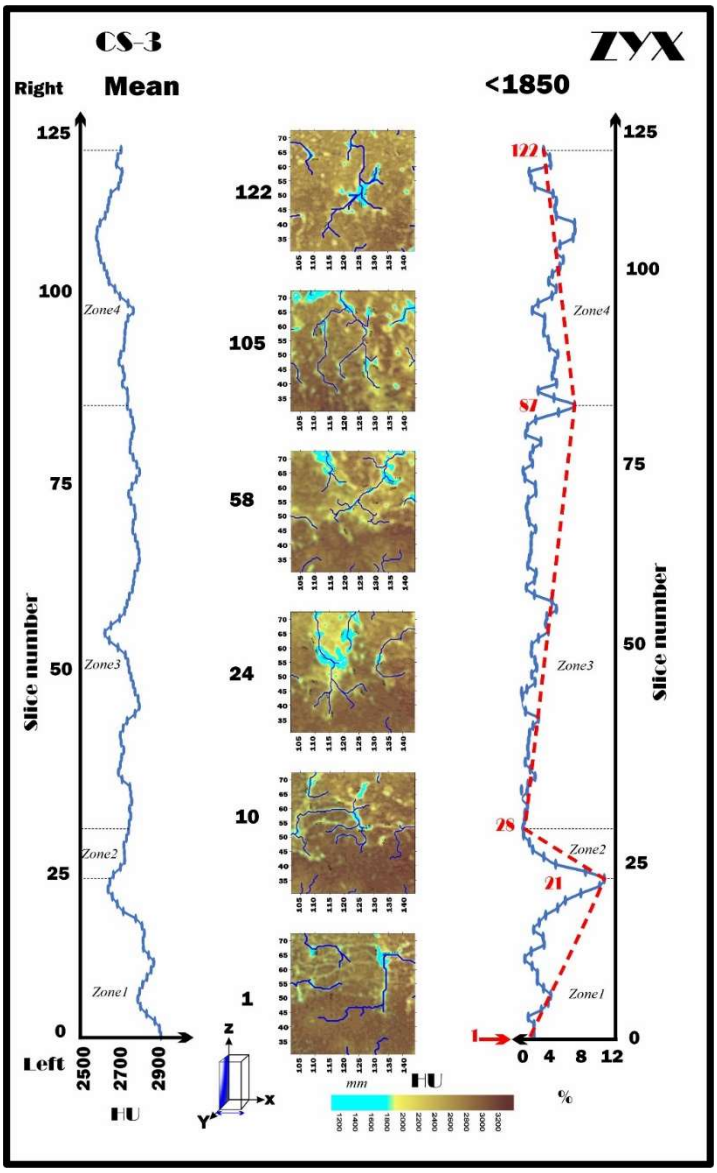

Figure IV–8: Results of analysis done on vertical slices (z, y) from bottom (slice 0) to top (slice 122) along the horizontal axis (x) of the Sample II brick. (Left graph: variation in mean HU values representing density changes in the sample, right graph: percentages of voids, Centre: horizontal slices characteristic of zones defined based on void percentages, light blue colors show areas of macro voids with HU values below the defined 1850 threshold value, darker shades correspond to the matrix, numbers on the slices represent distance in mm).
IV-8. ábra: A II. minta vízszintes tengelye (x) mentén alulról (0. szelet) felfelé (126. szelet) függőleges szeleteken (z,y) végzett elemzés eredményei. (Bal oldali grafikon: a minta sűrűségváltozását jelző átlagos HU-értékek változása, jobb oldali grafikon: az üregek százalékos aránya, középen: az üregek százalékos aránya alapján meghatározott zónákra jellemző vízszintes szeletek, a világoskék színek a makroüregek olyan területeit jelzik, amelyek HU-értékei a meghatározott 1850-es küszöbérték alatt vannak, a sötétebb árnyalatok a mátrixnak felelnek meg, a szeleteken lévő számok a távolságot jelzik mm-ben).

Fig. IV-9 also supplies the vertical distribution of macro voids along the y-axis from front to back of the brick, the density, and orientation of water path flow on representative horizontal slices (z, x). The percentage of macro voids has ranged from 1.05 to 4.05 %, with an average of about 2.34%. Here, seven main zones were interpreted. From the front, the first zone (Slice 1 to 13) displays a slightly increasing in mean HU values (2696 – 2713) and a relatively lowest proportion of macro voids by the end of this zone (2.10 - 1.05%) which indicates in this zone the water will flow down to the centre of the sample and will not infiltrate deeply as shown in Fig. IV-9 slice (1, 13). The Second zone is between slices 13 and 40 representing a sharp increase in the proportion of void percentage up to 3.71 % and slightly decreasing in the mean density down to 2659 HU. The next one of the longest zones, the third zone, which lies between

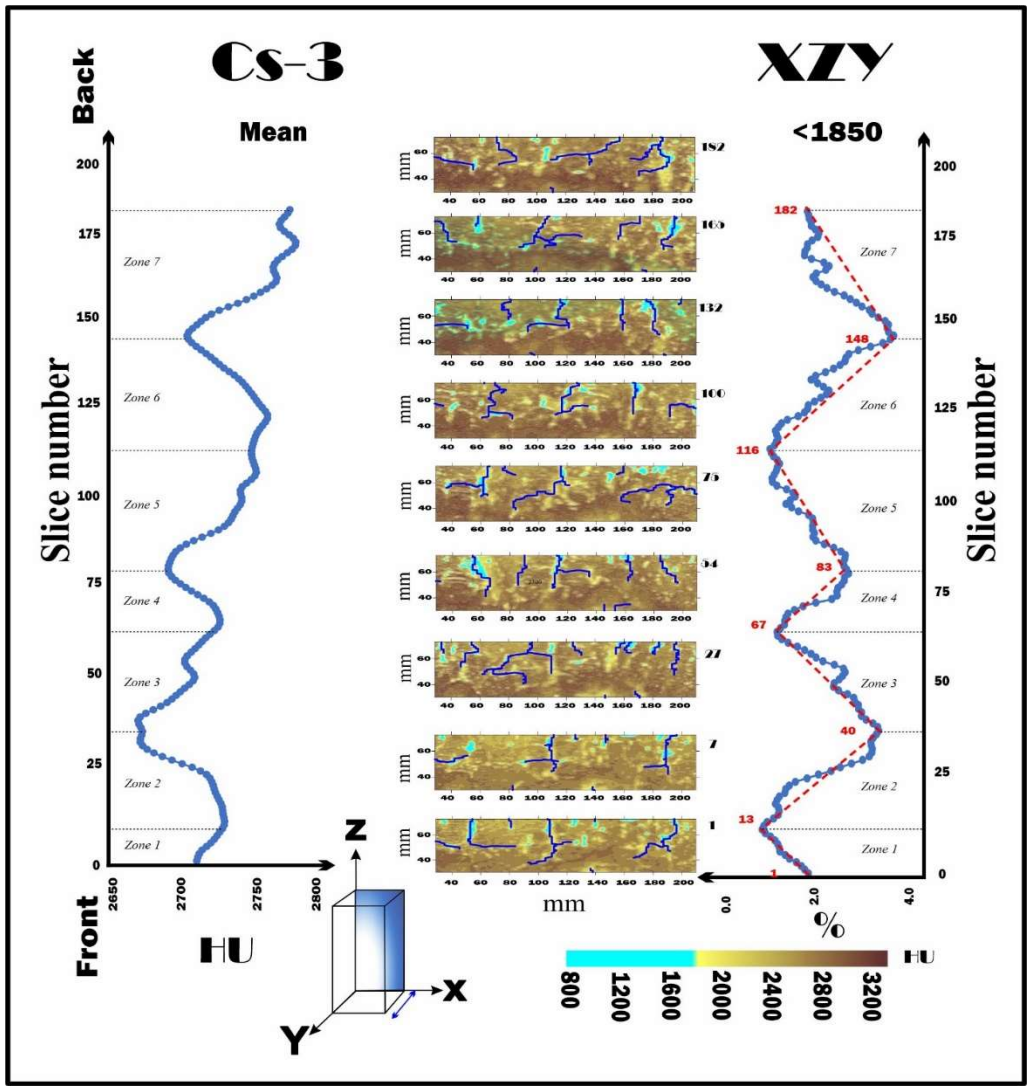

Figure IV–9: Results of analysis done on vertical slices (Z, X) from front (slice 1) to back (slice 182) along the horizontal axis (y) of the Sample II brick. (Left graph: variation in mean HU values representing density changes in the sample, right graph: percentages of voids, center: vertical slices characteristic of zones defined based on void percentages, light blue colors show areas of macro voids with HU values below the defined 1850 threshold value, darker shades correspond to the matrix, numbers on the slices represent distance in mm).
IV-9. ábra: A II. minta elülső (1. szelet) és hátsó (182. szelet) függőleges szeletein (Z, X) végzett elemzés eredményei a vízszintes tengely (y) mentén. (Bal oldali grafikon: a minta sűrűségváltozását jelző átlagos HU-értékek változása, jobb oldali grafikon: az üregek százalékos aránya, középen: az üregek százalékos aránya alapján meghatározott zónákra jellemző függőleges szeletek, a világoskék színek a makroüregek olyan területeit jelzik, amelyek HU-értékei a meghatározott 1850-es küszöbérték alatt vannak, a sötétebb árnyalatok a mátrixnak felelnek meg, a szeleteken lévő számok a távolságot jelzik mm-ben).

slices 40 and 67, has sharply decreased in the void percentage down to 1.39 % while the mean density increases up to 2710 HU which shows a repeat of the first zone density. The next increasing zone is the second zone shows a high proportion of voids but not high as the second zone here is only up to 3.02 % alongside decreasing in the density down to 2678 HU. At slice

116 the percentage of voids decreased to 1.26 % parallel to a sharp increase in the HU up to 2731. The sixth zone between 116 and 148 has the highest peak on the proportion of void percentage up to 4.05 % and 2691 HU. The last zone up to the last slice 182 has 2.08 % of the void percentage and the highest density value up to 2754 HU.

Fig. IV-9 also describes the spatial distribution of macro voids and the density and orientation of water path flow on representative horizontal slices (x, z). The largest percentage of voids is concentrated in the top of Zones 2, 4, and 6 with relative percentages of 3.71, 3.02, and 4.05%, respectively. The minimal percentage greater than 1 % shows the voids spread over the slice even if there are no connections as appears on slices 13, 67, 116, and 182. The longest water path flow (PWP) is mainly parallel to the z-axis, mainly from the top in all zones. However, some isolated short PWP appears from the bottom on slices 1, 40, 16, 148, and 182. The PWP.

parallel to the x-axis is minimal, as shown in (Fig. IV-9) only on slices 1, 13, and 182 from the left side, and on slices 40, 67, and 83 from the right side. Where macropores appear to be oval-shaped and generally isolated. Thus, horizontal inflow is generally possible from left and right, and water can infiltrate as deep as the centre of the sample. It is important to note that flow paths running parallel with the X-axis are less bifurcating, but due to their considerable length and density if water collects in them and freezes it results in a relatively uniform disintegration of the sample.

IV.4. Discussion and Interpretation

Investigating the void area percentage over the samples in various positions gives information about the surface and inside void spaces in addition to PWPs in various directions. Based on our findings of the analysis implemented on vertical and horizontal slices of Sample I the front and the back of the brick appear to be more porous and prone to water uptake than the left and the right sides of the central part. It is seen in all slices that the length and proportion of PWPs are negligible on the sides of the brick. So, these lateral parts are less prone to water uptake. Conversely, water may enter the pores from the front, or the back of the brick will be first moving horizontally toward the centre. Once it reaches the interior parts due to the good connectivity and significant percentage of vertically oriented pores flow continues upwards and downwards. Thus, the front and the back brick position needs good insulation to prevent

the inflow of water to the central parts. In the lateral areas, minimal insulation is acceptable, as shown in Fig. IV-10.

The investigation was also carried out on vertical and horizontal slices of Sample II in Fig. IV-11. The top of the brick appears to be more porous and susceptible to water absorption than the horizontal sides. The length and quantity of PWPs on the top of the brick are visible in all slices. As a result, this vertical region is highly susceptible to water absorption. Water possibly will also enter the pores from the front or rear of the brick, moving horizontally toward the centre. However, water will enter the bricks less from left or right. Because of the strong connection and high proportion of vertically oriented voids, flow continues upwards and downwards once it reaches the internal portions. Consequently, the front and back ends of Sample II require sufficient insulation to prevent water from entering the inner components. In the lateral portions, only bare essential insulation is needed.

IV.5. Conclusion

This research is looking to identify potential weaknesses that may arise from water infiltrating the rock which was used in ancient structures and archaeological buildings. However, in turn, helps in determining the cost and points of treatment required for the original stone and its sustainability. Quantifying voids spaces larger than voxel size (>200 μm) and detecting the potential flow path in freshwater carbonate rock for construction and decoration purposes is fundamental for facilitating and implementing protection for constructed areas. Moreover, it is crucial to forecast these vulnerabilities considering the predicted diurnal variation of temperature, resulting in increased freeze and thaw frequency from severe weather events. To achieve this aim, we used EM-mixture analysis of the CT data to segment RFCs and watershed algorithms to detect the potential of the water flow path.

By showing the spatial distribution and orientation of the potential watershed path (PWP) we can estimate the areas that require enhanced insulation to prevent water inflow and structural damage into the rock. These non-destructive methods provide better insight into the structural heterogeneity of construction stones and complemented by the results of ultramodern petrophysical measurements can supply better models of weathering effects. The advantages of the method include its non-destructive nature, the ability to obtain visual and quantitative data on rock composition, and the possibility of segmenting rock-forming components (voids

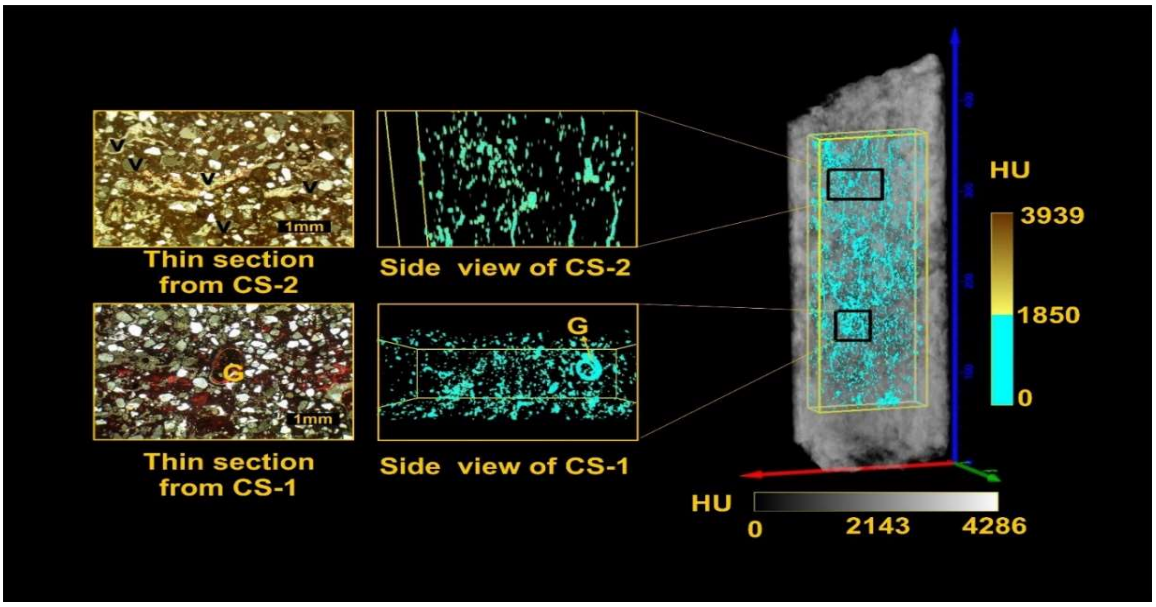

Figure IV–10: 3D void space in sample I, on the right, is the original sample in greyscale, and the rectangle shows the subset of the sample, the blue shape represents the void space area over the sample's subset in 3D, the black cube shows a side view of void space in Cs-1, the rectangle illustrates the void space in Cs-2, representative thin sections from each member parallel to void space location, V: voids, G: gastropods
IV-10. ábra A jobb oldali I. mintában lévő 3D üres tér az eredeti minta szürkeárnyalatos, és a téglalap a minta részhalmazát mutatja, a kék alakzat a minta részhalmaza feletti űrt jelöli 3D-ben, a fekete kocka oldalnézetben A téglalap a Cs-1 üregterét szemlélteti a Cs-2-ben, reprezentatív vékony szakaszok minden egyes elemtől párhuzamosan az üregtér elhelyezkedésével. V: üregek, G: haslábúak

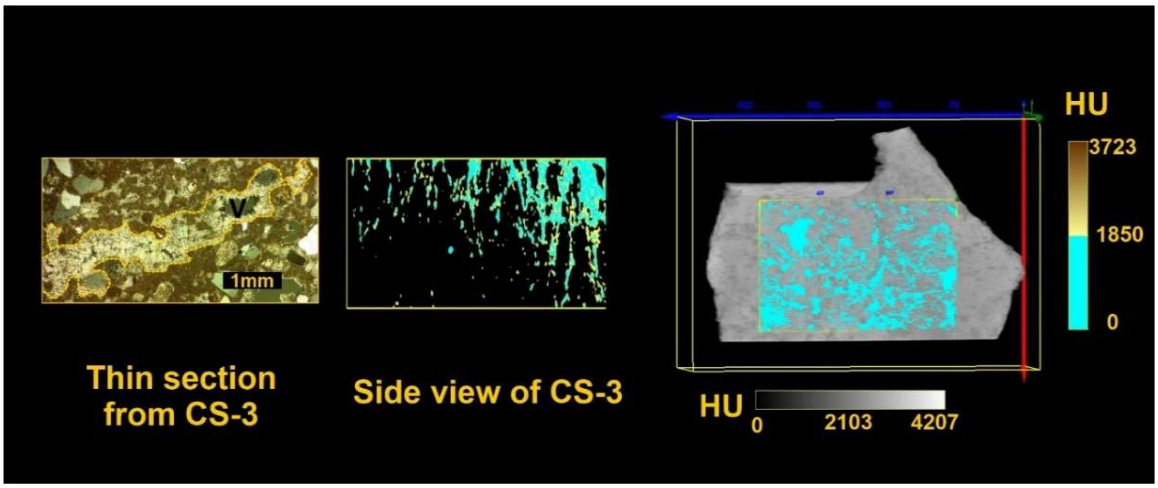

Figure IV–11: 3D void space in sample II, on the right, is the original sample in greyscale, and the inside rectangle shows the subset of the sample, the blue shape represents the void space area over the sample's subset in 3D, then in the center of figure a side view of void space in Cs-3, on the left side, a representative thin sections from the member parallel to void space location, V: voids.
11. ábra A 3D-s üregtér a II. mintában, a jobb oldalon, az eredeti minta szürkeárnyalatos, a belső téglalap pedig a minta részhalmazát mutatja, a kék alak a minta részhalmaza feletti űrt jelöli 3D-ben, majd az ábra közepén. a Cs-3 üregének oldalnézete, bal oldalon, reprezentatív vékony metszetek az elemtől párhuzamosan az üregek elhelyezkedésével, V: üregek.

and matrix) using statistical approaches. Furthermore, it allows estimation of the percentage of rock-forming components for the entire sample and assessment of spatial variation along the major axes of the studied sample, slice by slice. The method also enables the identification of zones with similar density characteristics and composition, facilitating the evaluation of the distribution, percentage, and orientation of voids within these zones. Additionally, by reconstructing potential flow paths, it becomes possible to determine the major direction of flow for each identified zone separately. The 3D visualization of the data enables assessment of the type, orientation, and connectivity of the voids.

This study is limited to using representative samples of the lithified section of freshwater carbonate from Csólyospálos, which probably give precise results if the lithified samples are taken from different points over the dry lake. The results of this work give a preliminary indication of the major direction of voids which are the main potential water paths during water infiltration. One more limitation is that the analysis is unable to detect micro-voids due to their size being smaller than the resolution offered by the medical CT (< 200 microns). Consequently, these micro-voids are not accounted for in the analysis.

V. Thesis Summary

This research focuses on the study of sedimentary rocks, in particular freshwater carbonates, as a paleoenvironmental and paleoclimatological record. Computer tomography (CT) analysis provides quantitative data based on rock-forming component (RFC) density differences, which allows insight into sedimentary environmental changes over time. The CT data are consistent with the results of geochemical and palaeoecological studies, providing a useful tool for understanding carbonate heterogeneity and refining rock nomenclature.

The study applied statistical and geostatistical tools to evaluate and visualize the heterogeneity of carbonate block samples based on density values obtained from CT images expressed in HU. Density values obtained from CT data correlate with the density of different rock-forming components present in the carbonates, and EM mixture analysis was used to successfully segment and identify different RFCs using CT data. In contrast to the rock component estimates based on thin sections, the CT data provide better estimates of the total sample volume, suggesting that the rock nomenclature needs to be reconsidered based on CT analysis.

The study also investigates the formation of freshwater carbonates in the Great Plain and their relationship with hydrological and climatic conditions. The study evaluates the temporal variation of carbonate rock-forming components quantified by CT on a millennial scale in terms of hydrological and climatic factors controlling the formation of carbonates, thus their potential use as a paleoclimatic and paleohydrological proxy. We also investigated spatial variations in the void spaces of freshwater carbonate samples, to explore how changes in void volume caused by water infiltration into the rock and then flow through pores, dissolution, freeze-thaw and weathering affect the malleability of rocks in areas more exposed to weathering, for use as building and ornamental materials, and to assess their vulnerability. This information will help to identify rock surfaces requiring increased insulative properties for construction and decoration.

The importance of quantifying non-destructively cavity spaces using CT and exploring potential water flow paths in freshwater carbonate rocks is emphasised. CT analysis, combined with modern geotechnical measurements, contributes to models for a better understanding of weathering effects on building rocks. The results suggest the use of conservation treatments, such as water repellents, to protect the preserved rocks from corrosion by water and weathering

in certain parts of the rock surface. Mapping the distribution, connectivity and orientation of megapores in the rock will allow the identification of surfaces and regions less susceptible to water infiltration. This analysis helps to select the optimum orientation of slabs and tiles and identifies areas that may require increased waterproofing during construction to prevent possible structural changes.

Overall, the research provides new insights into the freshwater carbonates of the Great Plain, including their rock-forming components, paleoenvironmental and paleohydrological setting, petrophysical properties and controlling factors. The application of CT analysis is valuable in understanding the micro-scale complexity of carbonate systems and in promoting effective conservation measures (Pini and Madonna, 2016).

The study of quaternary freshwater carbonate from the Great Hungarian Plain has produced important new results concerning the freshwater carbonate in the hypersaline lake in GHP, the rock-forming components, the palaeoclimatic and palaeohydrological conditions during the late Pleistocene and Holocene, in addition to petrophysical properties such as void space larger than 200 microns, and the freshwater carbonate controlling factors:

Defining rock-forming components of Holocene freshwater carbonates via univariate statistical and mixture analysis of computer tomography data.

1- The research conducted on four carbonate samples from Csolyospálos utilized computed tomography (CT) scanning to investigate and record the heterogeneity and textural characteristics of the carbonates. The study found that CT analysis offers a more objective and direct approach compared to traditional thin-section analysis. The quantitative data obtained through CT analysis in three dimensions enables a comprehensive evaluation of the entire sample, including detailed micro-scale resolution. In contrast, thin sections provide limited information as they rely on selectively chosen subsamples of small (couple of square mms) parts and being also subjective estimations.

2- By using CT data we investigated lithified and unlithified freshwater carbonate samples. We applied an EM-mixture analysis algorithm to determine the HU range of each rock forming component known from the textural analysis of previous studies. For the lithified samples the following intervals were defined for each RFC: empty pores < 850 HU, filled or partially filled pores between 600 - 2500 HU, calcium

carbonate matrix between 2000 – 3100 HU, high magnesium carbonate matrix between 2500 – 3200 HU, high-density matrix components and limonite between 2800 – 3400 HU. On the other hand, RFCs of the non-lithified samples had somewhat different ranges: the empty pores < 550 HU, filled or partially filled pores between 300 - 1900 HU, calcium carbonate matrix between 1300 – 2300 HU, high magnesium carbonate matrix between 1600 – 3100 HU, high-density matrix components 2500 – 3200 HU.

3- We calculated the relative percentage of each component, and the average percentage of the lithified samples were as follows: empty pores ~ 0.13%, filled or partially filled pores 18.37%, calcium carbonate matrix 62.0 %, high magnesium carbonate matrix 14.3%, high-density matrix components and limonite 5.2%. For non-lithified samples the following values were received: empty pores ~ 1.65 %, filled or partially filled pores 40.5%, calcium carbonate matrix ~55.35%, high magnesium carbonate matrix 1.25%, high-density matrix components 1.25%. To provide an example, the characteristics of the minerals that make up rocks were matched with descriptions of samples given by Molnár (1991).

Palaeoenvironmental and palaeoclimatic inferences based on X-ray computer tomography: a case study of alkaline lake deposits in Hungary.

1- X-ray computer tomography (CT) allows for quantitative data based on density differences of RFCs, providing insights into sediment formation and environmental properties through time at high resolution. Density changes in the matrix, as captured by medical CT, correspond to climatic oscillations and precipitation patterns in carbonate formations at high resolution. Changes in evaporation rates, temperature, and rainfall influence the type of carbonate minerals precipitated, leading to variations in densities. The CT method, combined with statistical analysis, proves effective in revealing millennial and centennial sedimentary cycles and past paleoenvironmental changes.

2- Analysing computer tomography data, colder conditions in the North Atlantic from 10.3 to 9.3 thousand years before the present (kilo-years Cal BP) had a notable impact on freshwater carbonate formation in the GHP. These conditions led to increased humidity, resulting in a rise in the groundwater table and the precipitation of dominantly calcite from pore waters instead of high-magnesium calcite. The negative

shifts in CT density values in the dated rock samples depicted these changes clearly and showed a good correlation with isotope geochemical and paleoecological data of previous studies (molnar 1996).

The use of CT analysis in revealing structural heterogeneity of freshwater carbonate decoration and construction stone.

1- Zones are defined based on the major trend changes in the percentage of void space and the mean value; therefore, some directions could contain only two zones such as (ZYX sample I), and others involved seven zones like (XZY sample II).
2- Macro-CT scanned data revealed voids which are greater than voxel size. Major trending was vertical with horizontal connected from the front and back sides once the water reaches the interior parts, the good connectivity and vertically oriented pores facilitate upward by capillary action and downward flow by gravity.
3- The analysis of Sample I revealed that the front and back of the brick had higher porosity and greater susceptibility to water absorption compared to the left and right sides of the central part. This indicates the need for effective insulation in the front and back positions to prevent water ingress into the central areas.
4- The lateral areas of the brick displayed negligible lengths and proportions of potential water pathways (PWPs), making them less prone to water uptake. Consequently, minimal insulation can be deemed acceptable for these regions, reducing the risk of water infiltration.

Acknowledgement

First of all, I would like to express of my deepest thankful and grateful to my supervisor, Sandor Gulyas to give me this chance to work in this exciting topic, and for his patience, continuous support, help and his high commitment in the project work. I appreciatively thank Prof. Janos Geiger, for his assistance and fruitful discussions since the beginning of the project till the end. I would like to thank the committee members and all reviewers for their time, and valuable comments to move this work forward and improve the scientific results. I don't want to forget to say thank you Stipendium Hungariucum and University of Szeged to give me this opportunity.

I am happy to say thank you for all my colleagues Soblasz Borka, Reka, Reka, Balasz, Mate, Laszlo Mako, Peter, Saja, Abdelrahim, and Zoltan for all time and discussions, support, and help, and I don't want to forget department members David, Janina, Balint and all friends in Hungary for a few times discussions. Furthermore, the brilliant team in TIK library for their cooporation and kindness.

I am grateful with endless support and patience, I would like to say a lot of thanks to my mother, my brothers and sisters with their support and encourage, they change my down times during COVID and whole abroad time. All my family members uncles, Aunts and cousins thank you for every single word that supported me to be here now.

This work has been partially supported by NSF Grant K129265, and grants by the European Union, and the State of Hungary, co-financed by the European Regional Development Fund in the projects of GINOP-2.3.2-15-2016-00009 'ICER'" as well as the Ministry of Human Capacities, Hungary Grant 20391-3/2018/FEKUSTRAT.

I would like to say thank you also to Sedsonline members for the coffee breaks discussion and their encouragement and support; Stephan locker, Valentin Zuchuat, Catherine Russell, Camille Thomas, and Or Bialik.

Last but not least, I don't want to forget my support members from my MSc. Degree; Najib Abou Karaki, Khaldoon Abu Hamideh and Nasir Hasweh for their endless support that encourage me to be here today.

References

Abutaha, S., Geiger, J., Gulyás, S., & Fedor, F., 2021. “Evaluation of 3D Small-Scale Lithological Heterogeneities and Pore Distribution of the Boda Claystone Formation Using X-Ray Computed Tomography Images (CT).” Geologia Croatica 74(3): 305–18. Doi: 10.4154/gc.2021.17

Ahmed, H., Ghni, J., & Murtadha J. 2021. “Petrophysical Study of Limestone Rocks for Al- Nfayil Formation – Bahr Al-Najaf Depression and Suitability for Industrial Purposes.” Journal of university of Babylon for pure and applied science (JUBPAS) 29(1): 75–85.

Akaike, H., 1974. “A new look at statistical model identification”. Institute of Electrical and Electronics Engineers IEEE 19/6, 716–723. Doi: 10.1109/TAC.1974.1100705

Alzoubi, N., Geiger, J. & Gulyas, S., 2022. “Defining rock-forming components of Holocene freshwater carbonates via univariate statistical and mixture analysis of CT data”. Studia Quaternaria 39,113-128. Doi: 10.24425/sq.2022.140887.

Atrash, Hasan, & Felicitász Velledits. 2020. “CT based analysis of pore network of reservoir rocks.” Geosciences and Engineering 8(13): 167–84.

Balogh, K., 1994. “History of the Hungarian geological survey from 1869 to 1919”. 125 years of Hungarian geological survey history.

Bender, M.L., Lorens R.B., Williams, D.F., 1975. “Sodium, Magnesium and Strontium in the tests of planktonic foraminifera”. Micropaleontology 21 (4), 448–459.

Bolliger, S.A., Oesterhelweg, L., Spendlove, D., Ross, S., Thali, M.J., 2009. “Is Differentiation of Frequently Encountered Foreign Bodies in Corpses Possible by Hounsfield Density Measurement?”. American Academy of Forensic Sciences. 54 (5), 1119–1122. Doi: 10.1111/j.1556-4029.2009.01100. x.

Bhattacharyya, K., 2016. "Godfrey Newbold Hounsfield (1919-2004): The man who revolutionized neuroimaging". Annals of Indian Academy of Neurology 19, 448–50.

Blaauw, M., Christen, J.A., Benett, K.D. & Reimer, P.J., 2018. "Double the dates and go for Bayes-Impacts of model choice, dating density, and quality of chronologies". Quaternary Science Reviews 188, 58-66.

Bond, G., Showers, W., Cheseby, M., Lotti, R., Almasi, P., deMenocal, P., Priore P., Cullen, H., Hajdas, I. & Bonani, G., 1997. "A pervasive millennial-scale cycle in North Atlantic Holocene and glacial climates". Science 278, 1257-1266.

Bond, G., Kromer, B., Beer, J., Muscheler, R., Evans, M.N., Showers, W., Hoffmann, S., Lotti-Bond, R., Hajdas, I. & Bonani, G., 2001. "Persistent solar influence on North Atlantic climate during the Holocene". Science 294, 2130–2136.

Balázs, György L., Éva Lublóy, & Tamás Földes. 2018. “Evaluation of Concrete Elements with X-Ray Computed Tomography.” Journal of Materials in Civil Engineering 30(9): 1–9.

Beucher, S., & Meyer, F., 1993. “The Morphological Approach to Segmentation: The Watershed Transformation”. In Advances of Mathematical Morphology in Image Processing, 433–481.

Capezzuoli, Enrico, & Rudy Swennen. 2017. “Non-Marine Carbonates: A Multidisciplinary Approach.” Quaternary International 437: 1–3.

Chen, Y., Shen, A., Pan, L., Zhang, J. & Wang, X., 2017. “Features, origin, and distribution of microbial dolomite reservoirs: a case study of 4th member of Sinian Dengying Formation in Sichuan Basin, SW China”. Petroleum Exploration and Development 44, 745-757.

Choquette, P.W., Pray, L.C., 1970. “Geologic nomenclature and classification of porosity in sedimentary carbonates”. American Association of Petroleum Geologists Bulletin 54, 207–250.

Claes, Steven, Jeroen Soete, Veerle Cnudde, & Rudy Swennen. 2016. “A Three-Dimensional Classification for Mathematical Pore Shape Description in Complex Carbonate Reservoir Rocks”. Mathematical Geosciences 48(6): 619–39.

Cnudde, V., Masschaele, B., Dierick, M., Vlassenbroeck, J., Van Hoorebeke, L., Jacobes, P., 2006. “Recent progress in X-ray CT as a geosciences tool”. Applied geochemistry 21 (5), 826–832. Doi: 10.1016/j.apgeochem.2006.02.010

Coudray, N., Buessler, J.,& Urban, J. 2013 "A robust thresholding algorithm for unimodal image histograms". Pattern Recognition Letters, 31, pp.1010-1019. 10.1016/j.patrec.2009.12.025. hal-00827953

Dawson, Robert. 2011. “How Significant Is a Boxplot Outlier?” Journal of Statistics Education 19(2).

De Boever, W., Derluyna, H., Van Loob, D., Van Hoorebekec, L., Cnudde, V., 2015. “Data-fusion of high-resolution X-ray CT, SEM and EDS for 3D and pseudo-3D chemical and structural characterization of sandstone”. Micron 74, 15–21. Doi: 10.1016/j.micron.2015.04.003.

De Muynck, Willem, Nele De Belie, and Willy Verstraete. 2010. “Microbial Carbonate Precipitation in Construction Materials: A Review.” Ecological Engineering 36(2): 118–36.

Dempster, A.P., Laird, N.M. & Rubin, D.B., 1977. “Maximum likelihood from incomplete data via the EM algorithm”. Journal of Royal Statistical Society 39, 1-38.

Dubravka, Đu., Sava, St., Ljiljana, Ći., 2013. “A réti mészkő felhasználásának kutatása a Bácska és Bánát északi részén a „CULT-NAT HERIT” elnevezésű Magyarország–Szerbia IPA határon átnyúló együttműködési program keretében". A DARÁZSKŐ. Kecskemét, 131 - 146 pp.

Duchesne, M.J., Moore, F., Long, B.F. & Labrie, J., 2009. “A rapid method for converting medical Computed Tomography scanner topogram attenuation scale to Hounsfield Unit scale and to obtain relative density values”. Engineering Geology 103, 100–105

Duliu, O.G., 1999. "Computer axial tomography in geosciences: An overview". Earth Science Reviews 48, 265–81.

Fang, Y., Xu, H., 2019. “A new approach to quantify the ordering state of Protodolomite using XRD, TEM, and Z-contrast imaging”. Journal of sedimentary research 89 (6), 537–551. Doi:10.2110/jsr.2019.29

Fodor, G. 2013. "Darázskő szunnyad lejjebb a pagonyban” A DARÁZSKŐ. Kecskemét, p. 7.

Földes, T.B., Kiss, G., Árgyelán, P., Bogner, I. & Repa, K. Hips. 2004. “Application of medical computer tomography measurements in 3D reservoir characterization”. –Acta Geologica Hungarica, 47/1, 63–73. Doi: 10.1556/AGeol.47.2004.1.5

Fourar, M., Konan, G., Fichen, C., Rosenberg, E., Egermann, P., Lenormand, R., 2005. “Tracer tests for various carbonate cores using X-Ray CT”. International Symposium of the Society of Core Analysts, Toronto, Canada, SCA2005-56.

Gaines, A.M., 1977. “Protodolomite redefined”. Journal of Sedimentary Petrology 47, 543-546

Geiger, Janos, Zoltan Hunyadfalvi, & Peter Bogner. 2009. “Analysis of Small-Scale Heterogeneity in Clastic Rocks by Using Computerized X-Ray Tomography (CT).” Engineering Geology 103(3–4): 112–18. http://dx.Doi.org/10.1016/j.enggeo.2008.06.011.

Gooya, R., Bruns, S., Müter, D., Moaddel, A., Harti, R. P., Stipp, S. L. S., & Sørensen, H. O., 2016. "Effect of Tomography Resolution on the Calculated Microscopic Properties of Porous Materials: Comparison of Sandstone and Carbonate Rocks." Applied Physics Letters 109(10): 1–5. http://dx.Doi.org/10.1063/1.4962389.

Guan, Kelly M. et al. 2019. "Effects of Image Resolution on Sandstone Porosity and Permeability as Obtained from X-Ray Microscopy." Transport in Porous Media 127(1): 233–45. https://doi.org/10.1007/s11242-018-1189-9.

Hammer, Ø., Harper, D.A.T. & Ryan, P.D., 2001. "PAST: Palaeontological statistics software package for education and data analysis". Palaeontologia Electronica 4, 1-9.

Hammer, Ø., Harper, D.A.T., Ryan, P.D., 2001. "PAST: Paleontological Statistics software package for education and data analysis". 275 pp.

Heismann, B.J., Leppert, J. & Stierstorfer, K., 2003. "Density and atomic number measurements with spectral x-ray attenuation method". Journal of Applied Physics 94, 2073-2079.

Hicks, P.J., Ram Narayanan, K. & Deans, H.A., 1994. "An experimental study of miscible displacements in heterogeneous carbonate cores using X-ray CT". Society of Petroleum Engineers Formation Evaluation, 55- 60.

Hoek, Evert., 2004. "Practical Rock Engineering.". 237pp.

Hounsfield GN. 1973. "Computerized transverse axial scanning (tomography)". 1. Description of system. British Journal of Radiology. 46(552):1016-22. Doi: 10.1259/0007-1285-46-552-1016. PMID: 4757352.

Jenei, M., Gulyás, S., Sümegi, P. & Molnár, M., 2007. "Holocene lacustrine carbonate formation: old ideas in the light of new radiocarbon data from a single site in central Hungary". Radiocarbon 49, 1017-1021.

Kak;, Avinash C., and Malcolm Slaney. 1999. The lnstitute of Electrical and Electronics Engineers. Principle of Computerized Tomographic Imaging. xxpp

Kenter, J.A.M., 1989. "Applications of Computerized Tomography in Sedimentology". Marine Geotechnology 8 (3), 201–211. Doi: 10.1080/10641

Kercsmár, Z., 2015. "Surface geology of Hungary. Geological study". Geological and Geophysical Institute of Hungary, 66 pp.

Ketcham, R.A. & Carlson, W.D., 2001. "Acquisition, optimization, and interpretation of X-ray computed tomographic imagery: Applications to the geosciences". Computers and Geosciences 27, 381-400.

Knauer, J., 1994. "Contribution to mineral exploration". 125 years of Hungarian geological survey history.

Kustár, R., & Szarka, J., 2013. "A réti mészkő felhasználása a Duna–Tisza közén". A DARÁZSKŐ. Kecskemét, 87- 131 pp.

Lazareth, C.E, Vanderputten, E., André, L. & Dehairs, F., 2003. "High-resolution trace element profiles in shells of the mangrove bivalve Isognomon ephippium: a record of environmental spatiotemporal variations". Estuarine, Coastal and Shelf Science 57, 1103-1114.

Lin Chan, Choi, & Mingzhong Zhang. 2023. "Effect of Limestone on Engineering Properties of Alkali-Activated Concrete: A Review." Construction and Building Materials 362 (October 2022): 129709. https://Doi.org/10.1016/j.conbuildmat.2022.129709.

Lóczy, Dénes. 2015. "Geomorphological Regions." In Landscapes and Landforms of Hungary, 227–35.

Magny, M., Bégeot, C., Guiot J. & Peyron, O., 2003. "Contrasting patterns of hydrological changes in Europe in response to Holocene climate cooling phases". Quaternary Science Reviews 22, 1589-1596.

Magny, M., Leuzinger, U., Bortenschlager, S. & Haas, J.N., 2006. "Tripartite climate reversal in Central Europe 5600-5300 years ago". Quaternary Research 65, 3-19.

Markussen, Ø., Dypvik, H., Hammer, E., Long, H. & Hammer, Ø., 2019. "3D characterization of porosity and authigenic cementation in Triassic conglomerates/arenites in the Edvard Grieg field using 3D micro-CT imaging". Marine and Petroleum Geology 99, 265-281. Doi: 10.1016/j.marpetgeo.2018.10.015.

Maurício, A., Pereira, M.F., Rocha, C., Figueiredo, C. & Marques, J.M., 2017. "X-ray micro-CT study of Cabeço De Vide serpentinites and carbonate rock samples: a preliminary approach". Procedia Earth and Planetary Science 17, 952-955. Doi: 10.1016/j.proeps.2017.01.034.

Mcconnaughey, T., 1991. "Calcification in Chara Corallina: CO2 hydroxylation generates protons for bicarbonate assimilation". Limnology and Oceanography 36, 619–28.

Miháltz, I., 1947. "A Duna-Tisza – csatorna geológiai viszonyainak tanulmányozása" – A Duna-Tisza – csatorna, A Magyar Földmívelésügyi Minisztérium kiadványa, Budapest, 3–12 (in Hungarian).

Miháltz, I., 1953. "A Duna-Tisza köze déki részének földtani felvétele" – MÁFI évi jelentése az 1950. Évről" [Geological survey of the southern part of the Danube-Tisza junction - MÁFI annual report for the year 1950], 113–148 (in Hungarian).

Miháltz, I. & Faragó, M., 1946. "A Duna-Tisza közi édesvízi mészkőképződmények" [Freshwater limestone formations between the Danube and Tisza]. Az Aéfölf Tudományos Intézet 1944-45. évi Évkönyve 1. Szeged, pp. 371-384 (in Hungarian).

Molnár, B., 1961. "A Duna-Tisza közi eolikus rétegek felszini és felszin alatti kiterjedése" – Földtani Közlöny 91.3, 294–297 (in Hungarian).

Molnár, B., 1970. "On the origin and hydrogeology of natron lakes in the southern great Hugarian palin", Móra Ferenc Múzeum Évkönyve/1, 65–76.

Molnár, B., 1976. "Recent lacustrine dolomite formation in The Great Hungarian Plain". Acta Geologica Academai Socientiarum Hungaricae 20, 179-198.

Molnar, B., 1980. "Diagenetic and lithification processes of recent hypersaline dolomites on the danube-tisza interfluve". Mineralogical Magazine 24, 315–37.

Molnár, B., 1980. "Hiperszalin dolomitképződés a Duna-Tisza közen" – Földtani Közlöny 100.1, 45–64 (in Hungarian).

Molnár, B., 1981. "Szeimentológia I. k." – JATE TTK egzetemi jegyzet, Szeged. 298 p. (in Hungarian).

Molnár, B., 1983. "A Duna-Tisza közi tavak keletkezése, fejlődéstörténete és hasznositása" – Akadémiai Doktori Értekezés, Szeged, 156P. (in Hungarian).

Molnár, B., 1985. "Földtani kutatások a Kiskunsági Nemzeti Parkban – in Tóth K. (szerk.) Tudományos kutatások a kiskunsági Nemzeti Parkban 1975–1984", OKHT kaidása, 29–58 (in Hungarian).

Molnár, B., 1988." Quaternary geohistory of the Hungarian part of the Danube-Tisza Interfluve". Proceedings of geo institute 21, 61– 78, Belgrade.

Molnár, B., 1991. "Modern lacustrine Calcite, Dolomite and Magnesite Formation in Hungary". Publication of the department of Quaternary geology, University of Turku, 1–22.

Molnár, B., 1996. "A szegedi Fehér-tó keletkezése és vízföldtana. Hidrológiai Közlöny" 76. 5., 266–271 (in Hungarian).

Molnár, B., 2000. “A Duna-Tisza köz délnyugati részének negyedidőszak végi földtani fejlődéstörténete”. In: Fábian, Sz.Á. – Tóth J. (Eds.), Geokronológia és domborzati fejlődés, Pécsi Tud. Egyetem Term. Tud. Kar Földrajzi Int. Kiadványa, Pécs, 101–121 (in Hungarian).

Molnár, B., 2015. “A Kiskunsági nemzeti park” – Földtana és vízföldtana, JatePress, 523 pp.

Molnár, B. & Botz, R., 1996. “Geochemistry and stable isotope ratio of modern carbonate in natron lakes of the Danube-Tisza Interfluve, Hungary”. Acta Geologica Hungarica 39, 153-174.

Molnár, B., Hum, L. & Fényes, J., 1995. “Investigation of modern geological processes in Holocene lacustrine carbonates in the Danube-Tisza Interfluve - Hungary.” Acta mineralogica-petrographica, Szeged, 36, 73-87.

Molnár, B., Murvai, M.I., 1976. “A kisunsági Nemzeti Park fülöphaázi szikes tanvainak kialakulása és földtani története” – Hidrológiai kö- zlöny 56. 2, 67–77.

Molnár, B., Murvai, M.I. & Hegyi-Pakó, J., 1976. “Recent lacustrine dolomite formation in The Great Hungarian Plain”. Acta Geologica Academai Socientiarum Hungaricae 20, 179-198

Molnár, B. & Szónoky, M., 1976. “On the origin and geohistorical evolution of the natron lakes of the Bugac Region”. Móra F. Múzeum Évkönyve, Szeged 1974/75, 257-270.

Molnár, S., Bakacsi. Z., Balog, K., Bolla, B. & Tóth, T., 2019. “Evolution of a salt-affected lake under changing environmental conditions in Danube-Tisza Interfluve”. Carpathian Journal of Earth and Environmental Sciences 14, 77–82.

Mucsi, M., 1963. “Finomrétegtani visózsgálatok a kisunsági édesvizi karbonátképződményekben” [Fine-stratigraphic viscosities in the Kisunság freshwater carbonate formations] Földtani Közlöny 93, 373-386 (in Hungarian).

Müller, G., 1970. “High-Magnesian Calcite and protodolomite in lake Balaton (Hungary) sediments”. Nature 226, 749–750.

Müller, G., Irion, G. & Förstner, U., 1972. “Formation and diagenesis of inorganic Ca-Mg carbonates in the lacustrine environment”. Die Naturwissenschaften 59, 158-164.

Müller, G., Wagner, F., 1978. “Holocene carbonate evolution in Lake Balaton (Hungary): a response to climate and impact of man”. special publication IAS international Association of sedimentologists., 2, 57–81.

Oliveira, G., Geia, M., Missagia, R., Neto, I., Santos, V. & Paranhos, R., 2020. “Core plug and 2D/3D-image integrated analysis for improving permeability estimation based on the differences between micro- and macroporosity in Middle East carbonate rocks”. Journal of Petroleum Science and Engineering 193, 107335.

Peng, Sheng, Qinhong Hu, Stefan Dultz, & Ming Zhang. 2012. “Using X-Ray Computed Tomography in Pore Structure Characterization for a Berea Sandstone: Resolution Effect.” Journal of Hydrology 472–473: 254–61. http://dx.Doi.org/10.1016/j.jhydrol.2012.09.034.

Pósfai, M., 2020. “A Balaton üledékének ásványai” (Minerals in the sediments of Lake Balaton). Földtani Közlöny 150/4, 511-528.

Pini, R., & Madonna, Cl., 2016. “Moving across Scales: A Quantitative Assessment of X-Ray CT to Measure the Porosity of Rocks.” Journal of Porous Materials 23(2): 325–38.

Radiology, American College of. 2013. “MRI Accreditation Program Clinical Image Quality Guide Introduction.”: 1–38.

Reimer, P., Austin, W., Bard, E., Bayliss, A., Blackwell, P.G., Ramsey, C., Butzin, M., Cheng, H., Edwards, R., Friedrich, M., Grootes, P., Guilderson, T., Hajdas, I., Heaton, T., Hogg, A., Hughen, K., Kromer, B., Manning, S., Muscheler, R., Palmer, J., Pearson, C., Plicht, J., Reimer, R.,

Richards, D., Scott, E., Southon, J., Turney, C., Wacker, L., Adolphi, F., Büntgen, U., Capano, M., Fahrni, S., Fogtmann-Schulz, A., Friedrich, R., Köhler, P., Kudsk, S., Miyake, F., Olsen, J., Reinig, F., Sakamoto, M., Sookdeo, A. & Talamo, S., 2020. "The IntCal20 northern hemisphere radiocarbon age calibration curve (0–55 cal kBP)". Radiocarbon 62, 725-757.

Richardson, L.L., Aguilar, C. & Nealson, K.H., 1988. "Manganese oxidation in pH and O2 microenvironments produced by phytoplankton". Limnology and Oceanography 33, 352-363.

Ruedrich, J., D. Kirchner, and S. Siegesmund. 2011. "Physical Weathering of Building Stones Induced by Freeze-Thaw Action: A Laboratory Long-Term Study." Environmental Earth Sciences 63(7): 1573–86.

Sun, Hu., Belhaj, Ha., Tao, Gu., Vega, Sa., & Liu, Lu., 2019. "Rock Properties Evaluation for Carbonate Reservoir Characterization with Multi-Scale Digital Rock Images." Journal of Petroleum Science and Engineering 175(March 2018): 654–64. https://Doi.org/10.1016/j.petrol.2018.12.075.

Sümegi, P. & Náfrádi, K., 2015. "A radiocarbon-dated cave sequence and the Pleistocene/Holocene transition in Hungary". Open Geosciences 1, 783-798. Doi:10.1515/geo-2015-0051.

Sümegi, P., Molnár, D., Sávai, S., Náfrádi, K., Novák, Z., Szelepcsényi, Z. & Törőcsik, T., 2015. "First radiocarbon dated palaeoecological data from the freshwater carbonates of the Danube-Tisza interfluve". Open Geosciences 7, 40–52. Doi: 10.1515/geo-2015- 0003

The program, Surfer®, and Golden Software. 2023. "Surfer Quick Start Guide." : 61.

Thompson, J.B., Schultze-Lam, S., Beveridge, T.J., Des Marais, D.J., 1997. "Whitening events: biogenic origin due to the photosynthetic activity of cyanobacterial picoplankton". Limnology and Oceanography 42/1, 133-141.

Tompa, É., Nyírő-Kósa, I., Rostási, Á., Cserny, T., Pósfai, M., 2014. "Distribution and composition of Mg-calcite and dolomite in the water and sediments of Lake Balaton". Central European Geology 57, 113-136.

Tullner, T. & Cserny, T., 2003. "New aspects of lake-level changes: Lake Balaton, Hungary". Acta Geologica Hungarica 46 (2), 215–238.

Uğur, İbrahim, and Hilal Özer Toklu. 2020. "Effect of Multi-Cycle Freeze-Thaw Tests on the Physico-mechanical and Thermal Properties of Some Highly Porous Natural Stones." Bulletin of Engineering Geology and the Environment 79(1): 255–67.

Urbaniec, Andrzej, Katarzyna Drabik, & Marek Dohnalik. 2018. "Selected Features of Carbonate Rocks Based on the X-Ray Computed Tomography Method (CT)." Nafta-Gaz 74(3): 181–92.

Vanderputten, E., Dehairs, F., Keppens, E. & Baeyens, W., 2000. "High-resolution distribution of trace elements in the calcite shell of modern Mytilus edulis: environmental and biological controls". Geochemica et Cosmochemica Acta 64, 997-1011.

Wang, L., & Liu, H., 2006. "An Efficient Method for Identifying and Filling Surface Depressions in Digital Elevation Models for Hydrologic Analysis and Modelling". International Journal of Geographical Information Science 20(2): 193–213.

Warlo, Ma., Bark, G., Wanhainen, Ch., Butcher, A., Forsberg, F., Lycksam, H., & Kuva, J., 2021. "Multi-Scale X-Ray Computed Tomography Analysis to Aid Automated Mineralogy in Ore Geology Research." Frontiers in Earth Science 9(December): 1–24.

Wilding, M., Lesher, C. E., Shields, K., 2005. "Applications of neutron Computed Tomography in the geosciences". Nuclear instruments and methods in physics research, section, A, 542 (1–3), 290–295. Doi: 10.1016/j.nima.2005.01.151